PHD

Investigation of Thin Responsive Polymer Films Using Evanescent Wave Optics with Dissipation

Menges, Bernhard

Award date:
2013

Awarding institution:
University of Bath

Investigation of thin responsive polymer films using evanescent wave optics with dissipation

Bernhard Ernst Menges

A thesis submitted for the degree of Doctor of Philosophy

University of Bath
Department of Chemistry
February 2013

Abstract

In recent years, new research emphasis has been directed towards integrating multiple functions into polymeric materials. Among these new advances in materials science functional polymers with structural designs are intended to produce a specific polymer function. One group of these polymeric materials are the so-called smart hydrogels. Such polymers undergo a discontinuous or continuous large volume change transition in response to a small environmental stimulus such as temperature, *pH*-value, ionic strength, etc. The swelling characteristics of these networks have been studied extensively with regards to their use in micro devices or drug delivery systems.

In order to utilize thin films of responsive hydrogels based on poly(N-isopropyl-acrylamide) (*pNIPAAm*) as active matrix in sensor applications, detailed knowledge about their structural and dynamical properties as well as their response to external stimuli is required. In the present study such dynamical and structural changes by swelling and collapsing were studied using Surface Plasmon Resonance / Optical Waveguide Spectroscopy (*SPR/OWS*) with dissipation. In combination with the reversed Wentzel-Kramers-Brillouin (*rWKB*) and Bruggeman effective medium approximation and by modelling the hydrogel film as a composite of sublayers with individual complex refractive indices, refractive index/volume fraction gradient profiles perpendicular to the surface are accessible simultaneously with information about local inhomogeneities. The imaginary refractive index κ of each sublayer can specifically be interpreted as a measure for static and dynamic inhomogeneities, which were found to be highest at the critical collapse temperature in the layer centre. These results indicate that the hydrogel collapse originates rather from the film centre than from its boundaries.

Furthermore, the influence of silica nanoparticles, solvent and film thickness to the swelling behaviour and transition temperature was investigated.

Moreover time-resolved quantitative studies of protein-functionalized hydrogel films are shown as well as the use of hydrogel supported protein-tethered bilayer lipid membranes as a new approach toward polymer-supported lipid membranes.

Table of Contents

List of Figures

List of Tables

Abbreviations

A	amplitude
AcSH	thioacetic acid
ACT	acetate
AFM	atomic force microscopy
AIBN	2,2'-Azobis-(isobutyronitrile)
APTES	3-Aminoprop-1-yl-triethoxysilane
ATR	attenuated total reflection
BPTES	4-benzoylphenoxypropyl-(triethoxy)silane
CcO	cytochrome c oxidase
DLS	dynamic light scattering
DMF	dimethylformamid
DMIAAm	N,N-dimethylacrylamide
DMSO	dimethylsulfoxide
DSC	differential scanning calorimetry
E	electrical field
EDC	1-Ethyl-3-(3-dimethylaminopropyl) carbodiimide
EIS	electrochemical impedance spectroscopy
EMT	effective-medium theory
EPR	electron paramagnetic resonance
f	volume fraction
FCS	fluorescence correlation spectroscopy
FWHM	full width at half maximum
H	magnetic field
HeNe	helium neon
HMDS	hexamethyldisilazane
IgG	immunoglobulin G
Ip	isoelectric point
ITO	indium-tin oxide
LCST	lower critical solution temperature
MAA	methacrylic acid
MABP	4-Methacryloylbenzophenone
MBAAm	methylenbisacrylamid
M_w	molecular weight
NA	neutravidin
n_{eff}	effective refractive index
NHS	N-Hydroxysuccinimid
NIPAAm	N-isopropylacrylamide
NMR	nuclear magnetic resonance

NP	nanoparticles
NTA	nitrilo-triacetic acid
OWS	Optical Waveguide Spectroscopy
PBS	Phosphate buffered saline
PED	photocrosslinking energy dose
PDI	Polydispersitytsindex
PMMA	poly(methyl methacrylate)
pNIPAAm	poly(N-isopropylacrylamide)
PS	polystyrene
ptBLM	protein-supported bilayer lipid membrane
rms	root mean square
rWKB	reversed Wentzel-Kramers-Brillouin
SCF	self-consistent field theory
SPR	surface plasmon resonance
SR	swelling ratio
T_C	volume transition temperature
TE	transversal-electric
TEOS	tetraethylorthosilicate
TFPS	para-tetrafluorophenol sulfonate
THF	tetrahydrofuran
TM	transversal magnetic
UV	ultra violet
WaMS	waveguide mode spectroscopy
α	polarizability
ß	propagation constant
Γ	surface mass density
ε	dielectric function
Θ	angle of incidence
κ	imaginary refractive index
Λ	periodicity
λ	wavelength
ϕ	phase
ω	angular frequency

Acknowledgements

First of all, I want to thank Prof. Wolfgang Knoll for giving me the opportunity to start my PhD in his group at the Max Planck Institute for Polymer Research in Mainz and supporting all my scientific ideas and Prof. Silvia Mittler for her inspiration to start my PhD project.

Second; I want to thank my supervisor Dr. Toby Jenkins from Bath University for the great support and his patience and understanding on this issue.

I would also like to thank Prof. Mischa Bonn for giving me the freedom to finishing my PhD project in his group Molecular Spectroscopy at the MPI-P in Mainz.

Great thanks go out to my collaborators in various cooperations for this thesis: Ulrich Jonas, Jakub Dostalek, Renate L.C. Naumann, Robert F. Roskamp, Matthias J. N. Junk, Ilke Anac, Coenraad van den Brom, Markus Retsch, Alena Aulasevich, Asmorom Kibrom, Piotr Jakubowicz, Catrin Corten and Christoph Hoffmann.

I want to thank Prof. Silvia Mittler, Prof. Uwe Langbein and Laurie Gangloff for proof reading of the thesis.

The infrastructure at the MPI-P is excellent. Thanks to the mechanical and the electrical workshop, the supermarket and the glassblower for the support. Especially I want to thank Natalie Horn and Charlie Mears, for keeping labs in shape.

Finally, the most constant support during all this time was my family. Thanks a lot to Isabel, Jonas and Jara.

1 Introduction

1.1 Hydrogels

In polymer chemistry, networking is a commonly used way to preserve polymers with improved material properties. It particularly applies to properties such as hardness, elasticity and stability. A special class of crosslinked polymers consists of chemically or physically networked polymer chains that make up a three-dimensional network, which has recorded large quantities of solvents. Such swollen networks are called "gels". If water is the solvent one speaks of a "hydrogel". The properties of gels are between those of a liquid and a solid material. They are like soft materials such as liquids, but they can retain their shape such as solid materials. Due to these properties, hydrogels have industrial potential as superabsorbent diapers or soft contact lenses [1].

Of special interest are "stimuli responsive" or "smart" polymers. These polymers react with great property changes to small physical or chemical stimuli, such as e.g. temperature, *pH* or pressure change. The microscopic changes are observable on a macroscopic level. The unlinked polymer reacted by precipitating from a solution or by renewed solving. Crosslinked polymers react with a decrease or increase in the volume by orders of magnitude. In both polymer types these changes are reversible.

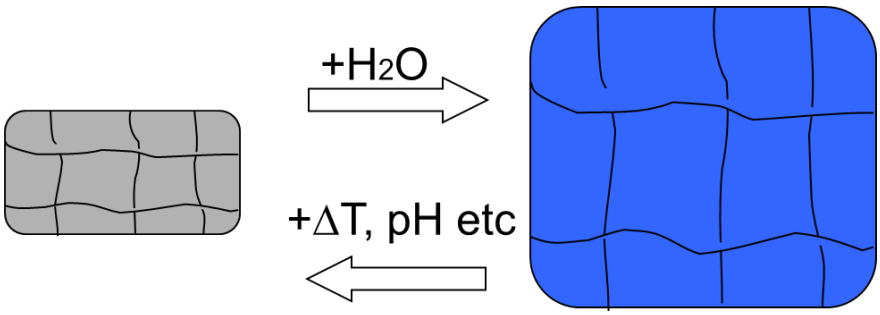

Fig. 1.1: Scheme of stimuli responsive hydrogel.

1.2 Responsive *pNiPAAm*-based Hydrogels

Much research was done on systems where the temperature, solvent composition and *pH*-value have been changed to find applications in various areas of the switchable polymer [2-4]. Poly(N-Isopropylacrylamid) (*pNIPAAm*), which shows a sharp phase transition at approximately 33 *°C* in water and is thus switchable by temperature change, is one of the best studied switchable polymer [5,6]. The reason for this sharp phase transition is a good balance between hydrophilic and hydrophobic interactions of the polymer [2]. The temperature rise above the lower critical solution temperature (*LCST*) in an aqueous *pNIPAAm* solution leads to a reduced efficiency of the hydrogen bonds between polymer and water, which no longer is enough to keep the *pNIPAAm* in solution. A phase separation occurs, which goes hand in hand with the transfer of water bound to the polymer chains and leads to the formation of two phases: a polymer-rich phase and an aqueous phase that contains almost certainly no polymer anymore. The process of water delivery is endothermic, and can be followed by differential scanning calorimetry (*DSC*) [7-9]. It has been demonstrated that hydrophobic interactions play an important role with regard to the phase transition of *pNIPAAm* gels in water [10,11]. The hydrophobicity of the N-alkyl group in the side chain particularly affected the transition temperature of thermally induced phase transition to a great extent. However, the degree of swelling is mainly affected by the elastic properties and the nature of the network backbone. The swelling properties of *pNIPAAm* hydrogels can effectively be modified through copolymerization with co-monomer carrying loaded groups [5,12-19]. However, the fact that the network density [13,20] and the surface connection [21,22] have a major impact on the swelling behavior cannot be neglected. A known issue in (co) polymers of *NIPAAm* without ionic groups is the skin barrier effect if they collapse [2,23]. This barrier arises because not the entire gel suddenly collapses, but initially only the outer parts close to the surface, which experienced the temperature change first. The water is driven out from these areas and it forms a dense outer layer. This skin layer prevents the water in the gel to diffuse out and slows or prevents the transition from the swollen to the collapsed state. To overcome this problem, either hydrogels with macro pores are established [5,23] or an integration of ionic groups. [5,12] These poly-electrolyte units serve as hydrophilic channel-like regions and allow the diffusion of water in the collapsing hydrogel.

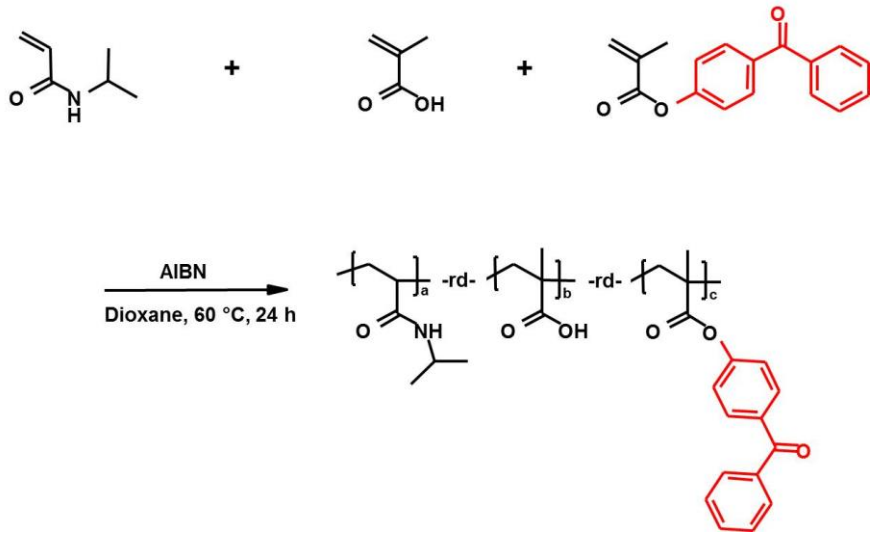

Fig. 1.2: General polymerization reaction for the statistical (stat) *pNIPAAm* terpolymer with methacrylic acid as the ionic species.

The most commonly method to make hydrogels is using free radical polymerization. [2,12,23,24] Where a bi-functional co-monomer (e.g. Methylenbisacrylamid (*MBAAm*)) is introduced into the polymerization, which ensures a network of polymer chains during the polymerization reaction.

The list of possible applications for hydrogels is long. The use as sensors and actuators [25-27], which take advantage of the volume phase transition of hydrogels, is possible in many areas, for example the fluidics [28,29]. Other possible areas are "tissue engineering" [30,31], "drug delivery" [32], "anti-fouling" coatings [33] and wound care [34,35]. The use of hydrogels as organic molecules was also examined [36,-42]. However, the problem of anchoring of biomolecules in the gel arises. In the regular occurrence of only non-specific interaction [43] the risk of displacement by competing reagents takes place [44]. Therefore coupling strategies have been pursued frequently [45-47], often based on weak reactive groups (e.g. easily oxidizable aldehyde groups). However, is promising the use of active ester group, based on N-Hydroxysuccinimid (*NHS*), which are very reactive compared to amines and still have some stability [48].

1.3 Evanescent wave optics: State of the art data analysis

Surface Plasmon Resonance (*SPR)* is a powerful tool to study the optical properties of polymers as thin films and yields information about thickness and refractive index [49]. Yet, an independent determination of both variables only by *SPR* is not possible. However, when polymer films are sufficiently thick (> 500 *nm*), optical waveguide modes can be observed in addition to the surface plasmon resonance. This combination of *SPR* with optical waveguide mode spectroscopy (*OWS*) allows independent characterization of the thickness and refractive index at a single measuring wavelength [49,50].

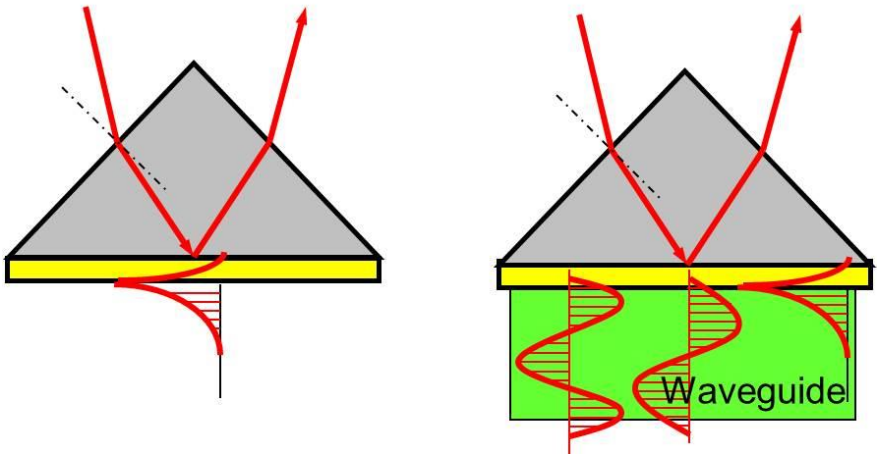

Fig. 1.3: Schematic setup of Kretschmann configuration for surface plasmon resonance and optical waveguide excitation.

A common method for the analysis of *SPR/OWS* data assumes a homogeneous refractive index for the whole polymeric layer. As recently shown for several systems, this so-called box model is not always appropriate since it exhibits a pronounced refractive index gradient perpendicular to the surface [5,51,52]. The primary cause for the anisotropy in the surface-grafted films is to be found in the covalent surface attachment via the benzophenone anchor layer, which restricts lateral expansion and leads to quasi-1D swelling away from the substrate-hydrogel interface. This optical gradient profile is accessible by a combination of *SPR/OWS* with the reversed Wentzel-Kramers-Brillouin (*rWKB*) approximation [5,52].

Polymer volume fraction profiles of thin hydrogel films were previously studied by several methods. Habicht et al. and Toomey et al. investigated polymer brushes and crosslinked polymer films based on styrene and dimethylacrylamide by multiple-angle nulling ellipsometry and modeled the gradient profiles for various crosslinking densities using an effective medium

approximation [53,54]. Vidyasagar et al. [51], Seitz et al., and Yim and al. [55] used neutron scattering to reveal temperature-dependent changes of the volume fraction profiles of surface-attached *pNiPAAm* networks, Mendez et al. chose a computational approach based on self-consistent field (*SCF*) theory [56].

1.4 Aim und Outline

The aim of the thesis is the investigation of thin thermo-responsive N-isopropyl-acrylamide (*NiPAAm*) based hydrogel films using evanescent wave optics with dissipation to study the swelling behaviour more in detail. For sensor applications the responsive hydrogel matrix is often immobilized as thin film on a solid substrate, which can lead to very different dynamic properties compared to the bulk gels [57].

For these studies, it is necessary to develop new data analysis methods. The noble combination of surface plasmon resonance and optical waveguide spectroscopy (*SPR/OWS*) in Kretschmann configuration with the reversed Wentzel-Kramers-Brillouin (*rWKB*) approximation is a powerful technique to gain detailed information about refractive index profiles, gradients and inhomogeneities in thin surface-attached responsive hydrogel films. The refractive index profile perpendicular to the film surface is calculated by the reversed *WKB* approximation from the *SPR/OWS* spectra. Such a refractive index profile forms the basis of a multilayer model, in which for each individual slab perpendicular to the multilayer surface the local refractive index n and the corresponding imaginary part κ is calculated using transfer matrix algorithm. This imaginary part κ is a measure for optical losses, which are interpreted in our system as hydrogel inhomogeneities. The procedure developed to obtain this data is presented and discussed in chapter 2.

An investigation on the optical properties of the hydrogel and analysis of the optical gradient profiles was conducted based on evanescent wave optics in chapter 4.

To achieve structural reinforcement, nanoparticles functionalized with benzophenone moieties were introduced as multiple photo-crosslinking units. Hydrogel nanocomposites exploit the embedding of nanoparticles (*NPs*) into a hydrogel polymer matrix to modify its properties. Such nanocomposites haven been extinsively studied, predominantly for the

purpose of structural reinforcement [58] and investigated in chapter 5.

Swelling of these immobilized 2D hydrogel layers is highly anisotropic due to the restricted in-plane (lateral) swelling, so that a volume change is only possible perpendicular to the substrate [59-61]. This decreases the maximum degree of swelling and may prevent the gel film from fully collapsing particularly close to the substrate (approx. < 500 *nm*). Also the transition temperature of the surface attached *pNIPAAm* gel films is affected by the lateral constraint. Besides these intrinsic anisotropy effects, the swelling behaviour of the hydrogel film matrix is affected by environmental changes and analyte binding. In order to fully understand the sensor response, it is necessary to deconvolute the effect of specific analyte binding and the influence of unspecific environmental parameters. In particular *pNIPAAm* gels show an unusual swelling behaviour in mixed solvents, and this compositional effect of the liquid medium in contact with the active matrix is of substantial technological relevance for sensor design and implementation and was investigated in chapter 6. In chapter 7 ultra-thin *pNIPAAm* films, less than 100 *nm* thickness was studied.

In chapter 8 the implementation of *OWS* for quantitative time-resolved characterization of mass changes and the swelling behaviour of protein-functionalized N-isopropylacrylamide (*NIPAAm*)-based hydrogel films is reported. This thermal responsive gel can be used for the design of advanced biosensor binding matrices.

The concept of poly(N-Isopropylacrylamid) (*pNIPAAm*) supported protein-tethered bilayer lipid membranes (*ptBLM*) was proved in chapter 9.

Chapter 4 “Analysis of optical gradient profiles” was published in

Matthias J. N. Junk, Ilke Anac, Bernhard Menges and Ulrich Jonas, Analysis of Optical Gradient Profiles During Temperature and Salt Dependent Swelling of Thin Responsive Hydrogel Films, *LANGMUIR*, Volume: 26 Issue: 14 Pages: 12253-12259, 2010

Chapter 5 “Nanoparticle composites” was published in

Coenraad van den Brom, Ilke Anaç, Robert F Roskamp, Markus Retsch, Ulrich Jonas, Bernhard Menges, Jon A Preece, The Swelling Behaviour of Thermoresponsive Hydrogel-Silica Nanoparticle Composites,

J. MATER. CHEM. 20 (23), 4827-4839, 2010

Chapter 6 “Cononsolvency Effects” was published in

Ilke Anac, Alena Aulasevich, Matthias J. N. Junk, Piotr Jakubowicz, Robert F. Roskamp, Bernhard Menges, Ulrich Jonas, Wolfgang Knoll, Temperature Dependent Swelling Behavior of Thin Poly(N-isopropylacrylamide) Copolymer Gel Layers in Ethanol-Water Mixtures *MAROMOLECULAR CHEMISTRY AND PHYSICS*, 211 (9), 1018-1025, 2010

The application as “Protein-Functionalized Hydrogel Films” in chapter 8 was published in

A. Aulasevich, R.F. Roskamp, U. Jonas, B. Menges, J. Dostalek and W. Knoll, Optical Waveguide Spectroscopy for the Investigation of Protein-Functionalized Hydrogel Films, *MACROMOLECULAR RAPID COMMUNICATIONS* 30 (9-10), 872-877, 2009

Chapter 9 “Hydrogel-Supported Membranes” was published in

Asmorom Kibrom, Robert F. Roskamp, Ulrich Jonas, Bernhard Menges, Wolfgang Knoll, Renate L.C. Naumann, Hydrogel-Supported Protein-Tethered Bilayer Lipid Membranes: a New Approach toward Polymer-Supported Lipid Membranes,

SOFT MATTER, Vol. 7 Issue: 1, 237-246, 2011.

References

[1] Stoy, V.; Wichterle, A.; Stoy, A. *US-Patent*, US4095877, **1978**
[2] Schild, H.G. *Prog. Polym. Sci.* **1992**, *17*, 163
[3] Hoffmann, A.S. et al. *J. Biomed. Mater. Res.* **2000**, *52*, 577
[4] Kokufuta, E. *Adv. Polym. Sci.* **1993**, *110*, 157
[5] Beines, P.W.; Klosterkamp, I.; Menges, B.; Jonas, U.; Knoll, W. *Langmuir* **2007**, *23*, 2231
[6] Heskins, H.; Guillet, J.E. *J. Macromol. Sci., Chem.* **1968**, *A2*, 1441
[7] Shibayama, M.; Suetoh, Y.; Nomura, S. *Macromolecules* **1996**, *29*, 6966
[8] Schild, H.G.; Tirell, D.A. *J. Phys. Chem.* **1990**, *94*, 4352
[9] Yamazaki, Y.; Tada, T.; Kunugi, S. *Colloid Polym. Sci.* **2000**, *278*, 80
[10] Ilmain, F.; Tanaka, T.; Kokofuta, E. *Nature* **1991**, *349*, 400
[11] Otake, K.; Inomata, H.; Konno, M.; Saito, S. *Macromolecules* **1990**, *23*, 283
[12] Yu, H.; Grainger, D.W. *J. Appl. Polym. Sci.* **1993**, *49*, 1553
[13] Kuckling, D.; Harmon, M.E.; Frank, C.W. *Macromolecules* **2002**, *35*, 6377
[14] Hirotsu, S.; Hirokawa, Y.; Tanaka, T. *J. Chem. Phys.* **1987**, *87*, 1392
[15] Feil, H.; Bae, Y.H.; Feijen, J.; Kim, S.W. *Macromolecules* **1992**, *25*, 5528
[16] Huglin, M.B.; Liu, Y.; Velada, J.L. *Polymer* **1997**, *38*, 5785
[17] Erbil, C.; Aras, S.; Uyanik, N. *J. Poly, Sci. A* **1999**, *37*, 1847
[18] Wu, W.F.; Hsu, C.H. *Polymer* **1998**, *39*, 5393
[19] Hirose, H.; Shibayama, M. *Macromolecules* **1998**, *31*, 5336
[20] Harmon, M.E.; Kuckling, D.; Frank, C.W. *Macromolecules* **2003**, *36*, 162
[21] Prucker, O.; Naumann, C.A.; Rühe, J.; Knoll, W.; Frank, C.W. *J. Am. Chem. Soc.* **1999**, *121*, 8766
[22] Toomey, R.; Freidank, D.; Rühe, J. *Macromolecules* **2004**, *37*, 882
[23] Xue, W.; Hamley, I.W.; Huglin, M.B. *Polymer* **2002**, *43*, 5181
[24] Tanaka, T. *Encyclopedia of Polymer Science and Engineering*, Vol. 7, John Wiley & Sons
[25] Qiu, Y.; Park, K. *Adv. Drug Delivery Rev.* **2001**, *53*, 321
[26] Hoffmann, A.S. *Adv. Drug Delivery Rev.* **2002**, *54*, 3
[27] Peppas, N.A.; Hilt, J.Z.; Khademhosseini, A.; Langer, R. *Adv. Mater.* **2006**, *18*, 1345
[28] Richter, A.; Kuckling, D.; Howitz, S.; Gehring, T.; Arndt, K.F. *J. Microelectromech. Syst.* **2003**, *12*, 748
[29] Kishi, R.; Ono, E.; Ichijo, H.; Hirasa, O., Plenum Press
[30] Ohya, S.; Nakayama, Y.; Marsuda, T. *Biomacromolecules* **2001**, *2*, 856
[31] Richardson, T.P.; Peters, M.C.; Ennett, A.B.; Mooney, D.J. *Nature Biotechnology* **2001**, *19*, 1029
[32] Maryland, P.; Zhang, Y.; Amidon, G.L.; Yang, V.C. *J. Biomed. Mater. Res.* **1999**, *47*, 595
[33] Sassi, A.P.; Lee, S.H.; Park, Y.H.; Blanch, H.W.; Praunitz, J.M. *J. Appl. Polym. Sci.* **1996**, *60*, 225
[34] Corkhill, P.H.; Hamilton, C.J.; Tighe, B.J. *Biomaterials* **1989**, *10*, 3
[35] Corkhill, P.H.; Hamilton, C.J.; Tighe, B.J. *Crit. Rev. Biocompat.* **1990**, *5*, 363
[36] Page, J.D.; Derango, R.; Huang, A.E. *Colloids and Surfaces A* **1998**, *132*, 193
[37] Wolpert, S. *Journal of Membrane Science* **1997**, *132*, 23
[38] Disley, D.M.; Blyth, J.; Cullen, D.C.; You, H.X.; Eapen, S.; Lowe, C.R. *Biosensors &*

Bioelectronics **1998**, *13*, 383
[39] Choi, K.; Ha. Y.; Youn, H.; Choi, J. *Journal of Biochemistry and Molecular Biology* **1997**, *30*, 308
[40] Singh, P. *Bioconjugate Chemistry* **1998**, *9*, 54
[41] Sanford, M.S.; Charles, P.T.; Commisso, S.M.; Roberts, J.C.; Conrad, D.W. *Chemistry of Materials* **1998**, *10*, 1510
[42] Piskin, E. Int. *J. Artif. Organs* **1984**, *7*, 283
[43] Buijs, J.; White, D.D.; Norde, W. *Colloids and Surfaces B* **1997**, *8*, 239
[44] Brynda, E.; Houska, M.; Skvor, J.; Ramsden, J.J. *Biosensors & Bioelectronics* **1998**, *13*, 165
[45] MacBeath, G.; Schreiber, S.L. *Science* **2000**, *289*, 1760
[46] Joos, T.O. et al. *Electrophoresis* **2000**, *21*, 2641
[47] Mendoza, L.G.; McQuary, P.; Mongan, A.; Gangadharan, R.; Brignac, S.; Eggers, M. *Biotechniques* **1999**, *27*, 778
[48] Ferruti, P.; Bettelli, A.; Fere, A. *Polymer* **1972**, *13*, 462
[49] Knoll, W., Annu. Rev. Phys. Chem., 1998. **49**: p. 569-638.
[50] Harmon, M.E., Kuckling, D., and Frank, C.W., Macromolecules, 2003, 36(1): p. 162-172.
[51] Vidyasagar, A., Majewski, J., and Toomey, R., Macromolecules, 2008, 41(3): p. 919-924.
[52] Weisser, M., et al., Opt. Commun., 1998, 153(1-3): p. 27-31.
[53] Toomey, R., Freidank, D., and Rühe, J., Macromolecules, 2004, 37(3): p. 882-887.
[54] Mendez, S., et al., Macromolecules, 2005, 38(1): p. 174-181.
[55] Yim, H., et al., Macromolecules, 2004, 37(5): p. 1994-1997
[56] Xue, W., Hamley, I.W., and Huglin, M.B., Polymer, 2002, 43(19): p. 5181-5186.
[57] M. Schonhoff, A. Larsson, P. B. Welzel, D. Kuckling, J. Phys. Chem. B 2002, 106, 7800.
[58] G. M. Eichenbaum, P. F. Kiser, S. A. Simon, D. Needham, Macromolecules 1998, 31, 084.
[59] A. Revzin, R. J. Russell, V. K. Yadavalli, W. G. Koh, C. Deister, D. D. Hile, M. B. Mellott, M. V. Pishko, Langmuir 2001, 17, 5440.
[60] I. Tokarev, S. Minko, Soft Matter 2009, 5, 511.
[61] J. Kim, I. Deike, N. Dingenouts, C. Norhausen, M. Ballauff, Macromol. Symp. 1999, 142, 217.

2 Evanescent Wave Optics Methods

The term evanescent wave optics summarizes a number of optical phenomena and techniques associated with the total internal reflection of light at the boundary between two media of different optical properties [1].

A stack of films with different optical properties and eventually different physico-chemical properties formed the basic configuration of the samples applied in this experimental thesis.

The transfer-matrix formalism is the central method for the theoretical description of reflection and transmission properties of multilayer systems. This formalism includes different resonance phenomena, such as the surface plasmon resonance and metal film enhanced leaky waveguide modes in Kretschmann configuration. A novel combination of the reversed Wentzel-Kramers-Brillouin (*rWKB*) approximation with the surface plasmon resonance allowed an accurate determination of refractive index profiles along the stack of films (perpendicular to the surface). Such a refractive index profile formed the basis of a multilayer model, in which for each individual slab parallel to the multilayer surface the local refractive index n and the corresponding imaginary part κ was calculated. The imaginary part κ determined the optical losses, which were interpreted in our system as hydrogel inhomogeneities. Utilizing an effective medium approximation, the refractive index profile of the gels could be converted into polymer volume fraction profiles.

2.1 Transfer Matrix Algorithm of a 2-Layer System

The transfer matrix formalism is the central method for the theoretical description of reflection and transmission properties of multilayer systems. Different resonance phenomena such as guided and quasi guided optical waves or the surface plasmon resonance are described on this basis.

Starting point of consideration is the transition of a plane light wave from medium (i) into a medium (j). This transition is described by the Fresnel equations, which link the reflected or transmitted field amplitudes to the amplitudes of the incident field.

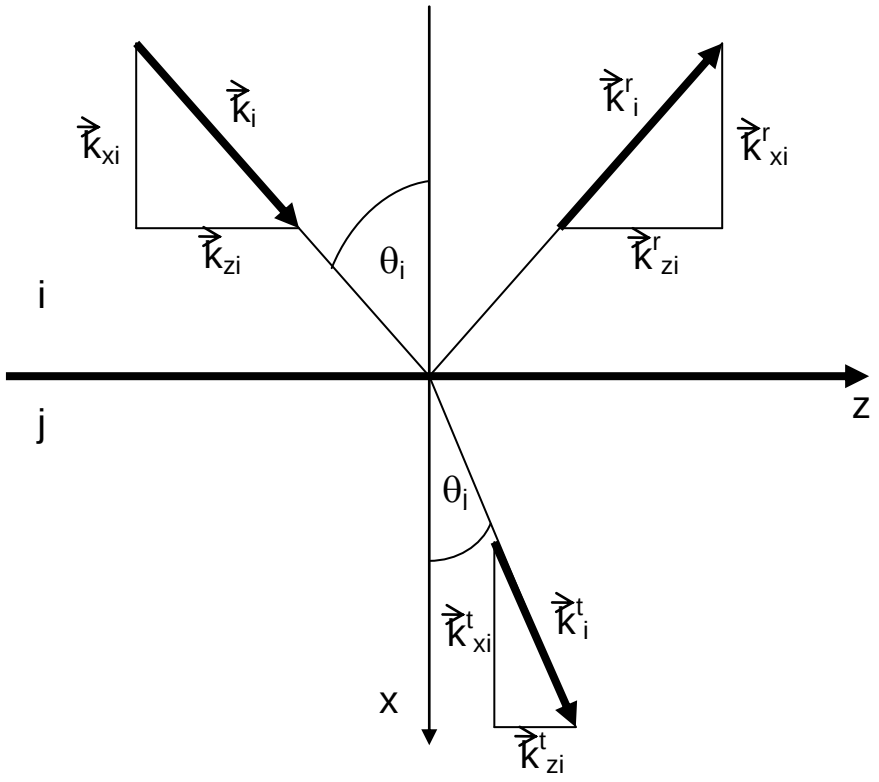

Fig. 2.1: Reflection and transmission at an interface

A plane monochromatic wave is defined as:

$$\vec{E}_{(\vec{r},t)} = \vec{A} \cdot e^{-j(\vec{k}\cdot\vec{r}-\omega t)} \qquad (2.1)$$

with the electrical field vector *E*, the position vector *r*, the time *t*, the amplitude *A*, the wave vector *k*, and ω the angular frequency. In case when the x-z-plane is the plane of incidence (Fi.g.2.1), the physical properties are independent from the y-coordinate. Therefore, the field components can be decoupled:

$$\vec{E}^{TE} = \begin{pmatrix} 0 \\ E_y \\ 0 \end{pmatrix}; \vec{H}^{TE} = \begin{pmatrix} H_x \\ 0 \\ H_z \end{pmatrix} \qquad \text{TE-polarization (s)} \qquad (2.2)$$

$$\vec{E}^{TM} = \begin{pmatrix} E_x \\ 0 \\ E_z \end{pmatrix}; \vec{H}^{TM} = \begin{pmatrix} 0 \\ H_y \\ 0 \end{pmatrix} \qquad \text{TM-polarization (p)} \qquad (2.3)$$

One differentiates between transversal-electric (*TE* or *s*) polarization and transversal magnetic (*TM* or *p*) polarization. If the *E* field vector is oriented perpendicular to the plane of incidence, it is called *TE* polarization. Similarly, *TM* polarization occurs if the *E*-field vector is aligned parallel to the plane of incidence.

If we consider an incident wave in medium (i) at an incidence angle θ_i, as shown in Figure 2.1, the normal component of the wave vector *k* is:

$$k_{xi} = \sqrt{k_0^2 \tilde{n}_i^2 - k_{zi}^2} = \sqrt{k_0^2 \tilde{n}_i^2 - k_0^2 n_{eff}^2} \qquad (2.4)$$

with $k_0 = 2\pi/\lambda$ the vacuum wave vector, λ the, and $\tilde{n}_i = n_i + j\kappa_i$ the complex refractive index of the medium. For transparent dielectrics $\kappa_i \approx 0$ in good approximation and the index of refraction is equivalent to the real refractive index: $\tilde{n}_i = n_i$.

The tangential component k_{zi} or the effective refractive index defined by $n_{eff} = k_{zi}/k_0$ is constant during the transition from medium (i) to medium (j), which is equivalent to Snell's law:

$$k_{zi} = n_i k_0 \sin\theta_i = n_j k_0 \sin\theta_j \Leftrightarrow n_i \sin\theta_i = n_j \sin\theta_j = n_{eff} \qquad (2.5)$$

Reflection, *r*, and transmission, *t*, coefficients are polarization dependent. The Fresnel equations describe the reflection and transmission at an interface for the respective polarization.

$$r_{ij}^{TE} = \frac{k_{xi} - k_{xj}}{k_{xi} + k_{xj}} \tag{2.6}$$

$$t_{ij}^{TE} = \frac{2k_{xi}}{k_{xi} + k_{xj}} \tag{2.7}$$

$$r_{ij}^{TM} = \frac{n_j^2 k_{xi} - n_i^2 k_{xj}}{n_j^2 k_{xi} + n_i^2 k_{xj}} \tag{2.8}$$

$$t_{ij}^{TM} = \frac{2n_i n_j k_{xi}}{n_j^2 k_{xi} + n_i^2 k_{xj}} \tag{2.9}$$

To fulfill the stationary Helmholtz equation for a layer system as shown in Figure 2.2, a linear combination of the electrical field in the positive and negative *x* direction is used for *TE* polarized light:

$$E_{i(x)} = A^{+} e^{-jk_{xi}x} + A^{-} e^{jk_{xi}x} \tag{2.10}$$

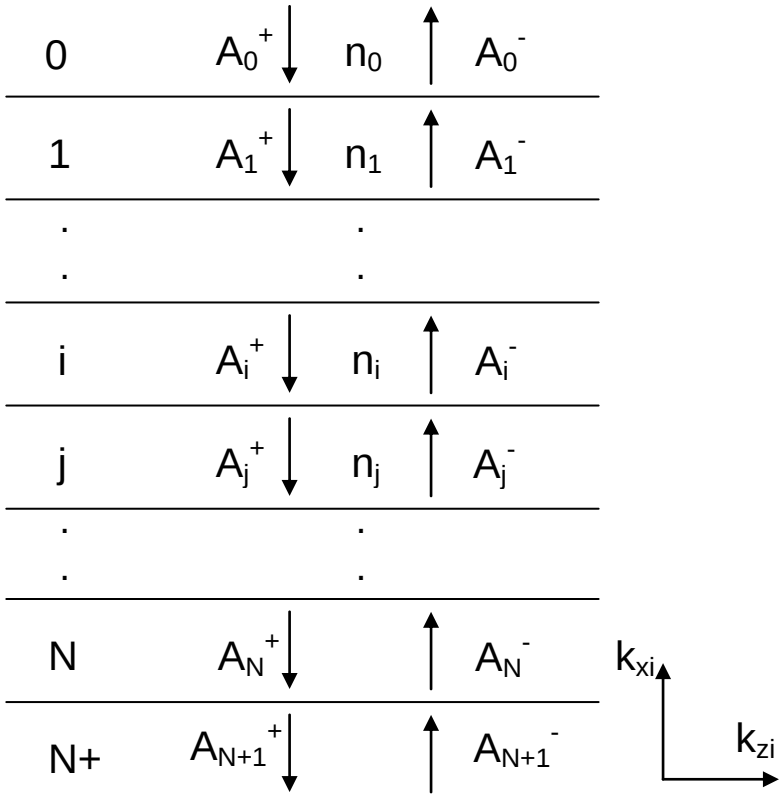

Fig. 2.2: N+2 layer system

The transfer matrix formalism links the amplitudes of electric fields in layer A_N^+ and A_N^- with the amplitudes of adjacent layer A_{N+1}^+ and A_{N+1}^- with the index + in positive direction and the index – in negative direction.

Eventually, the amplitude vector of the first layer is linked with the last layer by the transfer matrix M.

$$\begin{pmatrix} A_0^+ \\ A_0^- \end{pmatrix} = M \begin{pmatrix} A_{N+1}^+ \\ A_{N+1}^- \end{pmatrix} = \begin{bmatrix} M_{11} & M_{12} \\ M_{21} & M_{22} \end{bmatrix} \begin{pmatrix} A_{N+1}^+ \\ A_{N+1}^- \end{pmatrix} \tag{2.11}$$

M is the transfer matrix of the entire layer system. It is composed by the product of the respective transition and propagation matrices M_{ij}.

$$M = \begin{bmatrix} M_{11} & M_{12} \\ M_{21} & M_{22} \end{bmatrix} = D_{01} \prod_{i=1}^{N} P_i D_{i,i+1} \tag{2.12}$$

$$\begin{pmatrix} A_i^+ \\ A_i^- \end{pmatrix} = \frac{1}{t_{ij}} \begin{bmatrix} 1 & r_{ij} \\ r_{ij} & 1 \end{bmatrix} \begin{pmatrix} A_j^{\prime +} \\ A_j^{\prime -} \end{pmatrix} = D_{ij} \begin{pmatrix} A_j^{\prime +} \\ A_j^{\prime -} \end{pmatrix} \tag{2.13}$$

$$\begin{pmatrix} A_i^{\prime +} \\ A_i^{\prime -} \end{pmatrix} = \begin{bmatrix} e^{-j\phi_i} & 0 \\ 0 & e^{j\phi_i} \end{bmatrix} \begin{pmatrix} A_i^+ \\ A_i^- \end{pmatrix} = P_i \begin{pmatrix} A_i^+ \\ A_i^- \end{pmatrix} \tag{2.14}$$

where D_{ij} is the transition matrix between the layers i and j, P_i is the propagation matrix, which takes the phase difference in the layer into account. The characteristic 2 × 2 matrix M can be used to calculate both reflection and transmission coefficients of any homogeneous layer system.

To calculate the reflection and transmission coefficients of a layer system according to Figure 2.2 assume a wave coming from the top half-space with the amplitude of A_0 only and no incoming wave from the bottom half-space (i.e. $A_{N+1} = 0$). The resulting reflection coefficient is:

$$r(0 \to N+1) = \frac{M_{21}}{M_{11}} \tag{2.15}$$

And the transmission coefficient:

$$t(0 \to N+1) = \frac{1}{M_{11}} \tag{2.16}$$

In particular, the angular reflection behaviour, in the following called reflection spectrum, of the multilayer system is relevant in this thesis. Furthermore the transfer matrix method is useful for the calculation and simulation of reflected fields on multilayer systems. Surface plasmon or leaky waveguide modes appear as resonances in these reflection spectra. They will be usually recorded in a reflectivity spectrum. The reflectivity R of the entire layer system is given by:

$$R = |r|^2 = \left|\frac{M_{21}}{M_{11}}\right|^2 \tag{2.17}$$

2.3 Guided Waves in Layer Systems

In any optical layer system guided waves are present if the field components to the layer disappear and the outgoing fields decay exponentially, i.e. evanescently [2,3]. If apply the amplitudes A^+_0 and A^-_{N+1} equal to zero in equation (2.11), then:

$$0 = M_{11} A^+_{N+1} \tag{2.18}$$

$$A^-_0 = M_{21} A^+_{N+1} \tag{2.19}$$

one finds as a conclusion, guided waves are only possible when the matrix element M_{11} disappears:

$$M_{11} = 0 \tag{2.20}$$

For a multilayer system, M_{11} is just a function of the effective refractive index n_{eff}. Eq. 2.20 determines the propagation constant ß of guided modes. β can be calculated this way. Equation (2.20) represents an eigenvalue equation and β the eigenvalues.

$$\beta = k_z = k_0 n_{eff} \tag{2.21}$$

The field distribution of the resulting waveguide modes are as follows [4]:

$$\vec{E}_{(x,t)} = \vec{E}_m(x) e^{j(wt - ßz)} \tag{2.22}$$

$$\vec{H}_{(x,t)} = \vec{H}_m(x) e^{j(wt - ßz)} \tag{2.23}$$

$E_m(x)$ and $H_m(x)$ are the field distributions of the guided modes and m is the mode number.

The easiest waveguide structure forms a 3-layer system consisting of one dielectric layer and two dielectric half spaces, where the refractive index *n* of the dielectric layer is larger than that of the surrounding media. The geometry of such a planar waveguide is shown in Figure 2.3.

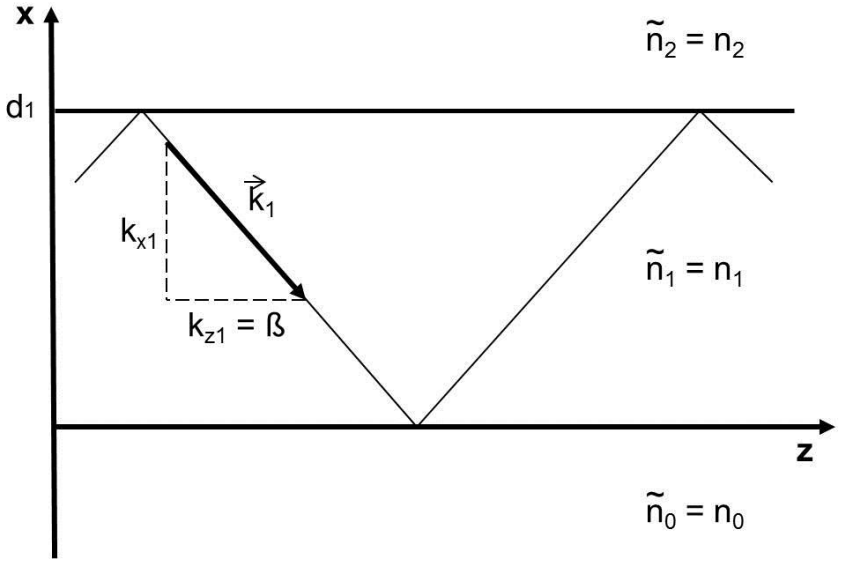

Fig. 2.3: Three layer waveguide configuration

Equation (2.20) can generally be understood as a condition for waveguiding in any layer system. In the case of planar film waveguides with step-index architecture, it is equivalent to the well-known transversals resonance condition; an eigenvalue equation obtained by solving the wave equation directly and taking into account the conditions of continuity at the interface [5].

Upon calculating the matrix of this 3-layer system according to equation (2.12), we obtain M_{11} for the matrix element:

$$M_{11} = \left(D_{01} P_1 D_{12}\right)_{11} = \frac{1}{t_{01} t_{12}} \left(e^{-j\phi_1} + r_{01} r_{12} e^{j\phi_1}\right) \tag{2.24}$$

The Fresnel coefficients and the phase ϕ depend on the polarization of the light.

For *TE* polarization:

$$m\pi = d_1 k_0 \sqrt{n_1^2 - n_{eff}^2} - \arctan\left(\frac{\sqrt{n_{eff}^2 - n_0^2}}{\sqrt{n_1^2 - n_{eff}^2}}\right) - \arctan\left(\frac{\sqrt{n_{eff}^2 - n_2^2}}{\sqrt{n_1^2 - n_{eff}^2}}\right) \tag{2.25}$$

And for *TM* polarization:

$$m\pi = d_1 k_0 \sqrt{n_1^2 - n_{eff}^2} - \arctan\left(\frac{n_1^2}{n_0^2}\frac{\sqrt{n_{eff}^2 - n_0^2}}{\sqrt{n_1^2 - n_{eff}^2}}\right) - \arctan\left(\frac{n_1^2}{n_2^2}\frac{\sqrt{n_{eff}^2 - n_2^2}}{\sqrt{n_1^2 - n_{eff}^2}}\right) \tag{2.26}$$

This resonance condition represents an eigenvalue equation and is only numerically solved. The individual eigenvalues n_{eff} are polarization dependent according to TE_m modes (s-polarized) and TM_m modes (p-polarized) with m = 0,1,2,… the mode number.

2.4 Surface Plasmon Polaritons

The surface plasmon or surface plasmon resonance is a surface wave that propagates along a single noble metal dielectric interface with an evanescent decay in two directions normal to the interface. The resonance condition or dispersions relation of the surface plasmon resonance can be calculated from the 3-layer system, considering a disappearing thickness (d_1 = 0) and a metallic half-space. With M_{11} and d_1 = 0 follows:

$$1 + r_{01} r_{12} = 0 \tag{2.27}$$

Insertion of Fresnel coefficients for *TE* polarization leads to:

$$k_{x0} + k_{x2} = 0 \tag{2.28}$$

Upon equation 2.4 and $k_{z0} = k_{z2} = ß$ one finds $\tilde{n}_0^2 = \tilde{n}_2^2$ however, this is impossible. Therefore, there is no solution for a *TE* surface wave.

Subsequently *TM* polarization is calculated:

$$\frac{k_{x0}}{\tilde{n}_0^2} + \frac{k_{x2}}{\tilde{n}_2^2} = 0 \tag{2.29}$$

Insert k_{x0} and k_{x2} according to equation (2.4) and the dispersion relation for the surface plasmon resonance is given [26]:

$$\tilde{\beta} = k_z = k_0 \sqrt{\frac{\tilde{n}_0^2 \tilde{n}_2^2}{\tilde{n}_0^2 + \tilde{n}_2^2}} \tag{2.30}$$

Because of the complex refractive index $\tilde{n}_2 = n_2 + j\kappa_2$ of the metal, the propagation constant β is becoming complex, i.e. an attenuated propagation of the surface wave. In this case the imaginary part of ß is responsible for the decay behaviour of the surface wave along the direction of propagation.

Fig.2.4 illustrates the quasi-free electron gas of the noble metal interface is excited to a collective oscillation. This can only be achieved if there is a field component perpendicular to the interface. The exponential decay is given by $e^{-jk_x x}$ to the interface. The penetration depth of the surface plasmon is defined by the decay of the evanescent field from the noble metal/ dielectricum interface. The depths were the field has decayed to *1/e* is the penetration depth.

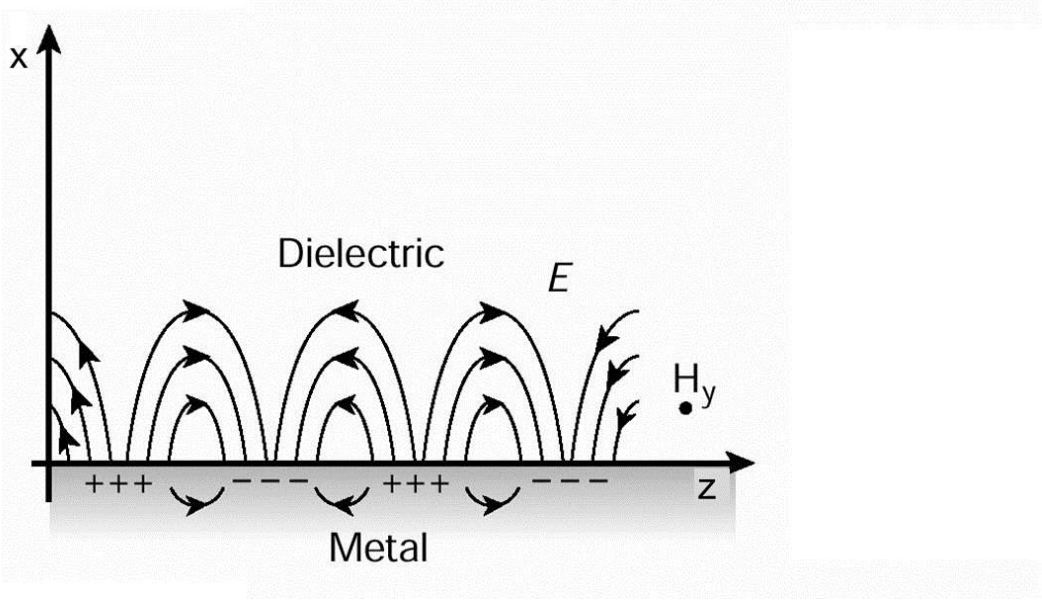

Fig. 2.4: Surface plasmon resonance on a noble metal/dielectricum interface

For gold ($\tilde{n}_{Au}$= 0.18 + *j*3.45) and silver ($\tilde{n}_{Ag}$= 0.08 + *j*4.12) this is fulfilled for λ = 633 nm. With the real refractive index of the dielectric follows:

$$\mathrm{Re}\{ß\} \approx k_0 \sqrt{\frac{n_0^2\left(n_2^2-\kappa_2^2\right)}{n_0^2+\left(n_2^2-\kappa_2^2\right)}} \rangle k_0 n_0 \qquad (2.31)$$

Surface plasmon resonance is a well-accepted analytical tool. [1, 6-8] Here, the surface plasmon polariton represents an extension of the so-called evanescent wave spectroscopy. In integrated optics the surface plasmon resonance (*SPR*) is very useful for the optical characterization of thin films using the method of attenuated total reflection (*ATR*). [9-11] In this thesis the sensitivity of the surface plasmon to refractive index changes in the evanescent field is used.

Because of $Re\{\beta\} > k_0 n_0$, a direct optical excitation of surface plasmon resonance is not possible. Therefore, the aforementioned attenuated total reflection (*ATR*) mechanism is needed. There are two major configurations possible: the Otto – and the Kretschmann configuration [12]. In both configurations the incoming light is totally internally reflected at the base of high refractive index prism. The created evanescent field can couple with the surface plasmon if the tangential component of the *k*-vector matches with the real part of the propagation constant of the surface plasmon. In Otto configuration a metal layer is placed close at the base of the prism. The distance must be in the order of the wavelength of light, so that the evanescent field is still strong enough to excite the surface plasmon. This is hard to achieve, therefore the Otto configuration is not used very often.

2.4.1 Kretschmann Configuration

The Kretschmann configuration is more commonly used and applied in this thesis. Here the surface plasmon is excited on the bottom of a metal film of a defined thickness [13,14]. The basic arrangement of the Kretschmann configuration is shown in Figure 2.5.

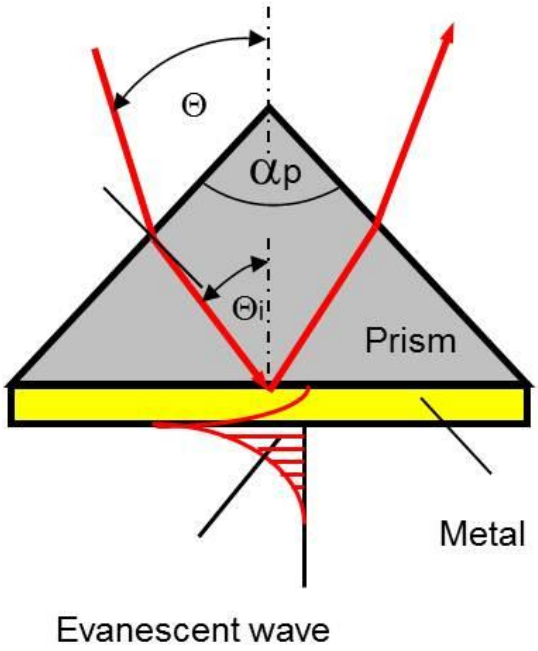

Fig. 2.5: Kretschmann configuration with high refractive index prism and a thin noble metal layer at the base.

The Kretschmann configuration represents one possibility of increasing the wave vector k_z of the incident light. Figure 2.6 shows the light line (dispersion relation of light) in the case of a propagation through air and through a prism with a dielectric constant larger than 1. At a given frequency ω the momentum in z-direction of the light propagating through the prism is increased. The light line has a smaller slope and therefore can match k_z of the surface plasmon. However, the momentum of the incident light has to be tuned to the surface plasmon by varying the angle of incidence.

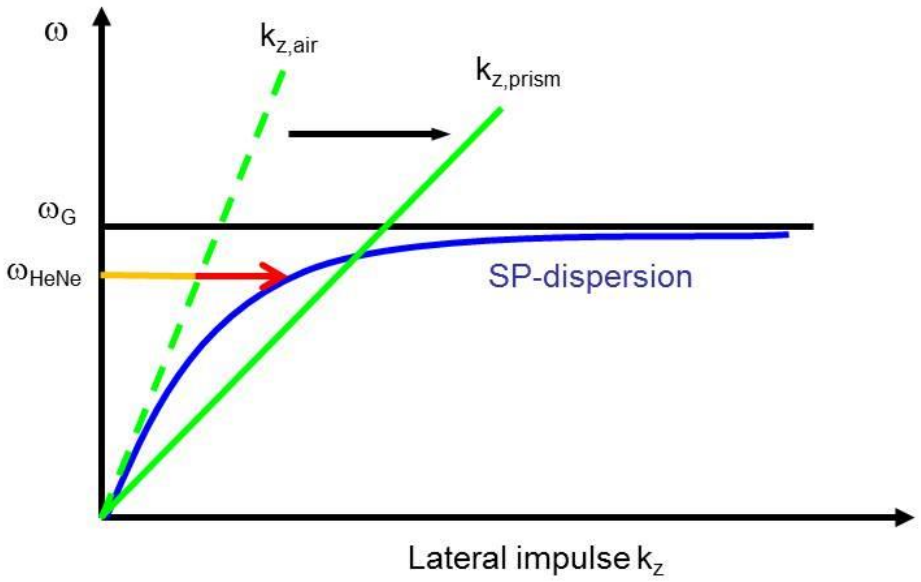

Fig. 2.6: Dispersion relation of free photons in air and in a dielectric such as the coupling prism compared to the dispersion of surface plasmon.

Experimentally, the resonant coupling is observed by monitoring the reflected light as a function of the angle of incidence. At the angle of coupling, a dip in the reflectivity versus angle spectrum is recorded. At the resonance, the total internal reflection is weakened; the energy of the incident light is coupled to the surface plasmon and dissipates along the plasmon propagation in the metal.

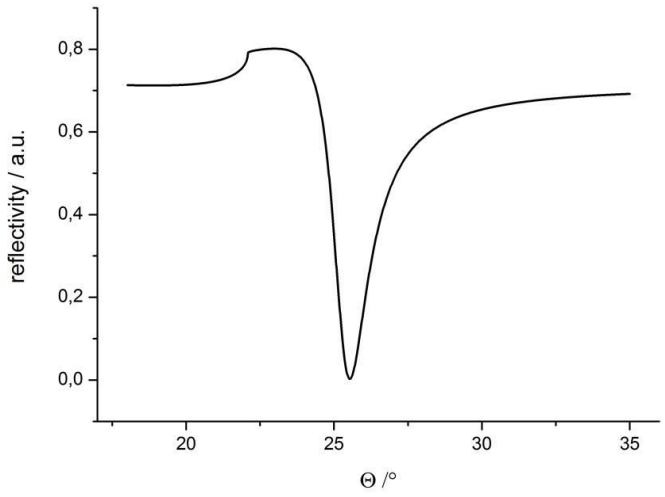

Fig. 2.7: Reflectivity as function of angle of incidence for a layer system: prism (n = 1.845)/gold (d = 50 *nm*, n = 0.18, κ = 3.45)/air (n = 1).

The surface plasmon resonance is particularly sensitive for refractive index changes of the surrounding medium. Figure 2.8 shows a glass/gold system simulated (black) with air as the environmental medium. The illustration shows calculated angle spectra, where the refractive index of the surrounding dielectric medium increases. Rising refractive indices moved the resonance minimum to larger angles. The form of the response did not change. This shift can be resolved in time by measuring the reflectivity at a certain angle. Another kinetic modus is the tracking of the resonance minimum.

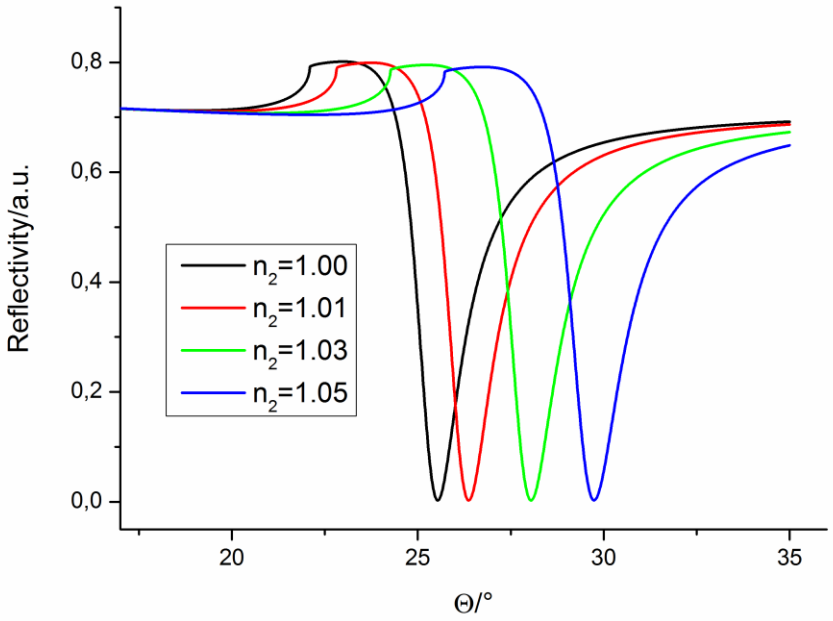

Fig. 2.8: Reflectivity for different refractive indices of dielectric medium, layer system prism (n = 1.845)/gold (d = 50 nm, n = 0.18, κ = 3.45)/air (n_2 = 1, n_2 = 1.01, n_2 = 1.03, n_2 = 1.05).

Another notable effect occurs if the directly adjacent dielectric represents an intermediate layer with a thickness in the order of the penetration depth of the evanescent surface plasmon field. This is illustrated in figure 2.9, showing the angular position of the surface plasmon resonance for various dielectric layer thicknesses.

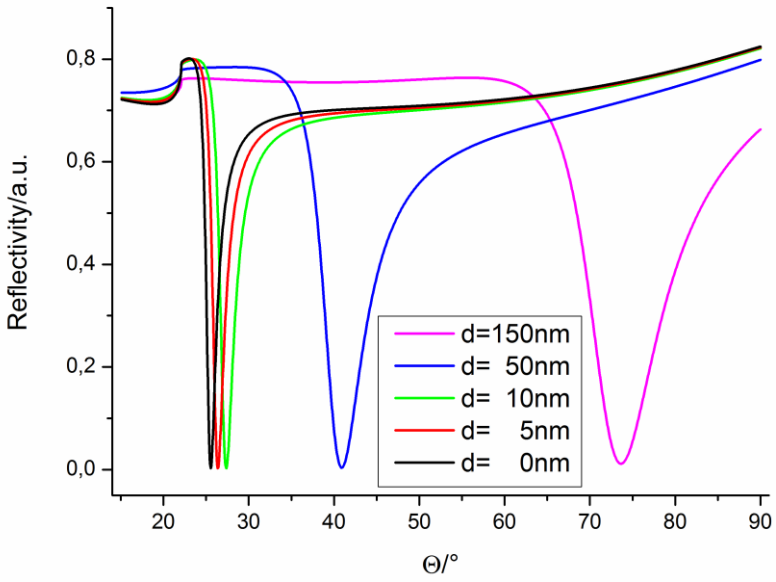

Figure 2.9: *SPR* spectra without and with additional dielectric layer. As basis for the calculations the following parameters were used: prism (n = 1.845)/gold (d = 50 *nm*, n = 0.18, κ = 3.45)/ dielectric layer (n = 1.5, d = 5 *nm*, d = 10 *nm*, d = 50 *nm*, d = 150 *nm*)/air (n = 1).

Based on the angular position for $d_1 = 0$, the surface plasmon response shifted with increasing dielectric layer thickness to larger angles and converges for $d \rightarrow \infty$ against the resonance angular position that applies for the dielectric half-space.

Note that the *SPR* minimum moved about 50 degrees for $d = 0$ to $d = 150$ *nm*. Due to an angle resolution < 0.01 in the experiment very interesting applications for the determination of layer thickness in the nanometer range occur. [12.15] It can also be used for time measurements of thickness increases recorded during the production of dielectric layers in real time. This is, of course, only true for thin layers, in terms of the penetration depth of evanescent surface plasmon field. Therefore, the resonance condition still differs from those for $d \rightarrow \infty$. For the example shown in Figure 2.9 the range of layer thickness is less than 300 *nm* because of the penetration depth of the evanescent field. For larger thickness of the dielectric layer the response converges to the angle for $d \rightarrow \infty$.

However, thickness determination is also possible if the layer thickness is greater than about $\lambda/2$. Then a configuration of so-called metal film enhanced leaky waveguide mode resonances come into effect. These resonances are quasi-modes, which spread in the dielectric

layer, called leaky modes or leaky waves. Together with the surface plasmon resonance they form the basis of the so-called metal film enhanced leaky waveguide spectroscopy. It is discussed in the following section.

2.5 Metal Film Enhanced Leaky Waveguide Modes

If the thickness of the dielectric layer is further increased, a new type of nonradiative waveguide modes can be observed. This is schematically shown in Fig. 2.10. The excitation of these modes of different order *m* can be seen again if the reflected intensity is recorded as a function of the angle of incidence: narrow dips in the reflectivity scan versus Θ indicate the existence of various waveguide modes.

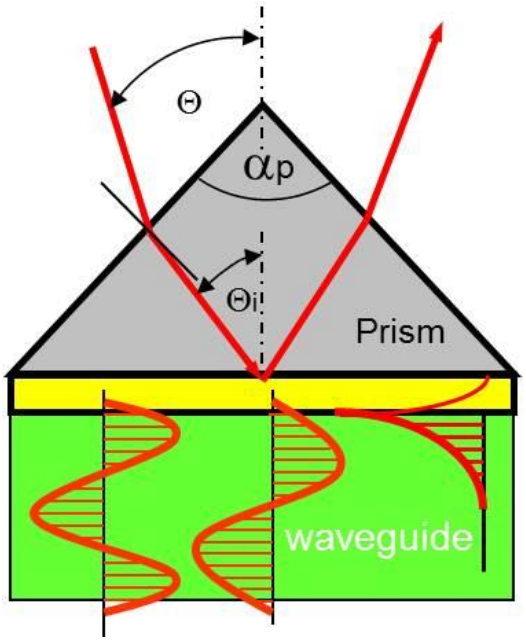

Figure 2.10: Excitation scheme with the optical field distributions of surface plasmon resonance and metal film enhanced leaky waveguide modes in Kretschmann configuration.

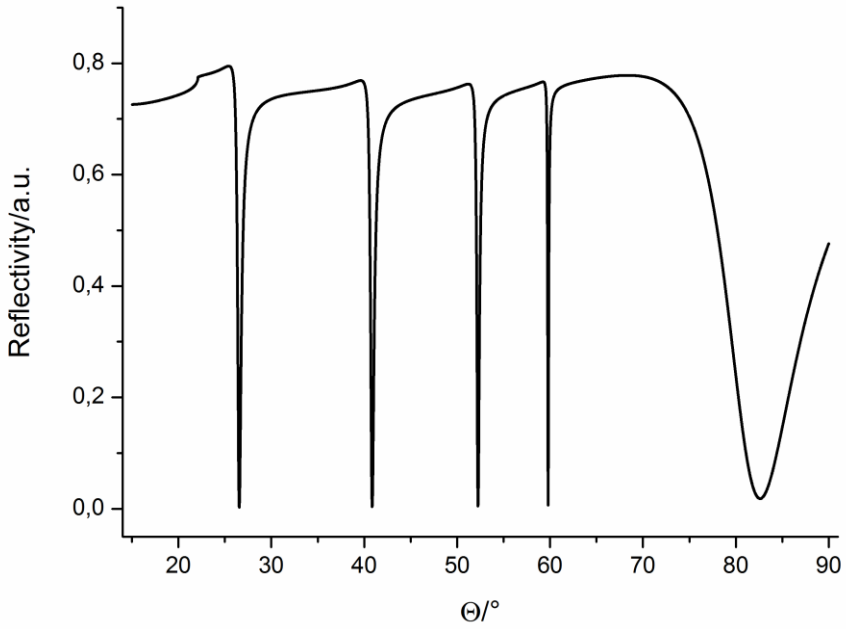

Figure 2.11: Simulated reflectivity spectrum for a slap waveguide in the Kretschman configuration with prism (n = 1.845)/gold (d = 50 *nm*, n = 0.18, κ = 3.45)/ dielectric waveguide layer (n = 1.5, κ = 0, d = 1200 *nm*)/air (n = 1).

However, in this specific layer configuration the propagation constant *ß* are becoming complex. The reflectivity scan provides insightful information about the concerned layer system. The shape of all resonances depends on the optical parameters (d, n, κ) of the layers. The angular position of the surface plasmon resonance is, as already discussed, mainly determined by the refractive index of the dielectric. The waveguide modes angular position and the number of resonances will be set by the refractive index and the thickness of the dielectric layer, respectively. Additionally the waveguide modes show a huge dependency on the imaginary part of the dielectric layer refractive index κ.

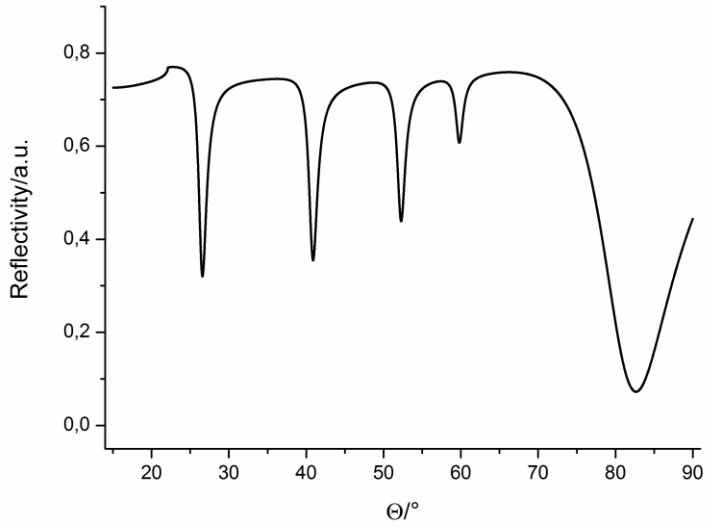

Figure 2.12: Simulated reflectivity for a slap waveguide with $\kappa = 0.005$. Parameters used: prism (n = 1.845)/gold (d = 50 *nm*, n = 0.18, $\kappa = 3.45$)/ dielectric waveguide layer (n = 1.5, $\kappa = 0.005$, d = 1200 *nm*)/air (n = 1).

In contrast to the surface plasmon resonance the waveguide modes exist also for *TE* (s) polarized light. The *TE* modes show a lower full maximum half with (*FMHW*) as the *TM* modes, also a slightly lower coupling efficiency.

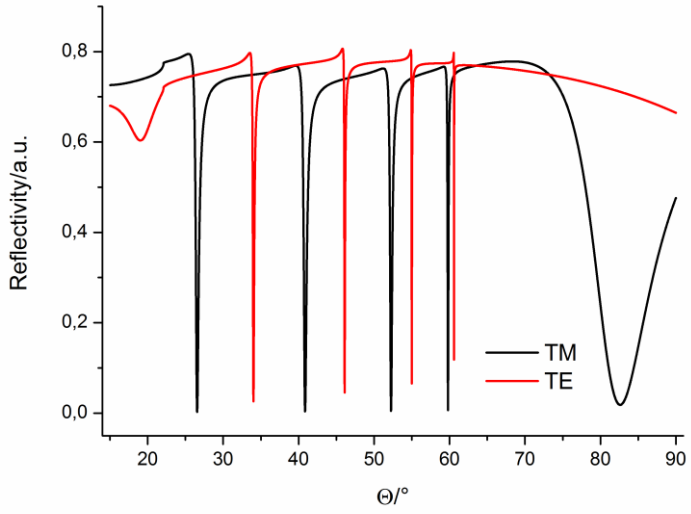

Figure 2.13: Simulated reflectivity for *TM* and *TE* polarized light. Slap waveguide in the Kretschman configuration with prism (n = 1.845)/gold (d = 50 *nm*, n = 0.18, $\kappa = 3.45$)/ dielectric waveguide layer (n = 1.5, $\kappa = 0$, d = 1200 *nm*)/air (n = 1).

By an evaluation of measured reflection spectra with the transfer matrix formalism, a coating system can be fully characterized on the optical parameters of each individual layer. The angular position and the shape of the modes provide detailed information on all optical layer parameters (n, κ and d).

The different field distributions of the modes are very useful for characterization of refractive index profiles. While the surface plasmon mode probes the area close to the interface, the waveguide mode probes the bulk behaviour of the dielectric layer.

2.6 Reversed Wentzel-Kramers-Brillouin-Approximation (*rWKB*)

The reversed Wentzel-Kramers-Brillouin (*rWKB*) approximation was utilized to evaluate the refractive index gradient in *x*-direction (normal to the substrate). This method is commonly applied for the analysis of planar waveguide gradient index profiles with smooth variation [17]. It is based on the fundamental idea that each waveguide mode has a different field distribution and probes different areas of the film. A detailed description is given in the literature, which is discussed very briefly in the following [16,17]. And it´s based on the scalar wave function for *x*-dependency of the refractive index.

$$\frac{\partial^2 H_y}{\partial x^2} + \left(k_0^2 n^2(x) - \beta^2\right) H_y = 0 \qquad (2.32)$$

The approach for the *x*-dependency of the amplitude and phase is:

$$H_y = H_0 e^{jk_0\Phi(x)} \qquad (2.33)$$

It is expanded in series. By summarizing the terms of the same order, the zero and first order of *rWKB*-approximation yields:

$$\Phi_0 = \frac{1}{k_0}\int \sqrt{k_0^2 n^2(x) - \beta^2}\, dx \tag{2.34}$$

$$\Phi_1 = \frac{i}{2}\ln\left|\frac{d\Phi_0}{dx}\right| \tag{2.35}$$

One is an oscillating solution:

$$H_y = \frac{H_0}{\sqrt[4]{k_0^2 n^2(x) - \beta^2}} e^{\pm j\int \sqrt{k_0^2 n^2(x) - ß^2}\, dx} \tag{2.36}$$

The other one is an evanescent solution:

$$H_y = \frac{H_0}{\sqrt[4]{ß^2 - k_0^2 n^2(x)}} e^{\pm\int \sqrt{ß^2 - k_0^2 n^2(x)}\, dx} \tag{2.37}$$

for $k_0^2 n^2(x) < ß^2$. At the point of discontinuity the one solution merges into the other (after connecting linearly). This transition point (x_d) is the integration limit for eq. 2.36, introducing the effective refractive index sensed by each waveguide mode, for $n_2 - n_1 << n_1$:

$$\int_0^{x_d} \sqrt{n^2(x) - n_{eff}^2}\, dx = \frac{\lambda_0}{2}\left(N + \frac{3}{4}\right) \tag{2.38}$$

With N=0,1,2,…

Experimentally, n_{eff} is calculated by the measured coupling angle for each mode, e. g. for the Kretschmann configuration in Fig. 2.10:

$$n_{eff} = n_p \sin\left(\frac{\alpha_p}{2} + \arcsin\left(\frac{\sin\Theta}{n_p}\right)\right) \tag{2.39}$$

Here, the refractive index of the prism is n_p, α_p the prism angle and Θ_m the resonance angle of the mode. The refractive index $n^2(x)$ can be approximated according to:

$$n^2(x) = n_{eff,k}^2 + \frac{n_{eff,k-1}^2 - n_{eff,k}^2}{x_k - x_{k-1}}(x_k - x) \tag{2.40}$$

With $x_{k-1} < x < x_k$ and $k = 1, 2, \ldots, m$

Combined with eq. 2.38, the measured effective refractive index n_{eff} of each waveguide mode can be assigned to a distance from the substrate interface by a recursive procedure:

$$\frac{x_m - x_{m-1}}{\lambda_0} = \frac{1}{\sqrt{n_{eff,m-1}^2 - n_{eff,m}^2}}\left(\frac{3(4m-1)}{16}\right) - \sum_{k=1}^{m-1}\frac{x_k - x_{k-1}}{\lambda_0(n_{eff,k-1}^2 - n_{eff,k}^2)} \times\left[\left(n_{eff,k-1}^2 - n_{eff,m}^2\right)^{3/2} - \left(n_{eff,k}^2 - n_{eff,m}^2\right)^{3/2}\right] \tag{2.41}$$

Experimentally, from the angular minimum of each waveguide mode, an effective refractive index n_{eff} can be derived. This effective refractive index n_{eff} equals the physical refractive index n at a defined lateral position x of the film, at which the oscillating and evanescent solutions of the wave equation coincide. Each waveguide mode allows the determination of one (x, n)-pair, which constitutes a distinct point on the refractive index profile. However, *rWKB* cannot provide the refractive index at the interface to the gold substrate (position $x = 0$) since the waveguide modes

cannot probe the area only close at the interface. *SPR* is located at the gold interface with a typically penetration depth of 200 *nm* into the gel. By novel combination of *SPR* and *rWKB* the entire refractive index profile is describable with high accuracy.

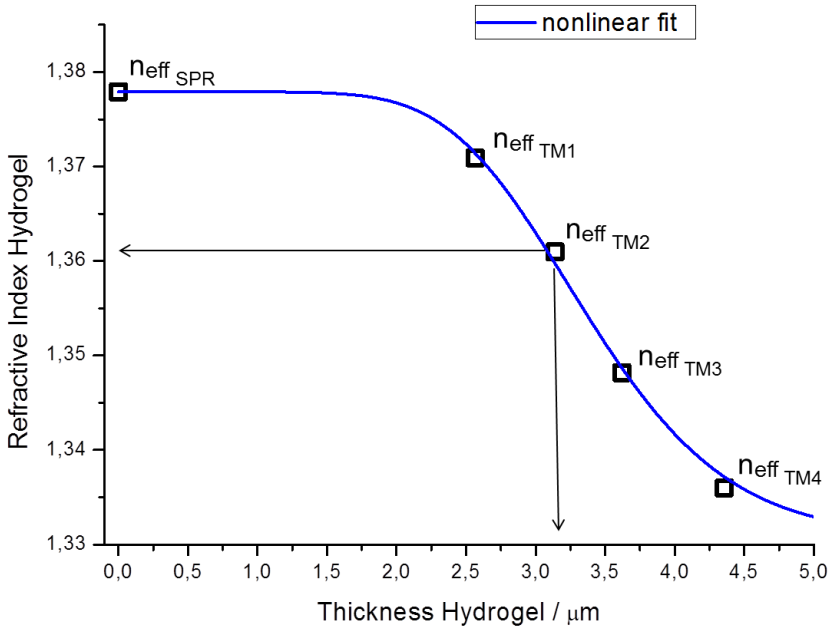

Figure 2.14: Refractive index profile calculated with *rWKB* for *TM* modes at λ = 632.8 *nm* of a hydrogel in the swollen state. The blue line is a fit to a nonlinear diffusion profile.

This is shown in Fig. 2.15 together with a fit for a nonlinear diffusion profile proposed in Ref. [20]:

$$n(x) = n_{Cover} + \frac{\Delta n}{\chi}\left[1-(1-\gamma)^{erfc(x/d_f)}\right] \qquad (2.42)$$

In this equation n_{cover} is the refractive index of the cover material (e.g. water), Δn is the maximum increase of the refractive index, χ is a material constant and d_f is the effective layer thickness.

The combination of *SPR* and the *rWKB* approximation provided detailed information on the refractive index profile in a hydrogel layer. To further exploit this information and to validate the *rWKB* approximation, the profiles were subdivided into several layers of uniform refractive index (Fig.2.15). Then, the surface plasmon resonance / optical waveguide spectroscopy

(*SPR/OWS*) data were simulated with this multiple slap approach by the transfer matrix algorithm. For each waveguide mode *rWKB* data point maximum one sublayer was fitted. The border between two sublayers was set symmetrically between two adjacent *rWKB* data points. Using this multilayer model, for each individual sublayer perpendicular to the surface the local refractive index n and the corresponding imaginary part κ was calculated by fitting the reflectivity with transfer matrix algorithm. This imaginary part κ is a measure for optical losses like absorption or scattering losses by homogeneities in the layer.

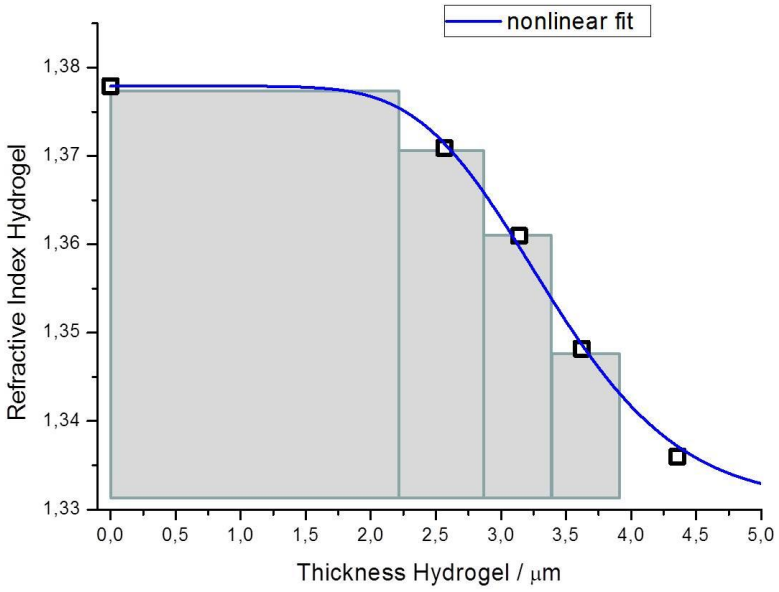

Fig. 2.15: Multilayer model based on a refractive index profile of a swollen hydrogel film.

2.7 Effective Medium Theory

To calculate the reflection of a layer stack with the transfer matrix formalism, it is assumed that the layers are homogeneous. However, often films are a mixture of several components, e.g. swollen hydrogels films. It can also occur that films have an interfacial roughness (film/air mixture), which cannot be neglected. If the spatial scale of the mixture or roughness is much smaller than the wavelength of light ($< \lambda/10$), we assume the layer as homogeneous and determine the properties of the film with an effective-medium theory (*EMT*)

[18]. The simplest effective-medium theory can be derived from the Clausius-Mosotti equation, which links the molecular polarizability with the refractive index of a material [21]:

$$\frac{n^2-1}{n^2+2}=\frac{1}{3\varepsilon_0}N\alpha \tag{2.43}$$

with α the polarizability of a molecule, and N the number of molecules per volume unit. For a substance mixed at the molecular level this equation is extended to:

$$\frac{n^2-1}{n^2+2}=\frac{1}{3\varepsilon_0}\sum_i N_i\alpha_i \tag{2.44}$$

Combined with eq. 2.43 the Lorentz-Lorenz theory follows:

$$\frac{n^2-1}{n^2+2}=\sum_i f_i\frac{n_i^2-1}{n_i^2+2} \tag{2.45}$$

with f_i the volume fraction of the material i, and $\Sigma f_i = 1$. If the materials are not mixed at the atomic level, it can be handled as a mixture of dielectric materials. An entire *EMT* family follows from the observation of microscopic operations. [13,15].

$$\frac{n^2-n_h^2}{n^2+\left(\frac{1}{\gamma}-1\right)n_h^2}=f_1\frac{n_1^2-n_h^2}{n_1^2+\left(\frac{1}{\gamma}-1\right)n_h^2}+f_2\frac{n_2^2-n_h^2}{n_2^2+\left(\frac{1}{\gamma}-1\right)n_h^2} \tag{2.46}$$

with n_h the refractive index of the host material, and γ a geometry factor $0 \le \gamma \le 1$, which is based on the micro-structure of the mixture. A common *EMT*, for example, is the Bruggeman-theory

with $n_h = n$ and $\gamma = 1/3$. The Bruggeman-theory is well suited to describe mixtures of roughly the same volume fractions of mixed materials [19]:

$$0 = f_1 \frac{n_1^2 - n^2}{n_1^2 + 2n^2} + f_2 \frac{n_2^2 - n^2}{n_2^2 + 2n^2} \tag{2.47}$$

From eq. 2.46 with $\gamma = 0$ and $\gamma = 1$ follows the upper and lower limit of n, the Wiener-bounds:

$$n^2 = f_1 n_1^2 + f_2 n_2^2 \tag{2.48}$$

$$\frac{1}{n^2} = f_1 \frac{1}{n_1^2} + f_2 \frac{1}{n_2^2} \tag{2.49}$$

In Fig. 2.16 the water volume fraction is calculated for Bruggeman *EMT* with Wiener bounds. As a consequence, the water/polymer content of the mixture can be determined from the measurement of the refractive index even without knowledge of the full details of the polymer blend microstructure.

$$f_p = \frac{n - n_{H2O}}{n_p - n_{H2O}} \tag{2.50}$$

Here f_p is the polymer volume fraction. This polymer example has a direct relation to the later characterized hydrogel films, which have approximately the same refractive index (n = 1.5). Often the volume swelling ratio is used for the characterization of hydrogels. This is defined as:

$$\Phi = \frac{1}{f_p} \tag{2.51}$$

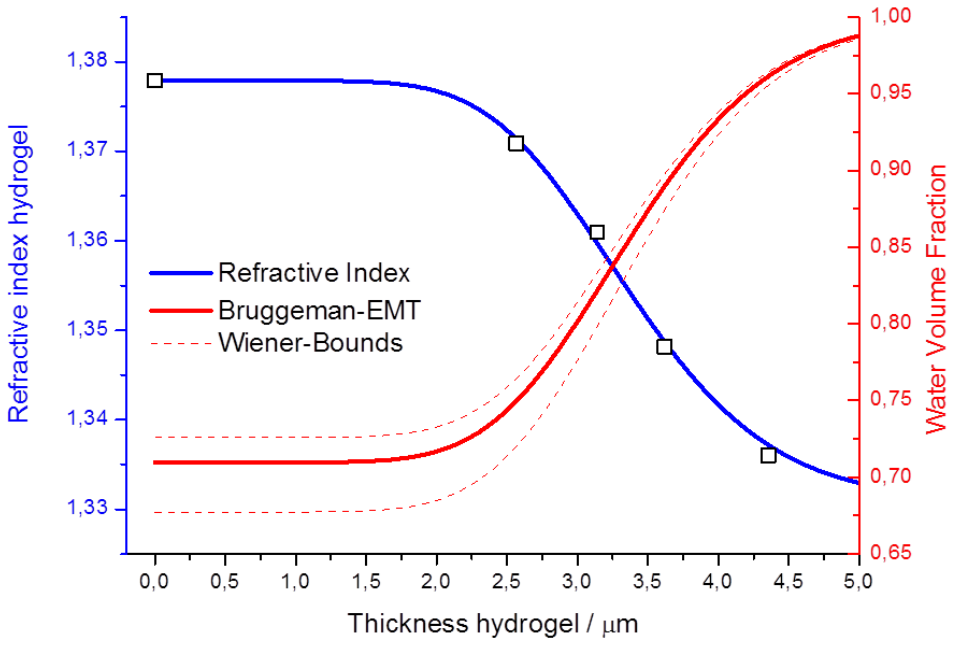

Fig. 2.16: Water volume fraction of a hydrogel calculated by the Bruggeman *EMT* from a refractive index profile.

This novel approach to analysing refractive index profiles allowed the characterization of polymer/water volume fractions of inhomogeneously swollen hydrogel films at each position.

References

[1] Knoll, W. *Annu. Rev. Phys. Chem.* 1998, *49*, 569
[2] Chilwell, J. and Hodgkinson, I., *J. Opt. Soc. Am. A* 1, 1984, 742
[3] Walpita, L.M., *J. Opt. Soc. Am. A* 2, 1985, 595
[4] Yeh, P., Opical Waves in Layere Media. Wiley Interscience, 2005
[5] Yeh, P., Optical Waves in Layered Media, Wiley, New York, 1988, Chap. 11
[6] Homola, J. and Slavik, R., *Electon. Lett.* 32, 1996, 480
[7] Ronot-Trioli, C.; Trouillet, A.; Veillas, C.; A. El-Shaikh and H. Gagnaire: *Anal. Chim. Acta* 319, 1996, 121
[8] Liedberg, B.; Nylander, C. and Lundström, I., *Sensors and Actuators* 4, 1983, 299
[9] Sprokel G.J. and Swalen, J.D., Handbook of Optical Constants of Solids II, Academic Press, Boston, 1991, 75-95
[10] Knoll, W.; Hickel, W and Sawodny, M., Integrated Optics and Micro-Optics with Polymers, Teubner, Stuttgart, 1993, 89-112
[11] Gordon J.G. and Swalen, J.D., *Opt. Commun.* 22, 1977, 374
[12] Sprokel G.J. and Swalen, J.D., Handbook of Optical Constants of Solids II, Academic Press, Boston, 1991, 75-95
[13] Kretschmann E. und Raether, H., *Z. Naturforsch.* 23A, 1968, 2135
[14] Raether, H., Academic Press, New York, 1977, 145
[15] Knoll, W.; Hickel, W. and M. Sawodny, M., Integrated Optics and Micro-Optics with Polymers, Teubner, Stuttgart, 1993, 89-112
[16] Pochi, Y., Wiley, 1988
[17] Karthe W. and Müller, R., Integrierte Optik, Akademische Verlagsgesellschaft Geet & Portig Leipzig, Germany 1991
[18] Choy, T.C., Effective Medium Theory. Oxford University Press, 1999.
[19] Aspnes, D.E., Thin Solid Films, 1982, 89:249–262.
[20] Linares, J.; Prieto, X; Montero, C., Opt. Mater. 3 _1994. 229.
[21] Born, M., Optik, Springer 1972

3 Experimental Methods

3.1 Surface Plasmon Resonance /Optical Waveguide Spectroscopy (*SPR/OWS*)

SPR/OWS spectra were recorded in the Kretschmann configuration with a customized setup shown in Fig. 3.1 [1]. A *LaSFN9* glass (refractive index n = 1.8449, corresponding to $\varepsilon' = 3.404$) was optically matched to the base of a *LaSFN9* glass prism. The sample was placed in a heatable and coolable flow cell ($\Delta T = 0.1K$), and subsequently filled with MilliQ water. Monochromatic light (He/Ne laser, λ = 632.8 *nm*, Uniphase) was directed through a linear, transverse magnetic (*TM, p*) polarization (Glan-Thompson polarizer, B. Halle) and the prism. The external angle of incidence θ was varied with two-cycle goniometer (Huber).

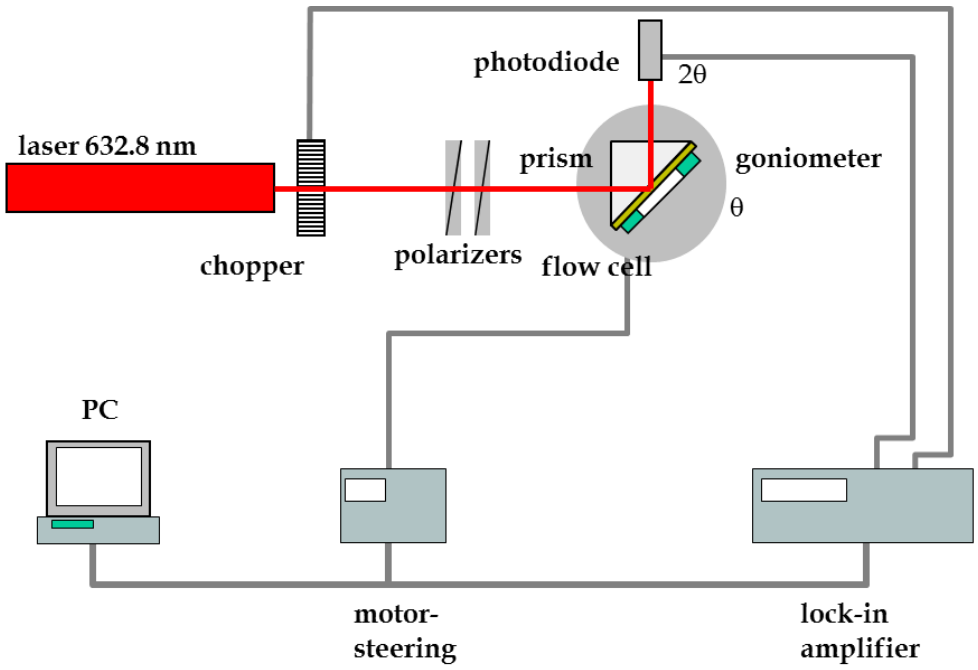

Figure 3.1: Schematic of SPR/OWS setup.

Angle-dependent intensities $I(\theta)$ were recorded with a BPW 34 B silicon photodiode (Siemens). The angular dependence of the reflectivity was modelled by the Fresnel matrix formalism (Chapter 2) for a multilayer system. Thus, the *SPR/OWS* scans yielded information about the

complex refractive indices $n + i\kappa$ of these layers. The relation of the complex refractive index to the dielectric function ε is given by eq. 3.1.

$$\varepsilon = \varepsilon' + i\varepsilon'' = (n + i\kappa)^2 \tag{3.1}$$

The real part of the complex refractive index, *n*, is determined by the angular minima of the resonances of the surface plasmon and the optical waveguide modes. The imaginary part κ can be calculated from the width and depth of the peaks and is a measure for the light intensity loss in the system. Thus, it allows further conclusions about the optical properties of the hydrogel as will be discussed in Chapter 4.

3.2 Waveguide Mode Spectroscopy (*WaMS*)

Waveguide mode spectroscopy is a highly sensitive method to characterize optical properties of thin films on top of a waveguide [2]. It has already been demonstrated that *WaMS* is suitable for highly sensitive ex-situ characterization of thickness and refractive index of thin plasma polymer films [3].

Here, very thin planar waveguides of high refractive index with only a TE_0 and a TM_0 modes are used (Figure 3.2). They produce evanescent fields which small decay lengths but extremely high fields at the waveguide surface.

By adding an adlayer onto the surface of a waveguide sensor the refractive index of the waveguide's surrounding environment changes, this leads to a new waveguide mode resonance condition and in a change in the penetration depth of the evanescent field of the waveguide modes. This in turn induces changes in the effective refractive indices, $n_{eff,TE0}$ and $n_{eff,TM0}$ of the guided modes.

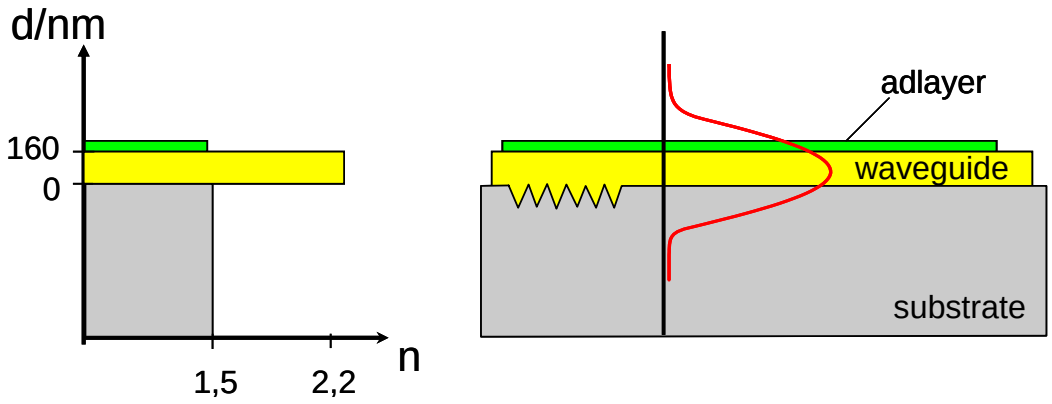

Figure 3.2: Waveguide sensor with high refractive index waveguiding layer

The determination of the propagation constants of waveguide modes is an established procedure for the evaluation of the layer thickness and refractive index of a waveguide [4]. It is based on the selective excitation of waveguide modes by means of a prism or a diffraction grating. The refractive index and the thickness of the layer can be calculated from the measured effective refractive indices of the different modes ($n_{eff,i,j}$ where i,j are the polarization of the light and mode number) using the dispersion relation, with the assumption that the refractive index distribution within the layer is in the form of steps (eq. 2.25 and 2.26). The effective refractive index provides the phase velocity of the guided mode ($\varpi = c / n_{eff}$), where c = is the velocity of light in a vacuum. Changes in the effective refractive index, Δn_{eff}, can be measured using a grating coupler. A laser beam can be coupled into the planar waveguide at an angle of incidence Θ if the in-coupling condition:

$$n_{eff} = n_C \sin \theta + I \lambda / \Lambda \qquad (3.2)$$

is satisfied. n_C is the refractive index of the covering medium (air or solvent), λ the wavelength of the laser used, I the diffraction order and Λ the grating period. Thus, if, for example, a hydrogel film is deposited as an adlayer onto the waveguide, its optical parameters (thickness d_a, and refractive index n_a) change the effective refractive indices n_{eff} of the waveguide modes. The effective index shift Δn_{eff} can be determined from eqn. (3.2) above, by measuring the change $\Delta\Theta$. The thickness d_a and refractive index n_a of the adlayer can be calculated from the effective index

shifts $\Delta n_{eff,\,TE0}$ and $\Delta n_{eff,\,TM0}$.

Alternatively to the prism coupling described for *OWS*, a grating with periodicity Λ, incorporated into the waveguide can used to couple a HeNe laser beam **(**λ = 632.8 *nm***)** into the waveguide. $n_{eff,i,j}$ can be determined by scanning the angle of incidence of the incoming laser beam onto the grating, while the in-coupled power is measured by two photo-detectors at both ends of the waveguide. Such waveguides are designed for optimal sensitivity for the zeroth transversal electric, TE_0, and transversal magnetic, TM_0, modes.

3.2.1. Sensitivity

A high refractive index material is favourable for the waveguide layer, since this allows for a relatively thin waveguide thickness, which will still guide optical modes. Thus, a high degree of field localization is obtained, which provides a high sensitivity for the thin film characterization [2]. Furthermore, low optical losses are required to avoid damping of the waveguide modes. The waveguide material chosen here was Tantalpentoxide Ta_2O_5 (n_{wg} = 2.22, at a wavelength $\lambda = 632.8$ *nm*) deposited on a quartz glass substrate, which is known for its excellent waveguide performance [3]. The substrate material was fused silica with a low refractive index (n_s = 1.457 at $\lambda = 632.8$ *nm*). A low substrate index leads to a fast decay of the evanescent field in the substrate, thus again resulting in a strong field localization. The choice of the waveguide thickness depends on the number of guided modes required for the calculation of the adlayer parameters of interest. Due to translation invariance in the direction orthogonal to both the waveguide interface normal and the propagation direction, guided modes of two independent polarizations exist: the transverse magnetic (TM_0, TM_1,...) and the transverse electric (TE_0, TE_1,...) polarization. The thicker the waveguide the higher is the number of orders of the guided modes. Fig. 3.3 shows the result of sensitivity determinations of the zero and first order modes based on simulation data. The change of the n_{eff} caused by an increase of the adlayer thickness (n_a = 1.50) is plotted as a function of the thickness of the waveguide layer (n_{wg} = 2.22) on a fused silica substrate as described. The simulation uses the Transfer-Matrix method (chapter 2.1) to compute the optical response of a multi-layer system with plane interfaces. Fig. 3.3 demonstrates that the sensitivity of each waveguide mode increases rapidly as the thickness of the waveguide increases. The sensitivity reaches a maximum and decreases slowly. As the thickness

of the waveguide increases, the number of modes available for sensing increases, however, at the same time, the sensitivity decreases. Two guided modes are sufficient to characterize two parameters, the thickness *d* and the refractive index *n* of a deposited layer, by assuming isotropic behaviour.

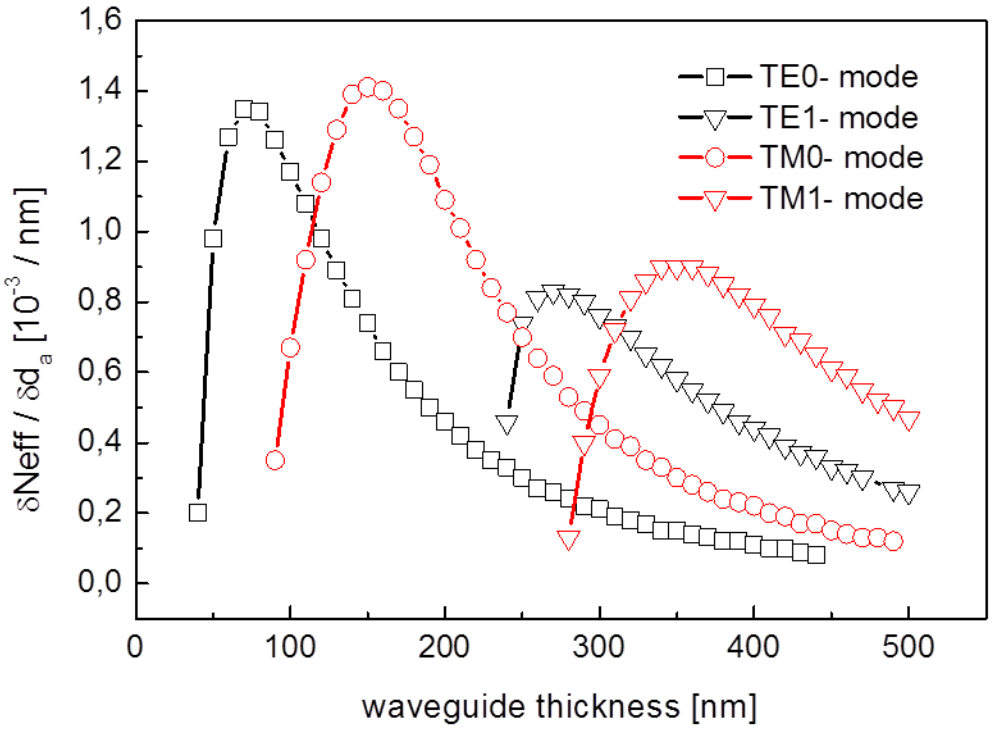

Figure 3.3: Simulated changes of the effective refractive indices normalized to the thickness of an adlayer with $n_a = 1.50$ are plotted as a function of the thickness of the waveguide with $n_{wg} = 2.22$ on a fused silica substrate ($n_s = 1.457$) in air at a wavelength of 632.8 *nm*.

3.2.2 Setup

The experiments were carried out using a home-built waveguide spectrometer (Figure 3.4). A grating with periodicity Λ, incorporated into the waveguide was used to couple a HeNe laser beam **($\lambda = 632.8$ *nm*)** from the external cover medium into the waveguide. $n_{eff\ i,j}$ can be determined by scanning the angle of incidence of the incoming laser beam onto the grating, while the in-coupled power is measured by two photo detectors situated at both ends of the waveguide. Figure 3.4 shows the principle for a grating coupling measurement. The waveguide sensor

carrying a coupling grating is rotated on a goniometer, systematically changing the angle of incidence from the chopped laser with adjusted polarization. Detectors at the ends of the waveguide sensor detect the modes as peaks, when light is coupled and guided to them. The waveguide sensor is connected to a cuvette with a liquid handling system. A lock-in amplifier is used to maximize the signal-to-noise ratio.

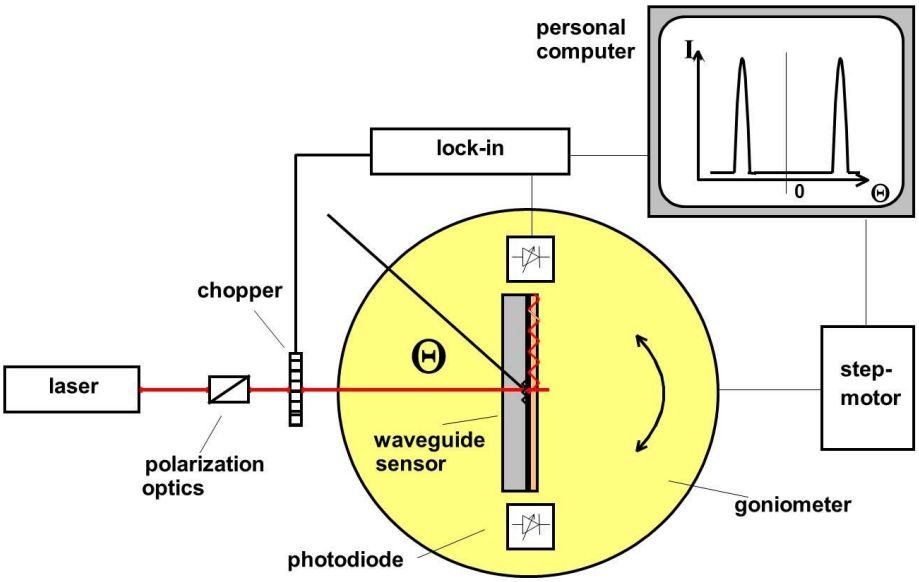

Figure 3.4: Experimental setup for detection of waveguide mode coupling angles.

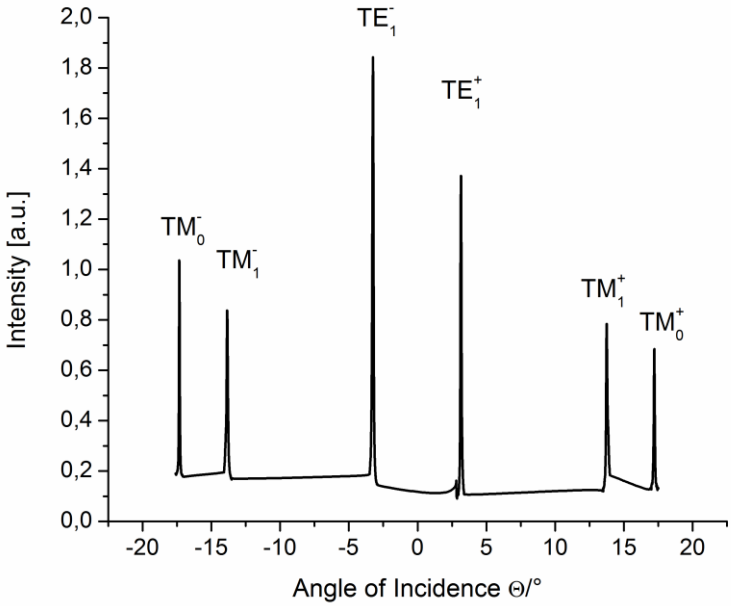

Figure 3.5: Intensity peaks of excited waveguide modes

3.2.3. Determination of *n* and *d*

The optical experiment results in a shift of the coupling angles of the guided modes during thin film deposition onto the surface of the waveguide. Momentum matching on a grating leads to the coupling condition for a laser beam with an angle of incidence Θ and n_{eff} of the guided mode (see Eq. 3.2). Using this relationship, n_{eff} is determined from the coupling angle for each mode separately. As the refractive index of the adlayer is higher than that of the surrounding medium, this results in a partial increase of the refractive index of the surrounding medium. Thus, for each mode a higher n_{eff} is observed, illustrated very clearly in Eq. (3.2). The Transfer-Matrix method was used to compute *d* and *n* of the deposited layer. The input parameters for this calculation are the bulk refractive indices of the substrate and surrounding medium as well as the thickness and refractive index of the bare waveguide. These parameters, therefore, have to be known accurately. The bulk substrate index, n_{s}, can be obtained from the manufacturer, $n_{\mathrm{fused\ silica}} = 1.457$ at $\lambda = 632.8\ nm$, and $n_{\mathrm{air}} = 1.000$ are literature values. The coupling angles prior to deposition were used to calculate thickness and refractive index of the bare waveguide. The result of the Transfer-Matrix method for a four-layer device consisting of the substrate, the waveguide, the deposited thin film and the surrounding air is a system of two non-linear equations. These equations are solved by constructing a function by adding the square of the two equations and minimizing it according to Powel's method [4].

As long as at least two modes are found and the optical data of the substrate are known, the thickness and the refractive index of the waveguide material can be obtained with the help of the effective refractive indices of the modes and an iterative computer routine based on a procedure proposed by Ulrich and Torge [5–7].

There are two main advantages in using functional minimization to solve the Transfer-Matrix problem. Firstly, this method shows a good numerical stability. Secondly, the function left after minimization, which should ideally be the zero-function, can be used to detect problems during parameter calculation, if this function differs significantly from zero. The minimization was performed for each data point individually without using the previous values of *n* and *d* as starting values. Consequently, no errors are smoothed out during the determination of *n* and *d*, so that any fluctuations in the *n* and *d* kinetics observed in this work reflect the sensitivity of the method.

References

[1] Schasfoort, R.B.M., Tudos, A.J., *Handbook of Surface Plasmom Resonance*, RSC 2008.

[2] Lukosz, W., Biosensensors & Bioelectronics 6,1991, 215.

[3] van Os, M.T., Menges, B., Förch, R., Vancso, G.J., Knoll, W., Chem. Mater. 11, 1999, 3252.

[4] Press, W.H., *Numerical Recipes in Pascal*, Cambridge University Press, Cambridge, 1989.

[5] Ulrich, R. and R. Torge, R, *Measurement of thin film parameters with a prism coupler*, Appl. Opt. 12, 1973, 2901–2908.

[6] Karthe, W and Müller, R, *Integrierte Optik*, Akademische Verlagsgesellschaft Geest & Portig, Leipzig, 1991.

[7] Liu, T. and Samuels, R.J., *Physically corrected theoretical prism waveguide coupler model*, J. Opt. Soc. Am. A 21, 2004, 1322–1333.

4 Analysis of Optical Gradient Profiles

The analysis of optical gradient profiles and temperature-dependent swelling of thin thermo-responsive hydrogel films was a cooperation with Matthias J. N. Junk, who performed the measurements Ilke Anac and Ulrich Jonas. This section is already published [1].

4.1 Introduction

Polymers based on N-isopropylacrylamide (*NiPAAm*) are one of the most intensely studied representatives of responsive polymer materials. The homopolymer exhibits a lower critical solution temperature (*LCST*) in water close to body temperature (33°C) [2]. Through a temperature increase above the *LCST*, because of a changing balance between hydrophilic and hydrophobic interactions, the polymer-water mixture phase separates [2,3]. Due to this externally triggered phase transition, responsive materials offer a large variety of possible applications in biology, medicine, and pharmaceutics and as sensors and actuators [4-7]. Besides temperature also varying salt concentration can trigger a volume collapse in many responsive gels, which is of particular importance for biosensor applications involving salt-containing sample media [8]. With the advent of nanotechnology, thin surface-attached films of responsive polymers received considerable attention. The unique properties of these thin responsive films were studied by various techniques such as neutron scattering [9,10], photon and fluorescence correlation spectroscopy [11,12], atomic force spectroscopy [13], ellipsometry and surface plasmon resonance (*SPR*) spectroscopy [14-18].

SPR is a powerful tool to study the optical properties of polymers as thin films and yields information about thickness and refractive index [19]. Yet, an independent determination of both variables only by *SPR* is not possible. However, when polymer films are sufficiently thick (> 500 *nm*), optical waveguide modes can be excited and observed in addition to the surface plasmon resonance. This combination of *SPR* with optical waveguide mode spectroscopy (*OWS*) allows independent characterization of the thickness and refractive index at a single experimental wavelength [17,19].

A common method for the analysis of *SPR/OWS* data assumes a homogeneous refractive index for the entire polymeric layer. As recently shown for several polymer systems, this so-called box model is not always appropriate since it exhibits a pronounced refractive index gradient perpendicular to the surface [9,18,20]. The primary cause for the anisotropy in the surface-grafted films is to be found in the covalent surface attachment via the benzophenone anchor layer, which restricts lateral expansion and leads to quasi-1D swelling away from the substrate-hydrogel interface. This optical gradient profile is accessible by a combination of *SPR/OWS* with the reversed Wentzel-Kramers-Brillouin (*rWKB*) approximation [18,21].

Polymer volume fraction profiles of thin hydrogel films were previously studied by several methods. Habicht et al. and Toomey et al. investigated polymer brushes and crosslinked polymer films based on styrene and dimethylacrylamide by multiple-angle nulling ellipsometry and modelled the gradient profiles for various crosslinking densities using an effective medium approximation [20,22].

Vidyasagar et al. [9], Seitz et al. and Yim et al. [10] used neutron scattering to reveal temperature-dependent changes of the volume fraction profiles of surface-attached *pNiPAAm* networks. Mendez et al. chose a computational approach based on self-consistent field (*SCF*) theory [23].

In this chapter, the temperature- and salt-driven collapse of an inhomogeneous hydrogel film was characterized by *SPR/OWS* in combination with the *rWKB* approximation. The refractive index profiles obtained by *rWKB* were used to perform a multi-layer simulation of the measured data, and successive application of the Fresnel formalism with transfer matrix algorithm (see chapter 2.1) to the individual sublayers. This provides spatially resolved information about the complex refractive index. The imaginary part carries the information about light intensity loss inside the hydrogel sample. These optical losses are interpreted as scattering losses due to network inhomogeneities which can be localized and assigned to defined slabs perpendicular to the hydrogel film surface.

The responsive thin hydrogel film studied here consisted of a lightly photo-crosslinked terpolymer based on *NiPAAm* [16]. Methacrylic acid (*MAA*) as an ionic comonomer increased the hydrophilicity, prevented a skin effect and allowed further chemical modification of the polymer [1,11,24,25]. 4-Methacryloylbenzophenone (*MABP*) served as the photocrosslinkable unit [20]. This terpolymer was photo-crosslinked and surface-attached by *UV* irradiation using a thiol- and

benzophenone-functionalized adhesion promoter [26]. The concept of benzophenone-based adhesion promoters was first introduced by Prucker et al., who utilized a chlorosilane functionality as a coating for silicon oxide surfaces [27]. Up to date, this concept was extended to triethoxysilanes (silicon oxide surfaces) [12], thioates (gold) [18] and phosphonic acids (aluminum and titanium) [28,29]. A second benzophenone strategy to graft hydrogels on a surface makes use of the fact that the polymer itself contains benzophenone units, which can attach to CH-containing surfaces [30]. This method was also successfully applied to the hydrogel system under investigation using a silanized surface [13].

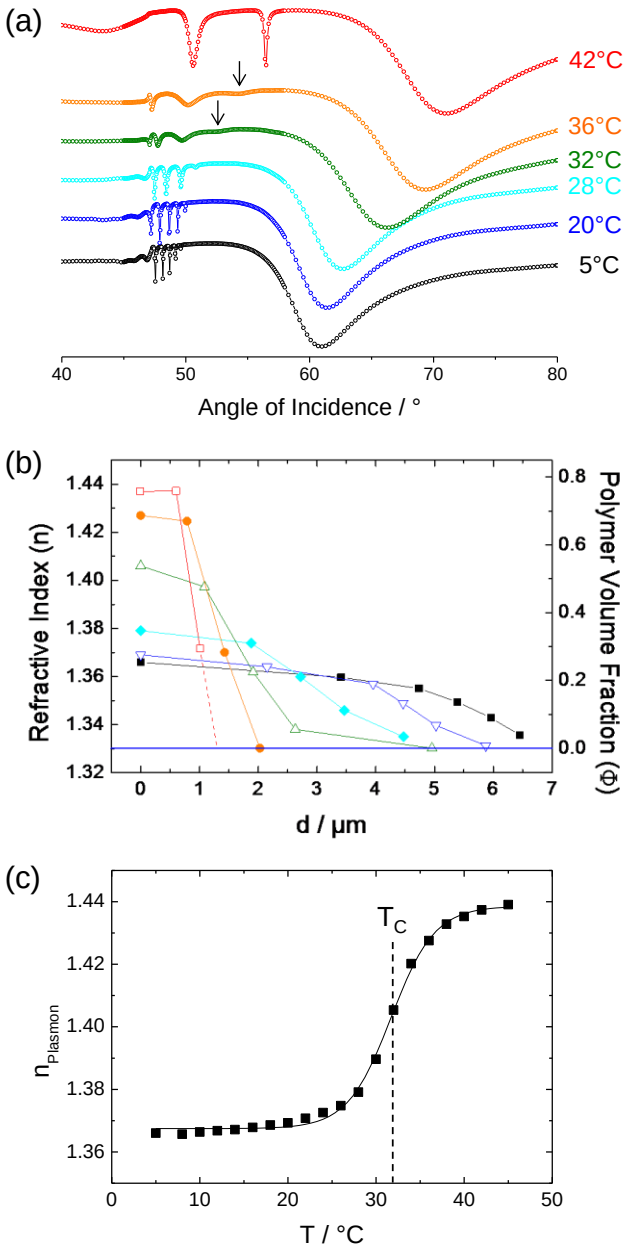

Figure 4.1: a) Experimental *SPR/OWS* data for selected temperatures. The black arrows mark the first waveguide mode TM_1 at temperatures near the volume transition temperature (T_C), which are substantially broadened due to inhomogeneities inside the hydrogel layer. b) Refractive index / polymer volume fraction profiles via Wentzel-Kramers-Brillouin and Bruggeman effective medium approximation at different temperatures: 5 °*C* (black squares), 20 ° C (blue triangles), 28 °*C* (cyan diamonds), 32 °*C* (green triangles), 36 °C (orange circles), 42 °*C* (red squares). The refractive index value at $d = 0\ \mu m$ was assigned from the angular minimum of the surface plasmon resonance. The refractive index of pure water is drawn as blue line. In c) refractive index probed by surface plasmon resonance is plotted versus temperature and fitted with a sigmoidal function [1].

4. 2 Results and Discussion

4.2.1 *SPR/OWS* Data

The experimental *SPR/OWS* data sets at selected temperatures are displayed in Fig. 4.1a. The angular scans were dominated by a broad reflectivity minimum of the surface plasmon resonance, which shifts from 60.9° (5 °*C*) to 71.0° (42 °*C*) with increasing temperature. Since the sample thickness is above 1 μm at all temperatures, optical waveguide modes were excited and additional sharp minima appeared at angles lower than the surface plasmon resonance and underwent considerable changes as a function of temperature.

At 5 °*C*, five very sharp waveguide modes (TM_1–TM_5 from right to left) were observed from 49.57° to 47.55°, furthermore two broad radiation modes. Up to a temperature of 20 °*C*, only minor changes occurred with the minima of these waveguide modes slightly spreading out from 49.95° to 47.20°. At 28 °*C*, the TM_5 mode was not observable any more, which was indicative of a decreased sample thickness. Increasing the temperature only by 4 *K* (up to 32 °*C*) to the *LCST* of the *NiPAAm* homopolymer, the waveguide modes were substantially broadened. While the TM_1 mode was most affected and hardly distinguishable, the last observable and usually broadest waveguide mode (TM_4) remained sharp. This broadening prevailed at 36 °*C* for the remaining three waveguide modes. Their angular minima extended still further from 54.1° to 47.3° (compared to 52.3° – 47.1° for four *TM* modes at 32 °*C*). At 42 °*C*, well above the *LCST* of the homopolymer, the first waveguide mode at 56.45° sharpened considerably to change from the least to the best defined feature of the *SPR/OWS* spectrum. Only one further waveguide mode (TM_2 at 50.60°) could couple into the thin collapsed hydrogel film. Upon cooling, the same temperature dependence was observed, indicating a completely reversible swelling and collapse process.

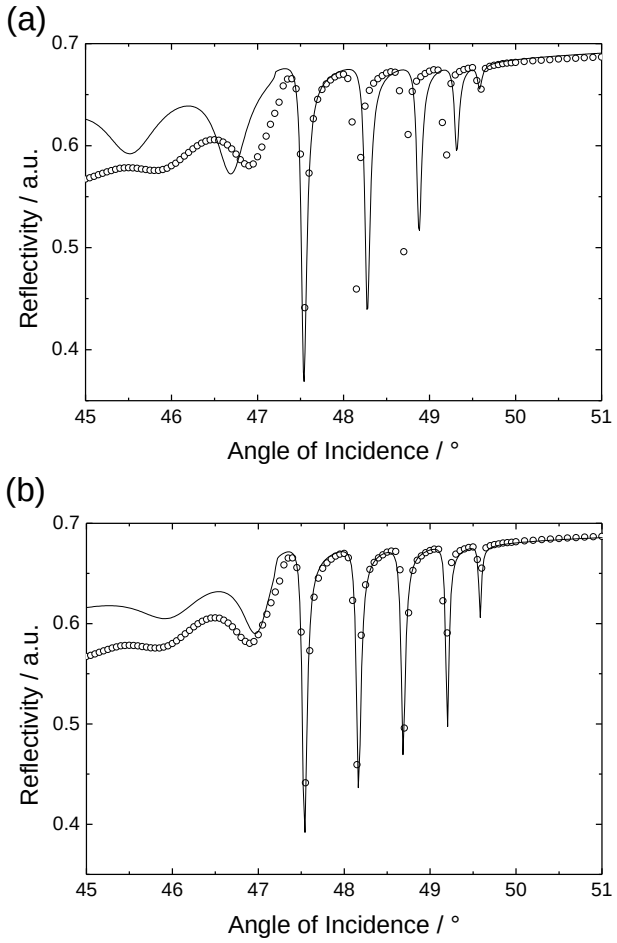

Figure 4.2: Waveguide modes of the *SPR/OW*S scan at 5 °*C*. (a) Best fit based on a box model simulation, (b) multiple slab simulation according to the refractive index profile obtained by reversed *WKB* approximation (cp. Fig. 4.3a) [1].

4.2.2 Data Evaluation.

The standard procedure to analyse the *SPR/OWS* data is to assume a homogeneous dielectric layer with a uniform refractive index. The refractive index was adjusted to fit the TM_1 mode, which is most sensitive to changes of this parameter while the thickness of the layer is adjusted to fit the highest mode number, here the TM_5 mode. The application of this so-called box model was not valid here as can be seen in Fig. 4.2a, since strong angular deviations were observed for the intermediate modes (TM_2–TM_4) and for the surface plasmon resonance (not shown). Thus, the hydrogel film could not be approximated as a single homogeneous layer with

invariant optical properties. The tethered hydrogel layer rather exhibited a refractive index gradient perpendicular to the gold–hydrogel interface, which could be obtained by the reversed Wentzel-Kramers-Brillouin (*rWKB*) approximation [18,21]. The refractive index at $d = 0$ *nm* is accessible by extrapolation of the *rWKB* data. Slopes of linear segments between neighbouring data points are squared and summed and the refractive index at $d = 0$ *nm* is extrapolated by minimization of this sum [34]. However, this extrapolation is only accurate for a smooth refractive index profile and if sufficient *rWKB* data points are available. In the collapsed state with three or less data points, this extrapolation is not meaningful. This problem can be overcome by analysis of the surface plasmon resonance. The evanescent field of the surface plasmon resonance is only sensitive to the refractive index in the first 200 *nm* of the hydrogel film close to the Au interface and its angular minimum can be used to retrieve information of the refractive index at the gold–hydrogel interface. This procedure enables the determination of the accurate refractive index gradient profiles, even for comparably thin films in the collapsed state.

4.2.3. Refractive Index and Polymer Volume Fraction Gradient Profiles.

Utilizing the effective medium approximation according to Bruggeman [35] and following Hirotsu et al. [36], the refractive indices of the gels can be converted into polymer volume fractions Φ according to eq. 4.1.

$$\Phi = \frac{n_{\mathrm{Hydrogel}} - n_{\mathrm{H_2O}}}{n_{\mathrm{Gel,dry}} - n_{\mathrm{H_2O}}} \qquad (4.1)$$

The refractive index n of the dry gel was 1.47 as determined by a separate *SPR/OWS* scan of the dry gel. The refractive index and polymer volume fraction gradient profiles are displayed in Figure 1b for various temperatures. At 5 °*C*, the refractive index of the gel is highest at the Au–hydrogel interface and drops with increasing slope towards the pure water value at a distance of 6.5 μm from the Au interface. The *rWKB* extrapolation to $d = 0$ μm yielded a refractive index of 1.364 ± 0.001, which was in perfect agreement with $n = 1.366 \pm 0.001$ from the surface plasmon analysis, indicating that five waveguide modes and the smooth refractive index profile in the

swollen state were sufficient for a good extrapolation. At 20 °*C*, the thickness of the gel was slightly decreased, while the maximum refractive index / polymer fraction was slightly increased. Although very small, these variations were discernible even at a temperature 12 *K* below the *LCST*. At 28 °*C*, closer to the transition temperature, these variations of the maximum refractive index and thickness were more pronounced. The transition regime from the bulk gel film to pure water (Δd > 2.5 μm) was significantly larger than for hydrogel layers well below the volume transition temperature (Δd ~ 1.5–2 μm). Here, the *rWKB* extrapolation of n = 1.387 ± 0.001 already yielded a considerable deviation from the value obtained by the surface plasmon resonance (n = 1.379 ± 0.001) and this procedure was not applicable any more. The refractive index profile at 32 °*C* showed the most significant changes. While the refractive index was drastically increased in the first µm, it decreased smoothly over a very broad thickness range (Δd > 4 μm) with the profile forming an S-shaped curve. This inhomogeneous refractive index profile showed characteristics of a swollen hydrogel at the boundary to the water phase, while a significantly higher refractive index at the Au interface was indicative of a highly collapsed state. It thus expressed the structural inhomogeneity of the hydrogel film at the phase transition temperature, where attractive and repulsive forces compete with each other. At 36 °*C* and 42 °*C*, above the volume transition temperature, the refractive indices at the Au–hydrogel interface and in the layer bulk were substantially increased while the sample thickness was strongly decreased, as water with its lower refractive index was driven out of the polymer network. A maximum polymer volume fraction of 0.8 was obtained, indicating that the collapsed gel still contained about 20% water. This observation was in agreement with previous reports [18]. The profiles exhibited a sharp interface to the water phase and the hydrogel layer could be approximated by a box model with a homogeneous refractive index profile (Δd ~ 0.5 μm). At 40 °*C* (data not shown) and at 42 °*C*, well in the collapsed regime, the refractive indices at the Au–hydrogel interface was slightly but reproducibly lower than in the layer bulk. At the Au interface, the attached hydrogel thus remained in a slightly more swollen state due to the lateral constraint imposed by the rigid substrate. This observation was in agreement with previous results from Harmon et al., who observed that a thin hydrogel layer near the surface is not able to fully collapse due to substrate confinement [17].

The shape of the refractive index profiles and their change with temperature matched well neutron scattering results on surfaces-attached *pNiPAAm* gels obtained by Vidyasagar et al. and

Yim et al. and those theoretically predicted by Mendez et al. [9,10,23]. They were also comparable to changes related to variations in crosslinking density as observed by Toomey et al. [20]. A dense network showed an almost rectangular volume fraction profile while the reduction of network restrictions resulted in a more pronounced gradient profile.

4.2.4 Volume Transition Temperature

A temperature-dependent collapse curve of the hydrogel could be obtained by plotting the refractive index obtained from the surface plasmon resonance vs. temperature (Fig. 4.1c) [16-18]. Due to the characteristic S-shape of the curve the data points could be fitted with a sigmoidal function:

$$n_{Pl} = n_{Pl,sw} + \frac{n_{Pl,coll} - n_{Pl,sw}}{1 + \exp(T - T_C)/\Delta T} \qquad (4.2)$$

The volume transition temperature of the hydrogel T_C, which is related to the *LCST* of a polymer solution, is defined as the inflection point of the curve. A value of 31.7 ± 0.1 *°C* was obtained, which is comparable to the T_C of the same hydrogel system with the same crosslinking treatment, surface-grafted to glass (d_{dry} = 450 *nm*) and investigated by atomic force spectroscopy (33 ± 1 *°C*) [13].

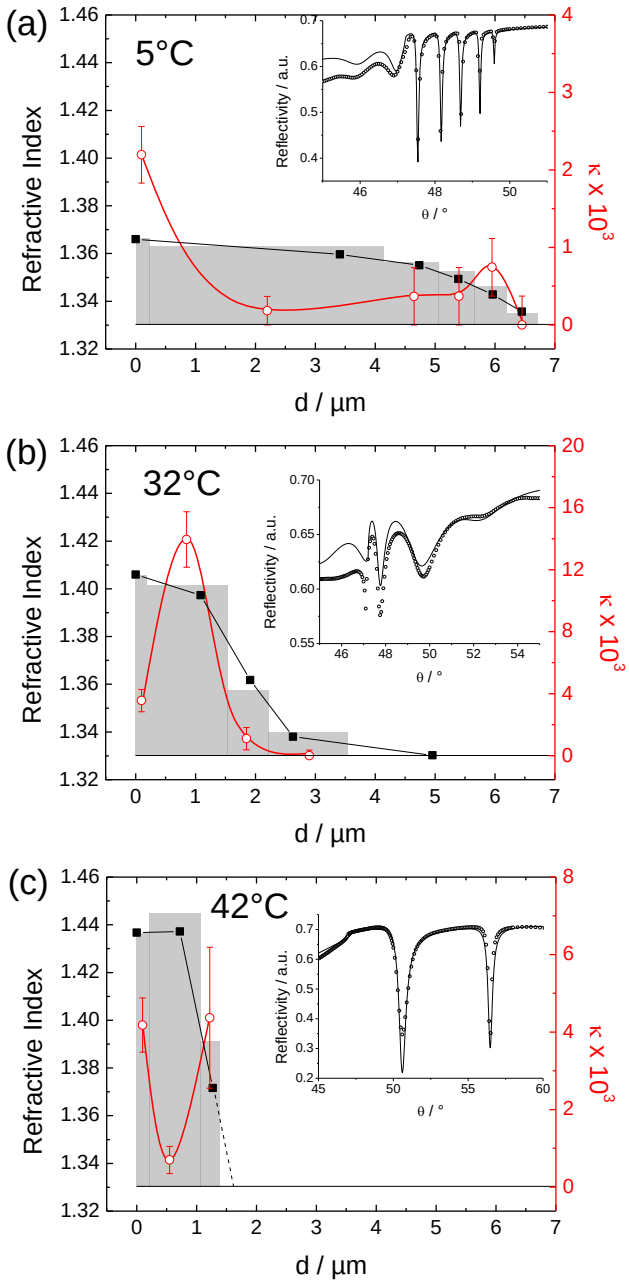

Figure 4.3: Refractive index profiles of the (a) swollen (5 °*C*), (b) collapsing (32 °*C*) and (c) fully collapsed (42 °*C*) hydrogel. The *SPR/OWS* data (inset) were simulated by dividing the hydrogel film in box-like sublayers with different, but homogeneous refractive indices (grey boxes). The values of the imaginary part κ (resembling optical losses) of these sublayers are displayed in red and are connected with a red line as guide to the eye [1].

4.2.5 Resimulation

The reversed *WKB* approximation provided detailed information of refractive index changes in the hydrogel layer perpendicular to the surface. To further exploit this information and to validate the *rWKB* approximation, the refractive index profiles obtained by *rWKB* were fitted with multiple sublayers, each with a uniform refractive index. The *SPR/OWS* data were then simulated with this multiple slab approach. For each waveguide mode *rWKB* data point one or less sublayer was fitted. In most cases, the border between two sublayers was set symmetrically between two adjacent *rWKB* data points. The refractive index of each sublayer was then adjusted to obtain the best angular simulation of the optical waveguide modes. For the first 200 *nm*, a separate sublayer was assigned with the refractive index obtained from the surface plasmon resonance. Thus, the angular simulation was improved considerably, as can be seen in Fig. 2 for the swollen hydrogel at 5 °*C*. While a single box model fit suffered from large deviations in the waveguide mode region, data and simulation agreed almost perfectly when the inhomogeneous refractive index profile of the hydrogel was simulated with six different sublayers. In Fig. 3a, these sublayers are displayed as grey slabs resembling the refractive index profile obtained by *rWKB* very well. Fig. 4.3 illustrates the multiple slab simulation technique for three characteristic states of the thermo-responsive hydrogel, the hydrogel in the swollen state at 5 °*C*, at the phase transition temperature (32 °*C*) and in the collapsed state (42 °*C*). The corresponding *SPR/OWS* data and simulations are shown as insets. At all temperatures, an excellent agreement of data and simulation was achieved with the assumed refractive index slabs resembling the *rWKB* profile. The largest deviations were observed at the phase transition temperature. This is caused by considerable deviations of the refractive index profile and the assumed uniform sublayers since the very inhomogeneous profile could barely be approximated by only four different slabs. At 42 °*C*, the trend in the *rWKB* data indicating a slightly lower refractive index at the Au–hydrogel interface than in the hydrogel bulk was manifested by the multiple slab simulation. To fit the *SPR/OWS* data accurately, even a higher refractive index difference had to be assumed, corroborating the theory already given by Harmon et al. that a thin gel layer near the surface is not able to collapse completely [17]. These authors used a two-sublayer simulation to analyse their results. The multiple sublayer approach based on *rWKB* introduced here represents a significant improvement since even very inhomogeneous refractive index profiles can be simulated accurately. Furthermore, a spatial vertical resolution of the structural inhomogeneity in

the hydrogel films could be assessed by interpretation of the optical losses. This will be explained in detail in the next paragraph.

4.2.6 Hydrogel Inhomogeneities

In the previous paragraphs, only the real part *n* of the complex refractive index was considered for the analysis of the refractive index profile. In this section, the imaginary part κ will be analysed as a measure for light intensity loss in the sample, which allows further conclusions about the local optical properties of the hydrogel film. The light intensity in a waveguide mode can be diminished via two different major phenomena. One possibility is the intrinsic absorption of the constituting material at 632.8 *nm*. This type of light intensity loss can be neglected for the hydrogel under investigation as it is highly transparent at this wavelength. The other type of loss is based on two scattering mechanisms. i) Surface scattering is related to the topography of the media, ii) volume scattering is effective if the waveguiding material contains optical inhomogeneities (refractive index fluctuations). Thus, κ is primarily a measure for the scattering losses in the hydrogel layer, which can be related to concentration gradients and ultimately to structural inhomogeneities of the sample.

In combination with the *rWKB* multiple layer resimulation approach, a vertical resolution of these inhomogeneities was accessible, which allowed some distinction between surface and volume scattering contribution in different swelling states of the film. κ was optimized for each sublayer of the hydrogel to obtain the best fit of width and depth of the surface plasmon resonance and the waveguide modes (full width at half maximum / *FWHM* analysis). The corresponding κ values are displayed in Fig.4.3 (red hollow circles) and are connected by a red line as guide to the eye. The κ value of (2-4) $\times$ 10^{-3} at the Au–hydrogel interface was relatively invariable for all temperatures and corresponding swelling states. It could be related to a "frozen" inhomogeneitiy due to the covalent surface attachment of the polymer network. Thus, the scattering losses were hardly affected by the swelling state of the hydrogel.

For the highly swollen hydrogel film at 5 °*C*, κ was very low in the centre of the dielectric layer ($\kappa < 8\times10^{-4}$) and slightly higher at the transition regime from layer bulk to water interface. At this temperature, water is a good solvent corresponding to a single phase in the *pNiPAAm*–water phase diagram for free *pNiPAAm* solutions and the polymer chains are homogeneously

hydrated. However, the non-zero κ values indicated slight inhomogeneities at the optical length scales even in the swollen state, which was in agreement with previous observations by Nuclear Magnetic Resonance (*NMR*) and Electron Paramagnetic Resonance (*EPR*) spectroscopy [31,37]. In the collapsed gel at 42 °*C*, the κ values in the layer centre and water interface were significantly increased, being very high at the gold and water interfaces ($\kappa \sim 4\times10^{-3}$) and lower in the layer centre ($\kappa = 1\times10^{-3}$). At this temperature, the gel is well in the phase separated region containing about 20 % water [18]. The high κ value at the hydrogel-water boundary could be explained by the significantly increased refractive index difference between the collapsed gel and water. Furthermore, topographic inhomgeneities at this interface, as observed by optical microscopy, would contribute as surface scattering losses and lead to higher κ values. The slightly increased κ-values in the layer centre (compared to the swollen state) were indicative of more static (nonergodic) inhomogeneities contributing to the light intensity losses. This was in good agreement with previous *EPR* spectroscopic results [31].

At the volume transition temperature (32 °*C*), the κ profile was significantly different from both the swollen and the collapsed state. At the hydrogel-water boundary, the κ values are comparable to those of the hydrogel in the swollen state. This indicates a single interfacial phase and a substantial amount of water were still incorporated in the polymeric network at this boundary. This was in line with the refractive index profile, which revealed a remaining water content >80 % in this interfacial region. The by far highest κ value ($\kappa = 1.4\times10^{-2}$) was, however, observed in the hydrogel layer centre, exceeding the value at the Au–hydrogel interface by four times. Qualitatively, this could already be deduced from the raw *OWS* angular data since the first waveguide mode is extremely broadened and hardly visible (Fig. 4.3b). The pronounced light intensity loss was caused by large inhomogeneities inside the hydrogel layer, which was also expressed by the complex slope of the refractive index profile. As known from light scattering, hydrogels undergo strong dynamic fluctuations at the volume transition temperature, i.e. the binodal phase line [38,39]. These dynamic fluctuations of the local polymer concentration / refractive index will manifest in volume scattering losses. Combined with the vertical information by *rWKB*, it could be deduced that the phase separation originates from the centre of the hydrogel layer, not from the interfaces to the water or the tethered substrate.

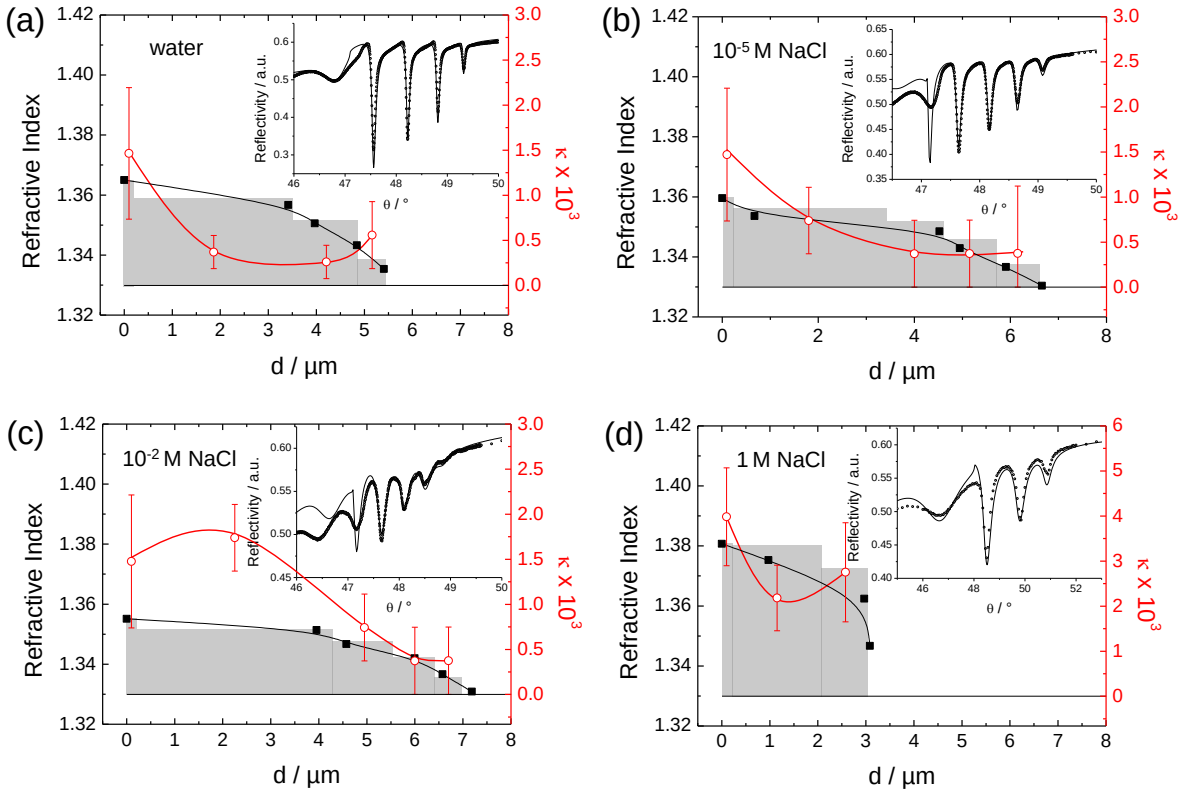

Figure 4.4: Refractive index profiles of the swollen hydrogel at 22 °*C* (a) in water, (b) in 10^{-5} *M NaCl*, (c) in 10^{-2} *M NaC*l and (d) in 1 *M* NaCl. The *SPR/OWS* data (inset) were simulated by slicing the hydrogel layer in sublayers with different refractive indices (grey slabs). The corresponding κ values of these sublayers are displayed in red and connected with a red line as guide to the eye [1].

4.2.6 Influence of Salt on the Swelling State

Besides the variation of temperature, a volume change in the hydrogel layer was also induced by addition of salt, as shown in Fig. 4.4 for *NaCl* concentrations of 10^{-5} *M*, 10^{-2} *M* and 1 *M* in water. Placed in pure water at 22 °*C* (Fig. 4.4a), the film centre was very homogeneous, while the interfaces to gold and water showed higher optical losses (compare also Fig. 4.3a at 5 °*C*). At a *NaCl* concentration of 10^{-5} *M* (Fig. 4.4b), the optical loss in the layer centre raised slightly leading to a more uniform distribution of inhomogeneities over the entire film. At the same time, the layer thickness increased from about 5.5 *µm* in pure water to 6.5 *µm* in 10^{-5} *M NaCl*. A further increase of the salt concentration to 10^{-2} *M* (Fig. 4.4c) lead to dramatic alteration of the distribution of inhomogeneities with highest optical losses in the layer centre and a further increase of the film thickness beyond 7 *µm*. The overall refractive index of the layer dropped

compared to the value in pure water and the hydrogel-water interface region was more extended ($\Delta d \sim 3\ \mu m$, from about 4 to 7 μm). While the decrease of homogeneity in the layer centre was very reminiscent of the situation for pure water around the transition temperature of 32 $°C$ (Fig. 4.3b), the thickness changed in the opposite direction (thinner for water and thicker for salt). At a high salt concentration of 1 *M* the situation reversed and the layer partly collapsed to a thickness of 3 μm, which was about twice the thickness of a thermally collapsed film at 42 $°C$ (Fig. 4.3c). The homogeneity was again higher in the layer centre compared to the gold and water interfaces. Here, the optical loss at the hydrogel-water interface clearly increased compared to the values at lower salt concentration, which suggested an increased layer surface roughness.

Potential mechanisms of the salt effect on the swelling behaviour might be an increased osmotic pressure in the polymer due to the salt ions and a variation of the solvent quality of the salt solution for the polymer. In particular, at low salt concentrations, the exchange of protons from the carboxylic acid by Cl^- counterions and the diffusion of Na^+ and Cl^- ions into the hydrogel network could lead to an increased osmotic pressure and a correspondingly higher swelling state with layer expansion. At a very high salt concentration (1 *M NaCl*), charge screening of the repelling negatively charged carboxylate groups by the salt ions and a substantial drop in solvent quality of the salt solution for the polymer may lead to the observed partial collapse of the hydrogel film (salting out). Similar effects of salt on the layer thickness have been reported in the literature for polymethacrylic acid brushes [40].

4.3 Conclusions

The presented results document that *SPR/OWS* spectroscopy combined with the reversed *WKB* approximation is a powerful method to gain detailed information about gradients and inhomogeneities in thin surface-attached thermo-responsive hydrogel films. By *SPR/OWS* spectroscopy the reflectivity minima of waveguide modes and surface plasmons are measured in angular reflectivity scans. From the angular position of these minima the refractive index profile perpendicular to the film surface was calculated by the reversed *WKB* approximation. Such a refractive index profile formed the basis of a multilayer model, in which for each individual slab perpendicular to the multilayer surface the local refractive index *n* and the corresponding

imaginary part κ was calculated. This imaginary part κ is a measure for optical losses, which were interpreted in our system as hydrogel inhomogeneities.

By this treatment we could identify different levels of inhomogeneities for the individual layer slabs that vary characteristically with temperature and salt concentration. In particular the inhomogeneities in the layer centre increased significantly for temperatures and salt concentrations around the layer transition from the swollen to the collapsed state. On the other hand, both the fully swollen and the collapsed layers were more homogeneous in the centre of the hydrogel film than at the interfaces to gold and water.

By this analysis we could deduce that the hydrogel collapse originates from the layer centre rather than from its interfaces, which is equally valid for the collapse induced by increased temperatures as well as by high salt concentration.

A conspicuous difference between increasing temperature and salt concentration was observed for the change in layer thickness, which expands with increasing salt concentration (below the collapse concentration), while for increasing temperatures even below the collapse the layer thickness decreased.

4.4 Experimental Part

Materials. The adhesion promoter 3-(4-Benzoylphenoxy)propanethiol (*BPSH*) was synthesized as described in the literature [26]. A 4/1 mixture with the corresponding disulfide was obtained and further used. The disulfide was not removed from the *BPSH* mixture since both thiols and disulfides are capable of monolayer formation on gold surfaces. Distilled water was purified by a MilliQ System (Millipore) to achieve a resistivity of 18.2 $M\Omega\,cm$ (ultrapure water).

Polymer. A statistical terpolymer based on N-isopropylacrylamide (*NiPAAm*, 94 % monomer concentration) with methacrylic acid (*MAA*, 5 % m.c.) and 4-methacryloylbenzophenone (MABP, 1 % m.c.) was obtained by free radical polymerization, initiated by azobisisobutyronitrile (*AIBN*) in dioxane. The molecular weight (M_W) of 206 kg mol^{-1} and the polydispersity index (M_W/M_N) of 2.0 were determined by gel permeation chromatography with dimethylformamide as mobile phase. The measurement was conducted at 60°C, *PMMA* served as internal

standard. The polymer composition resembles the monomer composition in the reaction feed as revealed by ^{1}H *NMR*. Details concerning synthesis and characterization are described in a previous publication [31]. The structure of the terpolymer is shown in Fig.4.5.

Sample Preparation. Chromium (1.0 *nm*) and gold (47.7 *nm*) were evaporated on *LaSFN9* glasses (Hellma Optik GmbH, Jena) in an Edwards Auto 306 evaporator. The exact thicknesses of *Au* and *Cr* were determined by *SPR* reference measurements. A 1.2 *mM* solution of *BPSH* in ethanol was immobilized onto the gold surface overnight, rinsed with ethanol, dried with N_2 gas, and stored in the dark under argon until use. The distance between two benzophenone units of the thiol monolayer is estimated from the molecular dimensions as approx. 0.5-1 *nm*. However, the yield of the *UV*-induced grafting of the polymer onto the surface and thus the grafting density is unknown.

A 10 wt% terpolymer solution in ethanol was filtered with a *PVDF* syringe filter (0.45 *µm*, Roth) to remove non-dissolved components and spin coated on the modified glass substrate (60 s, 4000 *rpm*). The samples were dried overnight in vacuum at 40 °C. The thickness of the dry film of approx. 1050 *nm* was measured with a Tencor P-10 Surface Profiler (KLA Tencor). Both crosslinking and surface attachment were carried out in a single process step by irradiating the sample with *UV* light (λ = 365 *nm*) for 30 *min* (Stratalinker 2400, Stratagene; cp. Fig.4.5) [20,32]. A total light energy of 3.14 $J\ cm^{-2}$ was dissipated.

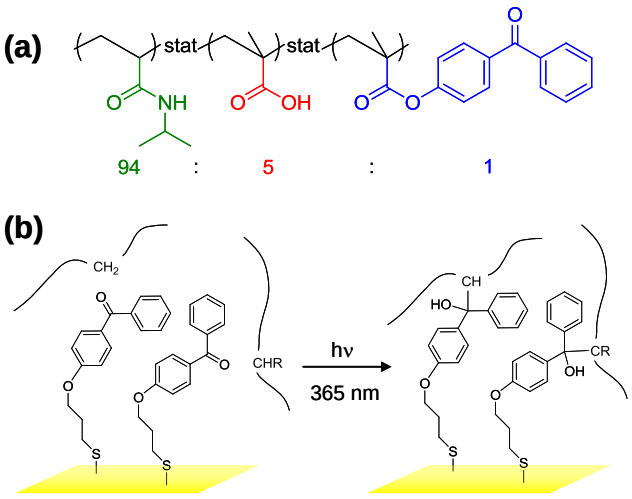

Figure 4.5: (a) Structure and composition of the investigated polymer, (b) *UV*-light induced surface attachment analogous to network formation [1].

***SPR/OWS* Measurements.** *SPR/OWS* spectra were recorded in the Kretschmann configuration with a customized setup described in 3.1. The sample was placed in a heatable and coolable flow cell (temperature accuracy: 0.1 *K*), which was then filled with ultrapure water. The angular dependence of the reflectivity was modelled by Fresnel's equations and transfer matrix algorithm for a multilayer system, consisting of the *LaSFN9* glass and layers of *Cr, Au, BPSH*, gel, and water. Thus, the *SPR/OWS* scans yield information about the complex refractive indices $n + i\kappa$ of these layers. The relation of the complex refractive index to the dielectric function ε is given by eq:

$$\varepsilon = \varepsilon' + i\varepsilon'' = (n + i\kappa)^2 \qquad (4.2)$$

The real part of the complex refractive index, *n* is determined by the angular minima of the resonances of the surface plasmon and the optical waveguide modes. The imaginary part κ can be inferred from the width and depth, i.e. coupling efficiency of the peaks and is a measure for the light intensity loss in the system. Thus, it allows further conclusions about the optical properties of the. In this study, both parts of the refractive index were evaluated. The real part of the refractive index *n*, referred to as refractive index, is dealt with in the first part of the "Results and Discussion" section. In the second part, "Hydrogel Inhomogeneities", the imaginary part κ is analysed.

By increasing the temperature to 50 °*C*, the swollen hydrogel was collapsed and non-crosslinked polymer fragments were removed from the network. By this pre-treatment, a completely reversible collapse behaviour is achieved [18,26]. The solvent was exchanged to fresh solvent and the temperature was adjusted to 5 °*C*. To ensure the optical and thermal stability of the system, the first angular $I(\theta)$ scan was recorded after a 30 *min* time period. After each $I(\theta)$ scan, the temperature was increased in steps of 2 *K* or 3 *K* to a maximum temperature of 42 °*C*. Following each temperature increase, the gel was equilibrated for 15 min to reach a constant temperature. Upon achieving the maximum temperature, the temperature was decreased in steps and further $I(\theta)$ scans were recorded to study the reversibility of the collapse.

References

[1] Junk, M. J. N., Anac, I., Menges, B. and Jonas, U., Langmuir, **2010**, 26, 14,12253-12259.

[2] Schild, H. G., *Prog. Polym. Sci.* **1992**, *17*, 163–249.

[3] Percot, A.; Zhu, X. X.; Lafleur, M., *J. Polym. Sci., Part B: Polym. Phys.* **2000**, *38*, 907–915.

[4] Qiu, Y.; Park, K., *Adv. Drug Del. Rev.* **2001**, *53*, 321–339.

[5] Hoffman, A. S., *Adv. Drug Del. Rev.* **2002**, *54*, 3–12.

[6] Peppas, N. A.; Hilt, J. Z.; Khademhosseini, A.; Langer, R., *Adv. Mater.* **2006**, *18*, 1345–1360.

[7] Richter, A.; Kuckling, D.; Howitz, S.; Gehring, T.; Arndt, K. F., *J. Microelectromech. S.* **2003**, *12*, 748–753.

[8] Annaka, M.; Motokawa, K.; Sasaki, S.; Nakahira, T.; Kawasaki, H.; Maeda, H.; Amo, Y.; Tominaga, Y., *J. Chem. Phys.* **2000**, *113*, 5980–5985.

[9] Vidyasagar, A.; Majewski, J.; Toomey, R., *Macromolecules* **2008**, *41*, 919–924.

[10] Yim, H.; Kent, M. S.; Mendez, S.; Balamurugan, S. S.; Balamurugan, S.; Lopez, G. P.; Satija, S., *Macromolecules* **2004**, *37*, 1994–1997.

[11] Gianneli, M.; Beines, P. W.; Roskamp, R. F.; Koynov, K.; Fytas, G.; Knoll, W., *J. Phys. Chem. C* **2007**, *111*, 13205–13211.

[12] Gianneli, M.; Roskamp, R. F.; Jonas, U.; Loppinet, B.; Fytas, G.; Knoll, W., *Soft Matter* **2008**, *4*, 1443–1447.

[13] Junk, M. J. N.; Berger, R.; Jonas, U., *Langmuir* **2010**, DOI: 10.1021/la903396v.

[14] Balamurugan, S.; Mendez, S.; Balamurugan, S. S.; O'Brien, M. J.; Lopez, G. P., *Langmuir* **2003**, *19*, 2545–2549.

[15] Harmon, M. E.; Jakob, T. A. M.; Knoll, W.; Frank, C. W., *Macromolecules* **2002**, *35*, 5999–6004.

[16] Kuckling, D.; Harmon, M. E.; Frank, C. W., *Macromolecules* **2002**, *35*, 6377–6383.

[17] Harmon, M. E.; Kuckling, D.; Frank, C. W., *Macromolecules* **2003**, *36*, 162–172.

[18] Beines, P. W.; Klosterkamp, I.; Menges, B.; Jonas, U.; Knoll, W., *Langmuir* **2007**, *23*, 2231–2238.

[19] Knoll, W., *Annu. Rev. Phys. Chem.* **1998**, *49*, 569–638.

[20] Toomey, R.; Freidank, D.; Rühe, J., *Macromolecules* **2004**, *37*, 882–887.

[21] Weisser, M.; Thoma, F.; Menges, B.; Langbein, U.; Mittler-Neher, S., *Opt. Commun.* **1998**, *153*, 27–31.

[22] Habicht, J.; Schmidt, M.; Rühe, J.; Johannsmann, D., *Langmuir* **1999,** 15, 2460–2465.

[23] Mendez, S.; Curro, J. G.; McCoy, J. D.; Lopez, G. P., *Macromolecules* **2005**, *38*, 174–181.

[24] Xue, W.; Hamley, I. W.; Huglin, M. B., *Polymer* **2002**, *43*, 5181–5186.

[25] Yu, H.; Grainger, D. W., *J. Appl. Polym. Sci.* **1993**, *49*, 1553–1563.

[26] Anac, I.; Aulasevich, A.; Junk, M. J. N.; Jakubowicz, P.; Roskamp, R. F.; Menges, B.; Jonas, U.; Knoll, W., *Macromol. Chem. Phys.* **2010**, DOI: 10.1002/macp.200900533.
[27] Prucker, O.; Naumann, C. A.; Rühe, J.; Knoll, W.; Frank, C. W., *J. Am. Chem. Soc.* **1999,** 121, 8766–8770.
[28] Pahnke, J.; Rühe, J., *Macromol. Rapid Commun.* **2004,** 25, 1396–1401.
[29] Griep-Raming, N.; Karger, M.; Menzel, H., *Langmuir* **2004,** 20, 11811–11814.
[30] Amos, R. A.; Anderson, A. B.; Clapper, D. L.; Duquette, P. H.; Duran, L. W.; Hohle, S. G.; Sogard, D. J.; Swanson, M. J.; Guire, P. E., Biomaterial Surface Modification Using Photochemical Coupling Technology; In *Encyclopedic Handbook of Biomaterials and Bioengineering, Part A: Materials*, Wise, D. L.; Trantolo, D. J.; Altobelli, D. E.; Yaszemski, M. J.; Gresser, J. D.; Schwartz, E. R., Eds.; Marcel Dekker: New York, 1995; Vol. 1.
[31] Junk, M. J. N.; Jonas, U.; Hinderberger, D., *Small* **2008**, *4*, 1485–1493.
[32] Turro, N. J., *Modern Molecular Photochemistry*; University Science Books: Mill Valley, California 1991.
[33] van den Brom, C. R.; Anac, I.; Roskamp, R. F.; Retsch, M.; Jonas, U.; Menges, B.; Preece, J. A., *J. Mater. Chem.* **2010,** DOI: 10.1039/b927314j.
[34] Karte, W.; Müller, R., *Integrierte Optik*; Akademische Verlagsgesellschaft Geest und Porttig KG: Leipzig, 1991.
[35] a) Bruggeman, D. A. G., *Ann. Phys.* **1935**, *24*, 636–664; b) Bruggeman, D. A. G., *Ann. Phys.* **1935**, *24*, 665–679.
[36] Hirotsu, S.; Yamamoto, I.; Matsuo, A.; Okajima, T.; Furukawa, H.; Yamamoto, T., *J. Phys. Soc. Jpn.* **1995**, *64*, 2898–2907.
[37] Saalwächter, K., *Prog. Nucl. Magn. Reson. Spectrosc.* **2007**, *51*, 1–35.
[38] Shibayama, M.; Takata, S.; Norisuye, T., *Physica A* **1998**, *249*, 245–252.
[39] Ikkai, F.; Shibayama, M., *J. Polym. Sci., Part B: Polym. Phys.* **2005**, *43*, 617–628.
[40] Biesalski, M.; Johannsmann, D.; Rühe, J., *J. Chem. Phys.* **2002**, *117*, 4988–4994.

5 Nanoparticle Composites

A new photo-cross-linked thermo-responsive nanocomposite hydrogel stabilised by "super-crosslinking" nanoparticles was studied by surface plasmon resonance and optical waveguide spectroscopy (*SPR/OWS*). The mechanically robust composite showed excellent responsive properties for potential incorporation into sensors and actuators. This project was a cooperation with Coenraad R. van den Brom who performed the measurements, Ilke Anac, Robert F. Roskamp, Markus Retsch, Ulrich Jonas, and Jon A. Preece. It has already been published [1].

5.1 Introduction

Hydrogel nanocomposites [2] exploit the embedding of nanoparticles (*NPs*) into a hydrogel polymer matrix to modify its properties. Such nanocomposites are much studied, predominantly for the purpose of structural reinforcement [3].

Nanocomposites of hydrogels with *Au-NPs* allow solvent-switchable electronic properties [4] and optical *pH*-sensing [5]. Responsive hydrogels have also been combined with polystyrene colloidal crystals [6] and have been used in sensors for metal ions [7].

Poly-(*N*-isopropylacrylamide) (*pNIPAAm*) [8] is one of the most intensively studied hydrogel materials. Heating aqueous *pNIPAAm* to a temperature above approx. 32 °C leads to a collapse from an extended coil to a globular structure, and hence to a sudden decrease in the degree of swelling. Such swelling behaviour of *pNIPAAm* gels depends on the crosslinking density [9] and the number of ionic groups along the backbone [10]. The swelling of bulk isotropic *pNIPAAm* gels is uniform in all directions [11]. In contrast, the swelling of surface-attached *pNIPAAm* thin films is highly anisotropic as the volume change is confined to one dimension perpendicular to the substrate [11,12]. Surface-attachment has a strong impact on the swelling [6] and the temperature dependent properties of the networks [9,13,14].

Various *pNIPAAm*-based nanocomposites have been reported in the literature, e.g. with exfoliated clays [15], carbon nanotubes [16] and a diversity of *NPs* [2]. *Au-NPs*, for instance, were either grown in-situ [17], or trapped in a bulk gel [8]. Core-shell *NPs* were

integrated in *pNIPAAm* to yield a photothermally responsive nanocomposite [19]. Arrays of rigid silicon columns could be manipulated by embedding them in *pNIPAAm* [20].

Silica *NPs* have also been combined with *pNIPAAm*, e.g. for the formation of a *pH*-sensing inverse opal [21]. Layer-by-layer growth of *pNIPAAm* with amine-terminated silica *NPs* was used for the construction of surfaces with tunable wettability [22]. Silica particles embedded in *pNIPAAm* with a packing gradient were applied construct temperature responsive bending materials [23].

This chapter is structured as follows:

Section 5.2.1 describes the *SPR/OWS* investigations on *pNIPAAm* thin films and focuses on the two essential parameters for responsive hydrogel composites, i. e. their swelling ratio and the occurrence of the thermally induced collapse. First, angular scans for pure *pNIPAAm* and for composites of varying composition/crosslink density are presented. These data allow the determination of the swelling ratios and the assessment of the homogeneity of the swollen films. Measurement and comparison of the thermal response yields critical temperatures and allows remarkable observations regarding hysteresis in the thermal response (section 5.2.4) and the high durability of the films (section 5.2.5). The preparation of the composite films (Figure 5.6) is discussed in Section 5.4.

5.2 Results and Discussion

5.2.1 Swelling Studies by *SPR/OWS*

The thermoresponsive behaviour of *pNIPAAm/BPTES*-coated (4-benzoylphenoxy-propyl-(triethoxy)silane) *NPs* nanocomposite films was assessed with *SPR/OWS* in Kretschman configuration (see Chapter 3.1). In this technique, the incident angles at which surface plasmon resonance occurs or light is coupled into waveguide modes depend on layer thicknesses and refractive indicies. These parameters were used to establish swelling ratios (*SR*) based on thickness and water content, respectively. Moreover, the layer homogeneity of the different films was investigated. Critical temperatures were found by following the temperature-dependent shifts in the *SPR/OWS* spectra. The film properties will be discussed in terms of *NP*-content and photocrosslinking energy dose (*PED*).

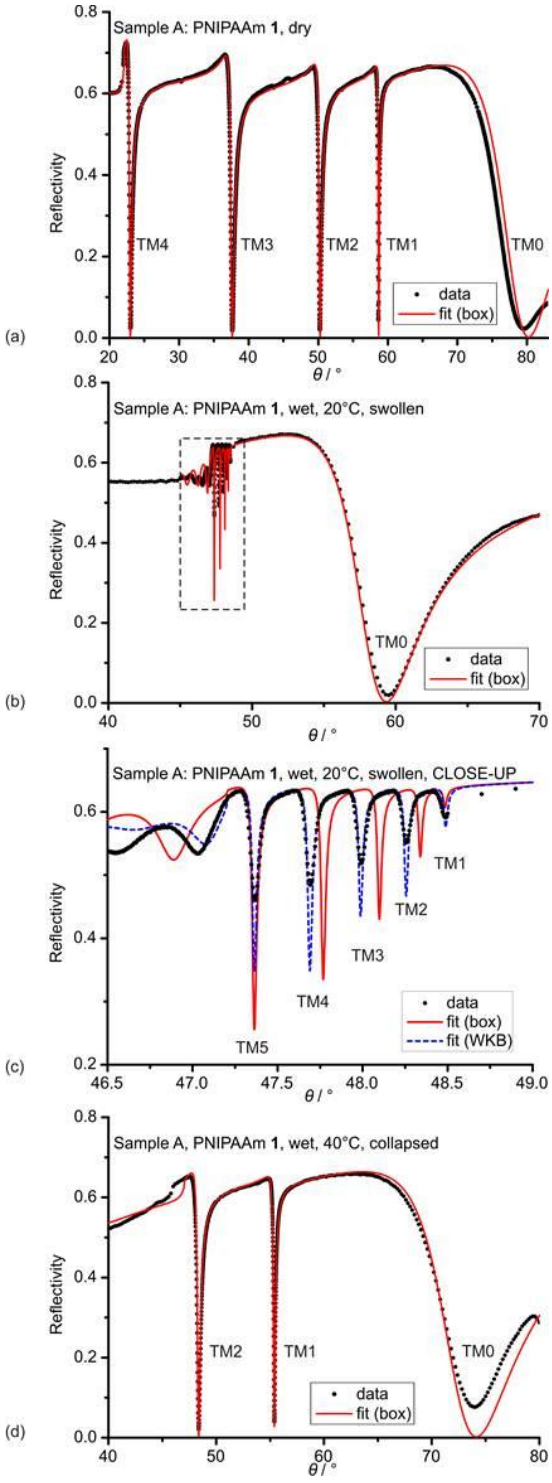

Figure 5.1: *SPR/OWS* spectra for a film of pure *pNIPAAm* terpolymer on a *LaSFN9* glass slide with a gold layer coated with adhesion promoter (*PED* 6.28 $J \cdot cm^{-2}$). (a) Dry film. (b) The film swollen in water at 20 °*C*. (c) A close up of (b) in the region of the minima corresponding to the guided optical waves TM_1 to TM_5. (d) The collapsed film in water at 40 °*C*. All spectra were recorded with *TM*-polarised light. The dots are measured data points, the lines correspond to simulated spectra: solid lines for a box model and the dashed curve in (c) for a density gradient based on *rWKB*-results [1].

A Pure *pNIPAAm* Film

In Fig.5.1 shows a series of *SPR/OWS* spectra (angular scans of $I(\theta)$) recorded with *TM*-polarised light of a dry film of *pNIPAAm* terpolymer (sample A). These spectra showed the typical features observed in the spectra of all samples: (1) The broad minimum around 79.5° corresponds to the excitation of a surface plasmon at the gold/polymer interface. (2) The four sharp minima left to it correspond to coupling of light into guided optical modes that are confined inside the polymer film and are labeled TM_1-TM_4.

The excellent optical quality in terms of smoothness and homogeneity of the film is evident in Fig.5.1a from (1) the narrow width of the peaks TM_1–TM_4, (2) the high coupling efficiency (depth of peaks) and (3) the good fit obtained with a box model, yielding $d_{composite}$ = 1.128 ± 0.005 μm and $n_{composite}$ = 1.493 ± 0.003.

Table 5.1 Composite film properties (thickness *d*, complex refractive index, *n* and κ) based on box-model simulations of the optical waveguide mode spectrum [1]

	Composite details		**Waveguide mode analysis**						**Swelling Ratio**
			Swollen composite at 20°C			**Collapsed composite at 40°C**			
	%-wt *NPs*	*PED* (J·cm^{-2})	$d_{composite}$ (μm)	$n_{composite}$	$\kappa_{composite}$	$d_{composite}$ (μm)	$n_{composite}$	$\kappa_{composite}$	SR_{1D}
A	0	6.28	7.70	1.348	0.0001	1.05	1.457	0.0003	7.34
B	20	6.28	6.34	1.363	0.0004	1.38	1.467	0	4.61
C	34	6.28	5.53	1.378	0.0004	1.77	1.466	0.0003	3.12
D	51	6.28	4.31	1.410	0.0005	2.48	1.464	0.0004	1.74
E	34	3.14	7.78	1.368	0.0004	1.94	1.466	0.0001	4.01
F	34	1.57	10.16	1.359	0.0004	2.06	1.462	0.0003	4.93

Due to swelling of the film in water at 20 °C, the waveguide modes are much closer spaced in the spectrum in Figure 5.1b. The coupling is less efficient because of the much smaller contrast in refractive indices between the swollen film and the water phase. The close-up of the region with TM_1-TM_5 in Figure 5.1c shows that behaviour for this sample and

in addition the simulation according to a box-model simulation (i.e. representing the composite layer as a single "box" with one thickness and one uniform refractive index) and a *rWKB* approach. It is clear from Fig. 5.1c that the box model is not an accurate description (see detailed discussion below).

When the temperature was increased to 40 °*C*, which was located above the critical temperature (T_c) for such *pNIPAAm* networks [9], the film collapsed, as evidenced by the spectrum in Fig.5.1d: TM_0, TM_1 and TM_2 have shifted to larger angles and increased in intensity, while TM_3 and TM_4 disappeared. The simulated spectrum of the collapsed film yielded a thickness of 1.05 ± 0.01 μm and a refractive index n = 1.457 ± 0.002, both close to the values for the dry film.

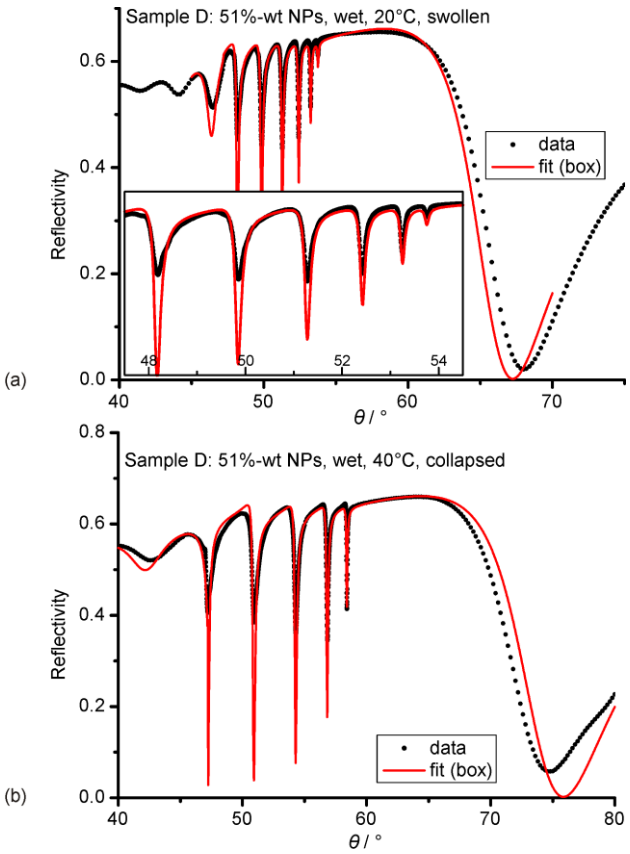

Figure 5.2: *SPR/OWS* spectra for a composite film of *pNIPAAm* and nanoparticle (51%-wt) on a *LaSFN9* glass slide with a gold film coated with adhesion promoter, (*PED*: 6.28 $J{\cdot}cm^{-2}$). (a) The film swollen in water at 20 °*C*; the inset shows the region of the waveguide modes TM_1 to TM_6. (b) The collapsed film in water at 40 °*C*. The dots are measured data points, the lines correspond to simulated spectra for a box model [1].

Variation of the Nanoparticle Content and Crosslink Density

Angular scans were also recorded for 5 samples (B–F) at 20 °*C* and 40 °*C* to investigate the effect of increasing nanoparticle content (samples A, B, C, D) and photocrosslink density (samples C, E, F). Figure 5.2 shows the spectrum of sample D with an *NP* content of 51%-wt (*PED*: 6.28 $J{\cdot}cm^{-2}$) swollen in water at 20 °*C*. The box-model simulation fitted this spectrum very well, which indicates that the composite film in this case was much more uniform than without particles. Samples B, C, E, and F show intermediate behaviour (raw data are not shown). The results of all the box-model simulations are summarized in Table 5.1 in terms of the film thickness $d_{composite}$ and the real and imaginary parts of the refravtive index n and κ. The imaginary part κ is associated with peak broadening and attributed to scattering and absorption processes. The low values highlight the high optical quality of the films.

Comparing 1D Swelling Ratios (SR_{1D})

The thicknesses reported in Table 5.1 were used to calculate the one dimensional swelling ratio:

$$\mathrm{SR}_{1\mathrm{D}} = d_{\mathrm{swollen}} / d_{\mathrm{collapsed}} \qquad (5.1)$$

Although the composite/water boundary in case of *pNIPAAm1* without *NPs* (sample A) was diffuse (see in the following sections), the box-model thickness provided the simplest approximation and eased comparison between different systems, including those already present in literature, like e.g. SR_{1D} = 7.3 for pure *pNIPAAm1* with a *PED* of 6.28 $J{\cdot}cm^{-2}$ [9].

Figure 5.3 shows that there was a clear relationship between the swelling ratios SR_{1D} of composite films with varying the nanoparticle content (A-D) and the degree of cross-linking (C,E,F), respectively. On increasing the *NP*-content (at a constant *PED* of 6.28 $J{\cdot}cm^{-2}$), SR_{1D} decreases almost linearly from 7.33 ± 0.08 to 1.74 ± 0.03. This decrease may be explained by the nanoparticles serving as “supercrosslinking” nodes that made the structure much more rigid: Close to the nanoparticle surfaces the swelling was strongly constrained

due to the high local concentration of the benzophenone "adhesion promoter" Conversely, the *SR* increased on reducing the irradiation dose and hence the crosslink density. The observed trends in *SR* strongly suggested that the nanoparticles were indeed firmly bound to the surrounding polymer matrix.

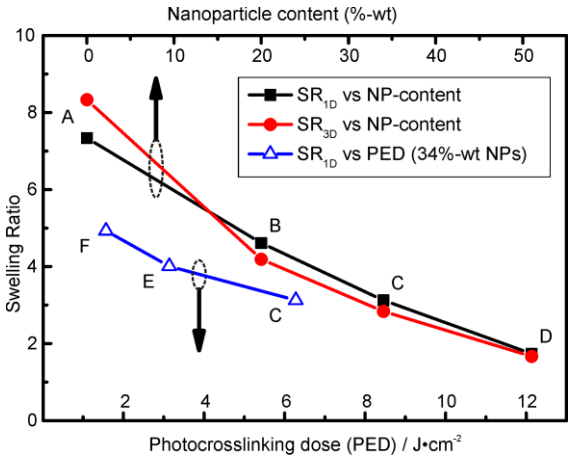

Figure 5.3: Swelling ratios SR_{1D} and SR_{3D} of polymer (1)/nanoparticle (4) composite films, as a function of the weight fraction of *NPs* with constant photo-crosslinking energy dose (6.28 $J{\cdot}cm^{-2}$; samples A–D, top scale) and as a function of *PED* (UV irradiation) with constant *NP*-content (34%-wt; samples C, E, F; bottom scale) [1].

SR_{3D} from Water Content

Besides the determination of the 1D swelling ratio from the film thickness change, an independent method used the change in water content, which allowed comparison of both types of swelling ratios. The refractive indices in Table 5.1 were used to calculate the water contents of the swollen and collapsed composite films. These water contents allowed the calculation of a three dimensional swelling ratio SR_{3D} solely based on the increase in water volume, assuming that the volume occupied by the *pNIPAAm1* polymer chains and the *NPs*4 is unaltered during the volume phase transition:

$$\mathrm{SR}_{3\mathrm{D}} = \frac{V_{\mathrm{tot}}^{\mathrm{swollen}}}{V_{\mathrm{tot}}^{\mathrm{collapsed}}} = \frac{1 - f_{\mathrm{vol}}^{\mathrm{collapsed}}(\mathrm{H_2O})}{1 - f_{\mathrm{vol}}^{\mathrm{swollen}}(\mathrm{H_2O})} \qquad (5.2)$$

Here, V_{tot} is the total volume of *pNIPAAm*, *NPs*, and water, and $f_{vol}(H_2O)$ is the volume fraction of water. Whereas SR_{1D} was based on the thickness obtained by the box-model fitting, SR_{3D} was derived from the measured refractive index *n*.

Using the effective medium approximation [28], we first calculated the *n* of the *NPs*, from the refractive indicies of pure *pNIPAAm* and the dry composite films. The average value obtained for *n* of the *NPs* is 1.4607, very well in agreement with the literature for amorphous SiO_2 (1.46008) [29]. The water content of the swollen and collapsed films are summarized in Table 5.2. Please note, how collapsed films still contained up to 15 % water. The associated volume-based SR_{3D} values compared very well with the thickness-based SR_{1D} values (Table 5.2 and Figure 5.6). Based on the sample geometry, this meant that the swelling was indeed pseudo-one-dimensional.

Table 5.2 Water uptake by composite gels calculated from *n* by the effective medium approximation: Volume fraction water ($f_{vol}(H_2O)$), loading ratios (LR_{3D}) and the swelling ratio (SR_{3D}) as a function of the weight fraction *NPs 2* ($f_{wt}(NP)$) [1].

Sample	**Dry solid**	**Collapsed (40°C)**		**Swollen (20°C)**		
	f_{wt}(NP)	f_{vol}(**H_2O**)	LR_{3D}	f_{vol}(**H_2O**)	LR_{3D}	SR_{3D}
A	0.00	0.16	0.19	0.90	8.90	8.33
B	0.20	0.14	0.19	0.79	4.67	4.19
C	0.34	0.10	0.16	0.68	3.06	2.84
D	0.51	0.06	0.12	0.44	1.45	1.67

Within the composite, only the polymer could take up water. The decrease in the *SRs* for the samples A–D might therefore be caused by the increasing *NP* content reducing the swellable fraction of the composite. This idea could be ruled out by comparing the loading ratios LR_{3D} for samples A-D. LR_{3D} (Table 5.2) expressed the water uptake per unit polymer volume, defined as $LR_{3D} = f_{vol}(H_2O)/f_{vol}$(polymer). The decrease in *LR* directly corresponded to an increase in the polymer volume fraction and showed that for samples with the same *PED* (essentially the same inter-chain photo-crosslinking) the *pNIPAAm* absorbs less water on increasing particle content. This decrease was explained by the increasing crosslinking of the polymer chains to the particles

that made it locally impossible for the gel to swell further. This analysis thus supported the theory that the *NPs* act as supercrosslinkers. Further discussion on the effect of supercrosslinking on the transition temperature follows.

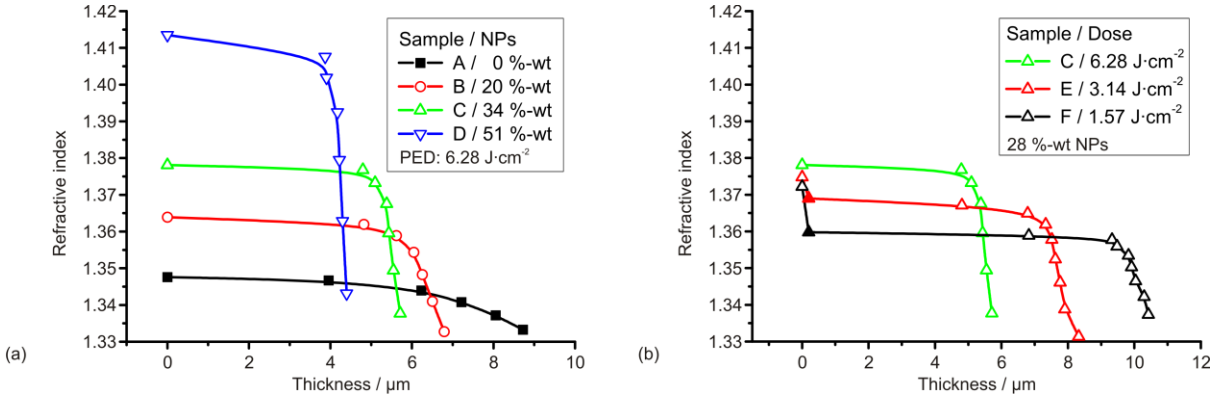

Figure 5.4: Refractive index profiles of *pNIPAAm/NP* composites. a) For samples with varying *NP* content using a constant *PED* (6.28 $J{\cdot}cm^{-2}$). b). For samples with varying *PED* and constant *NP* content (34%-wt) [1].

5.2.2. Homogeneity of Composite Films

A swollen film of pure *pNIPAAm* has a diffuse boundary with water [9,30]. In Figure 5.4, profiles of the refractive index of the films in the height direction (the *z*-direction normal to the substrate surface) are presented based on the reversed Wentzel-Kramers-Brillouin approximation (*rWKB*, see 2.6). Briefly, this approximation yields a refractive index profile in a particular film. According to the effective medium approximation (*EMA*, see 2.7), these profiles reflect the local densities of the films.

The refractive indices at the composite–gold interface (i. e. at 0 μm) were not obtained from *rWKB* analysis but calculated from the position of the surface plasmon resonance (TM_0) in the corresponding spectrum. In Figure 5.4a it can be observed that for pure *pNIPAAm* there was indeed a very gradual transition from the bulk value of *n* to that of the water phase, which spanned almost half the thickness of the swollen layer. The addition of *NPs* to the *pNIPAAm* film lead to a drastic enhancement of the film's homogeneity. This was especially pronounced for sample D containing the greatest fraction of *NPs* (51%-wt): At a height of ca. 4 μm, the refractive index of the film droped sharply, which indicated a well-defined boundary between the film and the water phase.

Figure 5.4b shows that varying the degree of photo-crosslinking did not affect the homogeneity of the films. All films with 34 %-wt *NPs* had a boundary of similar sharpness, despite the fact that the swelling ratio increased from 3.12 to 4.93 for sample C and F.

There was a remarkable discontinuity in the refractive index close to the substrate-composite interface for samples E and F, as can be seen in Figure 5.4b. The refractive indices at the interface were calculated from the surface plasmon resonance angles (at 0 μm). These refractive indicies were a little higher than the values from the *rWKB* approximation close to the interface (marked with solid triangles). As the surface plasmon probed only the first 200 *nm*, these *rWKB* values were placed at 300 *nm*, to express the fact that the refractive index in the bulk was fairly constant. The rise of the refractive index towards the substrate-composite interface was most likely caused by the much higher crosslink density at the interface due to the presence of the monolayer of adhesion promoter. Similar surface effects have been observed for surface-attached *pNIPAAm* films before [9,13].

5.2.3. Determination of the Critical Temperature

The most important aspect of the "smart" behaviour of *pNIPAAm* gels is the reversibility of the swelling and the collapse takeing place around a well-defined temperature T_c. This temperature is closely related to the so-called Lower Critical Solution Temperature (*LCST*) of aqueous *pNIPAAm* polymer chains, where the collapse of the gel resembles spinodal decomposition [7]. However, both the crosslinking and surface-attachment are known to affect T_c [8,9,13,31]. We determined T_c by tracking the angular positions θ of the minima corresponding to TM_0 and TM_1 as a function of temperature between 20 and 45 °*C*. These two modes have very different field distribution functions within the composite films. The surface plasmon mode (TM_0) is excited at the gold-composite interface and is evanescent in the film. Therefore, it is only sensitive to changes in the refractive index in the bottom 150-200 *nm* of the film. In contrast, the TM_1 waveguide mode carries its highest field intensity in the centre of the film, so it is a good probe of the "bulk structure" of the film.

We define the critical temperature T_c as the temperature at which the angle θ is exactly halfway between the "asymptotic" values of θ at 20 °*C* and 45 °*C*, respectively. This definition yields the temperatures T_c^{heat} upon heating and T_c^{cool} upon cooling, respectively.

Effect of Nanoparticle Content on T_c.

Figure 5.5a shows the traces of $\theta(TM_0)$ versus T for samples A–D with varying *NP* content. Remarkably, all the different data sets contained the same features: (1) A gradual onset of the collapse upon heating between approx. 25 – 31 °*C*, (2) a much increased collapse rate with a very large slope between 31 – 33 °*C* and (3) an abrupt end of the collapse when the "asymptotic" angle is reached. Upon cooling the films showed an even more abrupt onset of the reswelling (esp. for samples A–C) at substantially lower temperatures in comparison to the collapse. The reswelling then slowly proceeded until the same state is reached as before the *T*-cycle.

The critical temperatures T_c are plotted as a function of *NP* weight fraction in Figure 5.5b. The collapse temperature $T_c^{heat}(TM_1)$ in the "bulk" of the composites showed a small increase from 31.4 °*C* to 32.2 °*C* by incraesing the *NP* concentartion, whereas $T_c^{heat}(TM_0)$ close to the rigid substrate was not significantly affected by the *NP* content and remained constant at approx. 32.5 °*C*.

The main observations from Figures 5.5a and 5.5b are (1) that the shifts in T_c were remarkably small and (2) that the collapse–reswell cycles showed some hysteresis.

Effect of Photo-Crosslinking Energy Dose on T_c.

Figure 5.5c shows the results of a minimum tracking experiment of $\theta(TM_1)$ with varying *PED* for composites with 34 %-wt *NPs*. The corresponding critical temperatures $T_c^{heat}(TM_1)$ $T_c^{cool}(TM_1)$ are shown in Figure 5.5d. Remarkably, $T_c^{heat}(TM_1)$ was shifted from 31.8 °*C* at 6.28 $J{\cdot}cm^{-2}$ (1 hour crosslinking time) to 37.2 °*C* at 1.57 $J{\cdot}cm^{-2}$ (15 minutes crosslinking time). Meanwhile, $T_c^{cool}(TM_1)$ remained largely unaffected at around 31 – 31.5 °*C*. Thus, the hysteresis at low crosslink densities was much more destinct (*cf.* Sec. 5.2.5).

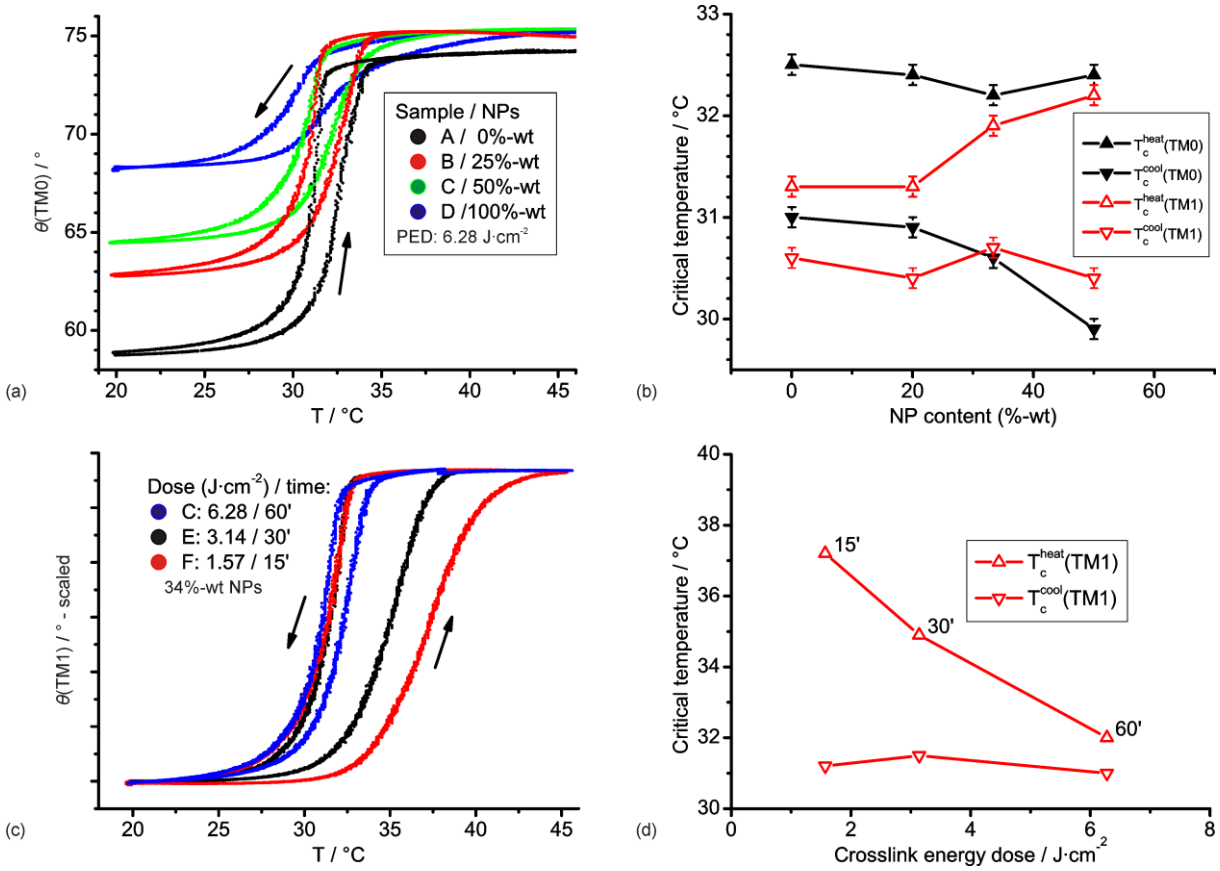

Figure 5.5: (a) Effect of a temperature cycle (20 – 45 °*C*) on the angle of incidence θ at which the surface plasmon mode (TM_0) is excited, for 1/4 composite films with increasing *NP* content. For every cycle, the right half corresponds to the collapse on heating and the left half to the reswelling on cooling, as indicated by the arrows. (b) The critical temperature T_c^{heat} and T_c^{cool} as a function of *NP* content, determined from the temperature cycles in (a) for TM_0 and similar curves for TM_1. (c) Effect of temperature-cycling (20–45 °*C*) on the TM_1 angle for films of *pNIPAAm 1* and *NPs 4* (34%-wt) exposed to varying *PEDs*. (d) The critical temperatures $T_c(TM_1)$ as a function of *PED*, determined from the temperature cycles in (c) for TM_1 [1].

The Trends in T_c^{heat}

According to the literature for bulk *pNIPAAm* gels, crosslinked in the *swollen* state, there was little dependence of T_c^{heat} on the crosslink density [7]. For gels that were crosslinked in the "dry" state, however, Harmon et al. [8] had observed that the critical temperature is shifted down with increasing crosslink density. This shift had been explained as follows: Upon wetting, the gel is driven to swell equally in three dimensions but the binding to the surface only allows pseudo one-dimensional swelling perpendicular to the substrate. The swollen polymer matrix is therefore under compressive stress further away from the substrate

surface. This stress is induced in a (vertical) section of the gel by the drive to 3D expansion of the surrounding polymer and increases on moving away from the substrate. The T_c of a *pNIPAAm* gel is lowered under compression [32]. Indeed there is a difference of approx. 1 *K* between $T_c^{heat}(TM_0)$ at the surface and $T_c^{heat}(TM_1)$ in the bulk for pure *pNIPAAm* (sample A, Figure 5.5b).

A gel that has a lower crosslinking density could reorganize more easily and hence swelled more in the direction normal to the substrate. Therefore, such a gel was under less compression and had a higher T_c^{heat}. When the crosslink density was reduced in our samples by 34 %-wt *NPs* we saw exactly this effect of increasing SR_{1D} (Figure 5.5b) and increasing T_c^{heat} (Fig. 5.5d). Then, why did the amount of *NPs* in the composite hardly affect T_c^{heat}, despite the fact that the *NPs* served as "supercrosslinkers", presenting more than $2 \cdot 10^3$ benzophenone-groups per *NP*, and clearly influencing the *SR* values of the composites? A possible explanation might be given as follows: Crosslinking by *NP*-bound benzophenone leads to the same kind of constriction of the polymer matrix as by an adhesion promoter close to the substrate surface. Therefore, no compressive stress (among the polymer matrix) can be built up close to the *NP* surfaces either. In this model, increasing the *NP* content of the composite is expected to lead to a gradual rise of $T_c^{heat}(TM_1)$ in the middle of the film to the value of $T_c^{heat}(TM_0)$ close to the substrate. This trend was indeed observed in Figure 5.5b. In conclusion, it was due to the rigid nature of the *NPs* and their isotropic binding to the polymer matrix that their presence in the composites had only a small effect on T_c^{heat}.

5.2.4. The Observed Hysteresis

The occurrence of hysteresis between collapse and reswelling (leading to a difference between temperatures T_c^{heat} and T_c^{cool}) is hardly discussed in literature [36], but is of crucial importance when constructing reversible, hydrogel-based sensors, valves or actuators. Figure 5.5a shows that there is some hysteresis even for a pure *pNIPAAm* film. The width of the collapse–swell cycle (and hence the difference between T_c^{heat} and T_c^{cool} in Figure 5.5b) increased only a little with increasing *NP* content, probably due to the growing rigidity of the composite. However, the effect of varying the "bulk" crosslinking density (by varying the *PED*) on the hysteresis was much larger (Figure 5.5c-d). Interestingly, the hysteresis in

composites containing *NPs* was much smaller than in *pNIPAAm* composites with a high clay content reported in the literature [37].

The fact that $T_c^{heat}(TM_1)$ shifted with the crosslink density, while $T_c^{cool}(TM_1)$ did not, implied that collapse and reswelling proceed along different pathways. The collapse is a nucleation-based process [33,34] that can take place everywhere within the film. Reswelling, however, is diffussion controled process which can start only at the water-composite interface by water diffusing through this interface into the film. Moreover, as there is no lateral compression in the collapsed state, no cross-linking effect on T_c^{cool} was expected. Nevertheless it is remarkable how steep the reswelling curve is: the reswelling proceeded within a much smaller *T*-interval than the collapse.

5.2.5. Durable Composite Films

All the observed hysteresis curves were highly reproducible: repeated collapsing and reswelling data for an individual sample superimposed perfectly. This superimposability meant that the composites did not change or degrade during these cycles. It had been observed before [9] and was found here again that there is some material loss during at least the first three cycles for pure *pNIPAAm*. In contrast, we observed for all composites containing *NPs* (even at only 20 %-wt) that the spectra superimpose immediately after the first cycle. This consistency is a strong indication for the high structural stability of the composites: The *NPs* significantly enhanced the chance that all polymer chains in the sample were linked together into a single (percolating) network during the photo-crosslinking. Moreover, any polymer fragments not part of the network but linked to at least on *NP* would be much harder to expel from the gel during temperature cycling. We concluded that the *NPs* improve the durability of *pNIPAAm* films but leave the critical temperature almost unaltered.

5.3 Conclusions

It was shown that homogeneous composite hydrogels consisting of *pNIPAAm* reinforced with nanoparticles could be prepared by making the *NPs* compatible with the polymer by means of surface functionalization. Even though the incorporation of the functionalized *NPs*

reduced the swelling efficiency of the hydrogel matrix, certain improvements in the material properties of the hydrogel could be identified. This composite allowed creating surface-attached thin films with good optical quality that showed very homogeneous swelling when 20 – 50 %-wt *NPs* were present. Furthermore, the swelling ratio could be controlled by the relative amount of particles. Remarkably, the critical temperature of the composite was still fully determined by the polymer matrix and not by the nanoparticles as was shown by the fact that the T_c was not significantly altered by the *NP* content of the samples. The uniform swelling of the composite films compared to pure *pNIPAAm* hydrogels may be explained by the *NPs* serving as supercrosslinkers that kept the gel together more effectively than individual crosslinking groups along the polymer chains. The excellent dispersion of the *NPs* in the *pNIPAAm* matrix also led to a composite of high optical quality, evident by the high coupling efficiencies and low scattering losses in the *SPR/OWS* experiments.

`The unusual properties of these composites make them promising building blocks for future applications. The rigidity of the gels may enable the construction of hydrogel-based microactuators that require a higher mechanical stability than pure *pNIPAAm*. Since T_c was not much affected by the presence of *NPs*, these *NPs* form an ideal scaffold to introduce functional groups that are well embedded into a *pNIPAAm* matrix without changing T_c. This concept is highly useful for sensor applications. The good optical coupling efficiency demonstrated above makes these materials especially suitable for *SPR/OWS*-based sensors [35].

5.4 Experimental Part

5.4.1. Preparation of Composite Films

A composite material of *pNIPAAm* and *NPs* that does not deteriorate on repeated swelling and collapsing requires *NPs* firmly linked to the polymer. Therefore, SiO_2 *NPs* were functionalized with photoreactive benzophenone [24] groups. Thus, a blend of the *NPs* and *pNIPAAm*, which also bears benzophenone groups, can be turned into a single network by photo-crosslinking.

NP* Preparation.** *SiO_2 NPs* were prepared by the sol-gel technique [25,26] and were functionalized in-situ by reacting the silanol (*Si-OH*) groups on the surface with the benzophenone derivative 4-benzoylphenoxypropyl-(triethoxy)silane (*BPTES 2)** using standard trialkoxysilane surface-chemistry [27] (Step 1 in Figure 5.6). Hexamethyldisilazane (*HMDS*) was added to the particle suspension (Step 2), without intermediate work-up. This reacts with any (sterically accessible) unreacted silanol group on the *NP* surface, and thus helps preventing irreversible *NP* aggregation by condensation reactions. The combined surface coverage with *BPTES* and *HMDS* led to particles that were stable in dispersion and were easily redispersed in *$CHCl_3$* or *CH_2Cl_2* without the formation of aggregates.

The functionalized and passivated *NPs* (after step 2 in Figure 5.6) had an average diameter of 35 ± 3 *nm* as determined by scanning electron microscopy (SEM, Zeiss). The number of cross-linking groups on the surface was determined by *UV-Vis* absorption of the benzophenone moieties in a suspension of known particle concentration, using solutions of free *BPTES* as standards. The resulting number of $(1.2 \pm 0.1)\cdot 10^{-4}$ *mol·g*$^{-1}$ (i.e. moles *BPTES* per gram of *NPs*) corresponds to approx. $2.0 - 2.3 \times 10^3$ benzophenone groups per particle (with 35 *nm* ∅) or to one *BP*-silane per 1.7 – 1.9 *nm*^{2} on the *NP* surface.

Film Preparation. Blends of *NPs* and polymer in *$CHCl_3$* solution (Step 3, Figure 1) with varying compositions were used to fabricate films with 0, 20, 34 and 51 %-wt *NP*-content, respectively (Table 1).

Spincoating of these blends (Step 4, Figure 5.6) on *LaSFN9* glass slides with a gold layer functionalized with the thiol adhesion promoter led to smooth and homogeneous films that were crosslinked by *UV* irradiation (λ = 365 *nm*) on the *LaSFN9* substrate.

5.4.2 Materials

Ethanol (*HPLC*-grade, Sigma), chloroform (*HPLC*-grade, VWR), 1,1,1,3,3,3-hexamethyldisilazane (*HMDS*, > 98 %, Carl Roth), 3-Aminoprop-1-yl-triethoxysilane (*APTES*, 98 %, ABCR), and aqueous ammonium hydroxide solution (PA, Fluka) were all used in their original state. Tetraethylorthosilicate (*TEOS*, 98 %, Acros), was distilled before

use. Water of ultra-high purity (*UHP* Water) was obtained from a Milli-Q 185 Plus water purification system (Millipore).

Phenyl(4-(3-(triethoxysilyl)propoxy)phenyl)methanone (**2**, 4-benzoylphenoxypropyl-(triethoxy)silane, *BPTES*), was synthesized as described before [38] by reacting 4-allyloxybenzophenone [39] with triethoxysilane using a platinum catalyst on activated charcoal under an Ar atmosphere.

Syntheses

Terpolymer (*pNIPAAm***)** consisting of *N*-isopropylacrylamide (*NIPAAm*), methacrylic acid (*MAA*) and 4-benzoylphenyl methacrylate [30] (*MABP*) in a random distribution was synthesized by radical polymerization similar to Beines et al. [9]. Determination of the polymer composition from ^{1}*H-NMR* required several spectra in different media and revealed that the polymer consists of 94 mol% *NIPAAm*, 5 mol% *MAA* and 1 *mo*l% *MABP*, equal to the composition of the monomer mixture. Molecular weight: *Mw* = 213500, *Mn* = 89600, *PDI* = 2.38 (*GPC, DMF, PMMA* standard). This corresponded to about 20 benzophenone crosslinker units per polymer chain.

SiO$_2$-NPs were prepared following a method adapted from Giesche et al. [25], using the Stoeber process [26]. A stock solution of *TEOS* (0.14 *M*) in ethanol (5 *ml*) was diluted with ethanol (20 *ml*), warmed to 60 °*C* and added to a stirred mixture of aqueous ammonia (0.86 *M*, 10 *ml*) and ethanol (125 *ml*) in a reactor flask kept at 60 °*C*. The mixture was stirred overnight at 60 °*C* and became slightly turbid. The reaction was run to complete conversion with a quantitative yield of *NPs* (average diameter 35 ± 3 *nm* after silanisation). The crude reaction mixture was used in the following experiments without intermediate workup (in order to prevent coalescence/aggregation of the *NPs*).

***BPTES*-coated *NPs*.** An ethanolic solution (7 *ml*) of the benzophenone silane (300 *mg*, 0.74 *mmol*) was added to the "crude" *SiO$_2$* colloidal suspension. After stirring in the dark for

12 hours, *HMDS* (1 *ml*) was added and the mixture was stirred in the dark for another 12 hours. The resulting suspension was dialyzed against ethanol (2 *l*) for 5 days (using a Roth Visking regenerated cellulose membrane, cut-off M_W = 14,000) and further purified by ultrafiltration over a Millipore PL filter (cut-off M_W = 20,000). By repeatedly concentrating the mixture and diluting, first with ethanol and then with $CHCl_3$, a suspension is obtained that is virtually free from non-particulate impurities (< 0.1 % of the original concentration) and contains < 2 % ethanol. The nanoparticle content as determined by gravimetry was 1.1 %-wt. The suspension was stored in the dark at -20 °*C* and remained stable for months. Silica nanoparticles that were only passivated with *HMDS* were prepared by similar means.

Functionalized Glass Substrates for Optical Characterisation

LaSFN9 glass slides (Hellma Optik GmBH, Jena) were cut into 25×25 *mm* pieces, cleaned by immersion in a 2 % Hellmanex solution (Hellma Optik), rinsed with copious amounts of *UHP* water and ethanol and dried in an argon stream. They were coated with 1.8 *nm* Cr and 50 *nm* Au by thermal evaporation using an Edwards Auto 306 evaporator. The slides were immersed in an argon-flushed solution of the adhesion promoter 3-(4-benzoylphenoxy)propanethiol (*BPSH*) (approx. 0.5 *mg/ml*) for 5 hours, washed 3× with ethanol, and stored in the dark under an argon atmosphere until further use.

Preparation of Nanoparticle/Hydrogel Composite Films

About 20 *ml* of the 1.1 %-stock suspension of *NPs4* was concentrated by rotary evaporation of the solvent to a volume of 3.7 *ml* to yield a suspension of 6 %-wt. Amounts of this suspension were combined with *pNIPAAm* and $CHCl_3$ to yield blends of overall compositions. All blends were homogenized by orbital shaking at 250 *rpm* overnight in darkened containers, yielding clear suspensions. *pNIPAAm/NP* composite films were prepared from these blends by spin-coating (4500 *rpm*, 60 *s*) onto the functionalised *LaSFN9* glass slides. The samples were dried at 50 °*C* in vacuum for 8 hours. The films were cross-linked by *UV* irradiation (365 *nm*) in a Stratalinker 2400 (Stratagene). The total photocrosslinking energy dose (*PED*) was varied from 1.57 to 6.28 $J \cdot cm^{-2}$ for different samples by varying the exposure time from 15 to 60 *min*. All deposition parameters were

chosen in such a way that films with a sufficient thickness ($\geq 1000\ nm$) were obtained allowing both surface plasmon resonance and the generation of optical waveguide modes in the film.

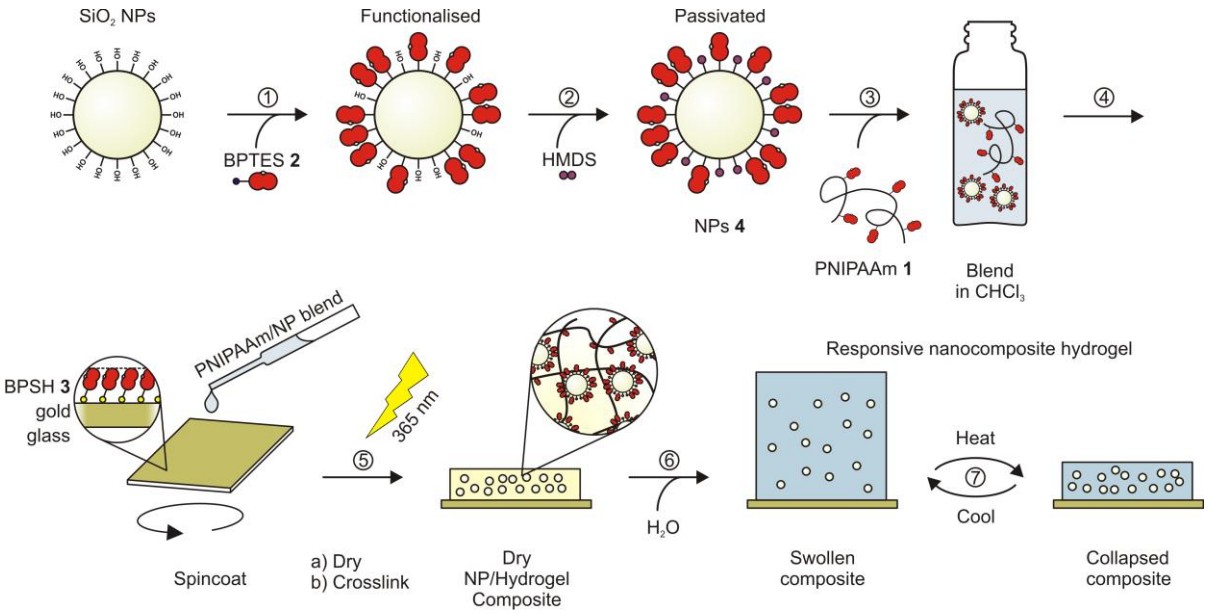

Figure 5.6: Preparation of photoreactive functionalized SiO_2 *NPs*, preparation of nanocomposite hydrogel films on substrates [1].

5.4.3 Analysis

Surface Plasmon Resonance and Optical Waveguide Spectroscopy

Setup. *SPR/OWS* was carried out in the Kretschmann configuration with a customized setup described in chapter 3.1. Opposite to the prism, a 1 ml flow cell was mounted on the sample and connected to a peristaltic pump, so that the sample could be measured in a fluid. The temperature of the flow-cell and sample could be controlled with an electronically controlled, water-cooled resistive heater and either set at a constant temperature (15–50 °*C*) or ramped up or down at controlled rates, with an accuracy of 0.1 *K*.

Swelling experiments. To fully characterize the swelling behaviour of the hydrogel/nanoparticle composite films, they were subjected to a measurement protocol that typically looked as follows:

(*i*) An angular scan of $I(\theta)$ of the film in the dry state.

(*ii*) The flowcell was filled and rinsed with *UHP* water for approx. 1 *min*. The flow was then turned off and the film was allowed to swell and equilibrate for 15 *min*.

(*iii*) Three collapse–swell cycles (cycling the temperature from 20 °*C* to 45 °*C* and back) to "prime" the composite films. (*iv*) Equilibration at 20 °*C* for 20 *min*. (*v*) Ramp *T* up from 20 °*C* to 45 °*C* at 0.1 $K \cdot min^{-1}$. (*vi*) Equilibrate for 15 *min*. (*vii*) Ramp down to 20 °*C* at 0.1 $K \cdot min^{-1}$.

The priming in step (*iii*) ensures high reproducibility of angular and temperature scans. Angular scans of $I(\theta)$ were recorded at 20 °*C* and 45 °*C* at different stages of the temperature programme, using *p*-polarised light to excite the plasmon resonance (TM_0) and couple into the transverse magnetic waveguide modes TM_n. Similar scans with *TE*-polarization allowed coupling into the transverse electric modes TE_n. Steps *v–vii* were performed twice, tracking $\theta(TM_0)$ and $\theta(TM_1)$ respectively, as a function of temperature with 5 or 10 *s* time intervals. Each individual tracking experiment lasted approx. 10 hours, the slow ramp ensuring that the system deviated only marginally from thermal equilibrium throughout the cycle.

Modeling *SPR/OWS* Spectra. The angle-dependent reflectivity of the hydrogel/nanoparticle film samples was modeled by solving the Fresnel equations for a planar multilayer system by a transfer-matrix algorithm descriped in Chapter 2. In the so-called *box-model* one average refractive index is assumed for the entire film. For samples with a density gradient, the *rWKB* method as described in Chapter 2.6 was applied.

References

[1] Van den Brom, C., Anaç, I., Roskamp, R.F., Retsch, M., Jonas, U., Menges, B., and Preece, J.A., *J. Mater. Chem.*, **2010,** 20 (23), 4827.4839.

[2] P. Schexnailder and G. Schmidt, *Colloid Polym Sci*, 2009, **287**, 1-11.

[3] D. R. Paul and L. M. Robeson, *Polymer*, 2008, **49**, 3187-3204.

4] V. Pardo-Yissar, R. Gabai, A. N. Shipway, T. Bourenko and I. Willner, *Adv. Mater.*, 2001, **13**, 1320-1323.

[5] I. Tokarev, I. Tokareva and S. Minko, *Adv. Mater.*, 2008, **20**, 2730-2734.[6] J. M. Weissman, H. B. Sunkara, A. S. Tse and S. A. Asher, *Science*, 1996, **274**, 959-960.

[6] J. M. Weissman, H. B. Sunkara, A. S. Tse and S. A. Asher, *Science*, 1996, **274**, 959-960.

[7] J. H. Holtz and S. A. Asher, *Nature*, 1997, **389**, 829-832.

[8] H. G. Schild, *Prog. Polym. Sci.*, 1992, **17**, 163-249.

[9] M. E. Harmon, D. Kuckling, P. Pareek and C. W. Frank, *Langmuir*, 2003, **19**, 10947-10956.

[10] P. W. Beines, I. Klosterkamp, B. Menges, U. Jonas and W. Knoll, *Langmuir*, 2007, **23**, 2231-2238.

[11] I. Tokarev and S. Minko, *Soft Matter*, 2009, **5**, 511-524.

[12] M. E. Harmon, T. A. M. Jakob, W. Knoll and C. W. Frank, *Macromol.*, 2002, **35**, 5999-6004.

[13] D. Kuckling, M. E. Harmon and C. W. Frank, *Macromol.*, 2002, **35**, 6377-6383.

[14] M. E. Harmon, D. Kuckling and C. W. Frank, *Macromol.*, 2003, **36**, 162-172.

[15] K. Haraguchi and H. J. Li, *Macromol.*, 2006, **39**, 1898-1905.

[16] Z. Yang, Z. Cao, H. Sun and Y. Li, *Adv. Mater.*, 2008, **20**, 2201-2205.

[17] C. Wang, N. T. Flynn and R. Langer, *Adv. Mater.*, 2004, **16**, 1074-1079.

[18] L. Sheeney-Haj-Ichia, G. Sharabi and I. Willner, *Adv. Func. Mater.*, 2002, **12**, 27-32.

[19] S. R. Sershen, S. L. Westcott, J. L. West and N. J. Halas, *Appl. Phys. B*, 2001, **73**, 379-381.

[20] A. Sidorenko, T. Krupenkin, A. Taylor, P. Fratzl and J. Aizenberg, *Science*, 2007, **315**, 487-490.

[21] Y. J. Lee and P. V. Braun, *Adv. Mater.*, 2003, **15**, 563-566.

[22] K. S. Liao, H. Fu, A. Wan, J. D. Batteas and D. E. Bergbreiter, *Langmuir*, 2009, **25**, 26-28.

[23] T.-a. Asoh, M. Matsusaki, T. Kaneko and M. Akashi, *Adv. Mater.*, 2008, **20**, 2080-2083.

[24] N. J. Turro, *Modern Molecular Photochemistry*, University Science Books, 1991, Mill Valley, CA, 1991.

[25] H. Giesche, *J. Eur. Ceram. Soc.*, 1994, **14**, 189-204.

[26] W. Stöber, A. Fink and E. Bohn, *J. Coll. Interf. Sci.*, 1968, **26**, 62-69.

[27] A. Ulman, *Chem. Rev.*, 1996, **96**, 1533-1554.

[28] D. A. G. Bruggeman, *Ann. Phys.*, 1935, **24**, 636-664.

[29] *CRC Handbook of Chemistry and Physics*, CRC Press/Taylor and Francis, Boca Raton. FL, 2009.

[30] R. Toomey, D. Freidank and J. Rühe, *Macromol.*, 2004, **37**, 882-887.

[31] M. J. N. Junk, R. Berger and U. Jonas, *submitted to Langmuir*, 2009.

[32] S. Hirotsu, *J. Chem. Phys.*, 1991, **94**, 3949-3957; A. Suzuki, *Adv. Polym. Sci.*, 1993, **110**, 199-240.

[33] M. J. N. Junk, U. Jonas and D. Hinderberger, *Small*, 2008, **4**, 1485-1493.

[34] F. Ikkai and M. Shibayama, *J. Polym. Sci. B*, 2005, **43**, 617-628; M. Shibayama, *Bull. Chem. Soc. Jpn.*, 2006, **79**, 1799-1819.
[35] J. Homola, *Chem. Rev.*, 2008, **108**, 462-493.
[36] M. Guenther, G. Gerlach and T. Wallmersperger, *J. Intelligent Mater. Syst. Struct.*, 2009, **20**, 949-961.
[37] Y. Liu, M. F. Zhu, X. L. Liu, Y. M. J. Ang, Y. Ma, Z. Y. Qin, D. Kuckling and H. J. P. Adler, *Macromol. Symp.*, 2007, **254**, 353-360.
[38] M. Gianneli, R. F. Roskamp, U. Jonas, B. Loppinet, G. Fytas and W. Knoll, *Soft Matter*, 2008, **4**, 1443-1447.
[39] O. Prucker, C. A. Naumann, J. Rühe, W. Knoll and C. W. Frank, *J. Am. Chem. Soc.*, 1 999, **121**, 8766-8770.

6 Cononsolvency Effects

Surface plasmon resonance / optical waveguide spectroscopy was used to study the cononsolvency effect on the swelling behaviour of thin, surface attached and photo-crosslinked poly(*N*-isopropylacrylamide) (*pNIPAAm*) gel layers in water-ethanol mixtures. The transition temperature of the gel layers first decreased upon ethanol addition to the aqueous swelling medium and increased again at higher ethanol fractions due to the cononsolvency effect of the solvent mixture.

The investigation of cononsolvency effects in ethanol-water mixtures was a cooperation with Ilke Anac who performed the measurements, Alena Aulasevich, Matthias J. N. Junk, Piotr Jakubowicz, Robert F. Roskamp, Ulrich Jonas and Wolfgang Knoll. More details can be found in the published paper [1].

6.1 Introduction

The swelling state of a sensor gel film matrix is affected by environmental changes and analyte binding. In order to fully understand the sensor response, it is necessary to deconvolute the effect of specific analyte binding and the influence of unspecific environmental parameters. In particular *pNIPAAm* gels show an unusual swelling behaviour in mixed solvents and this compositional effect of the liquid medium in contact with the active matrix is of substantial technological relevance for sensor design and implementation. The gels swell in pure water as well as in some organic solvents such as acetone, ethanol, methanol, *THF* or *DMSO*, but may collapse in the corresponding water-organic solvent mixtures [2]. This behaviour has been termed “cononsolvency”. It can be related to the demixing and complexation of two solvents [3]. The cononsolvency behaviour for 3-dimensional polymer systems in solutions and as bulk gel networks has been studied [2-5] and the general physics behind it is discussed in the literature [6-7]. However, for 2D architectures of the responsive gels only little information is available. Napper et al. studied the swelling behaviour of *pNIPAAm* chains at interfaces of polystyrene lattices dispersed in a binary mixture of water and methanol, ethanol and 2-propanol by dynamic light scattering (*DLS*) [8]. However, the transition temperature of surface attached films of *pNIPAAm* gel networks in mixed solvents has not been investigated previously.

Surface plasmon resonance spectroscopy (*SPR*) is a powerful technique to determine the refractive index and thickness of thin polymer films [9], however the independent determination of both quantities is not possible by *SPR* spectroscopy at one wavelength only. If the polymer film is sufficiently thick (d ≥ 500 *nm*), optical waveguide modes (*OWS*) can be exited in the material, which allows a detailed film characterization and an independent determination of thickness and refractive index [10].

This technique was implemented here to investigate the cononsolvency effect of water-ethanol mixtures at varying temperature on the swelling behaviour of responsive *pNIPAAm* films of micrometre thicknesses. Additionally, the refractive index gradient perpendicular to the swollen gel film surface in ethanol and water was analysed by the reversed Wentzel-Kramers-Brillouin (*rWKB*) approximation [11].

The investigated material consisted of a terpolymer synthesized by free radical polymerization from *N*-isopropylacrylamide (*NIPAAm*), methacrylic acid (*MAA*) and 4-methacryloyloxybenzophenone (*MABP*), which was spin-coated on a solid substrate as a photo-crosslinkable film [11, 12, 13] . Covalent adhesion of the thin polymer film onto agold-coated substrate was achieved with a photoreactive thiol derivative analogous to 4-Methacryloyl-benzophenone (*MABP*).

6.2 Results and Discussion

6.2.1. Swelling Behaviour

An important factor, determining the permeability of hydrogel films for diffusing molecules of different sizes, which is highly relevant for sensor designs, is given by the swelling ratio. The effect of the crosslinking energy dose on the swelling ratio in ethanol of the surface-attached *pNIPAAm* films on 4-benzoylphenoxypropyl-(triethoxy)silane *BPSH-Au* substrates at room temperature is shown in Figure 6.1A. The swelling ratio was defined as the ratio of the film thickness swollen in ethanol normalized by that in the dry state. The thickness in the swollen state was calculated from the *SPR/OWS* data assuming an average refractive index for the entire layer [11]. The data were fitted by adjusting the fit parameter to the first and last waveguide modes since the first waveguide mode is most sensitive to the refractive index while the last one is most

sensitive to the thickness of the film. As the crosslinking energy dose was increased, a decreasing swelling ratio was observed up to an energy dose of 2.8 $J\ cm^{-2}$ (corresponding to a crosslinking time of 180 *min*). No further change of the swelling ratio was found for higher energy doses. This result is consistent with fluorescence correlation spectroscopy (*FCS*) experiments [14], where the "translational" diffusion of tracer molecules was investigated to probe structural properties of grafted, crosslinked *pNIPAAm* films swollen in ethanol. It was very difficult to obtain the waveguide modes at shorter crosslinking times (less than 60 *min*) and only 40 % of the samples with 15 *min* crosslinking time showed waveguide mode excitation. This was most likely due to strong heterogeneities, which were introduced into the gel film upon exposure to the solvent and dissolution of unbound material. This hypothesis would also explain why it was difficult to measure the waveguide modes for these samples in the dry state after swelling. Nevertheless, the swelling ratio (after the first swelling and drying cycle, at 15 *min* crosslinking time) could be obtained for two samples. In order to measure the waveguide modes and calculate the swelling ratios at crosslinking times shorter than 60 *min* more reproducibly, a polystyrene (*PS*) adhesion promoter layer between the gold substrate and the hydrogel film was applied. Figure 6.1B shows the swelling ratio of *pNIPAAm* films prepared with the *PS* adhesion layer in ethanol at room temperature as a function of crosslinking energy dose and time. A decrease in swelling ratio was also observed for the *pNIPAAm* layers on *PS* as the energy dose increases. (Figure 6.1B)

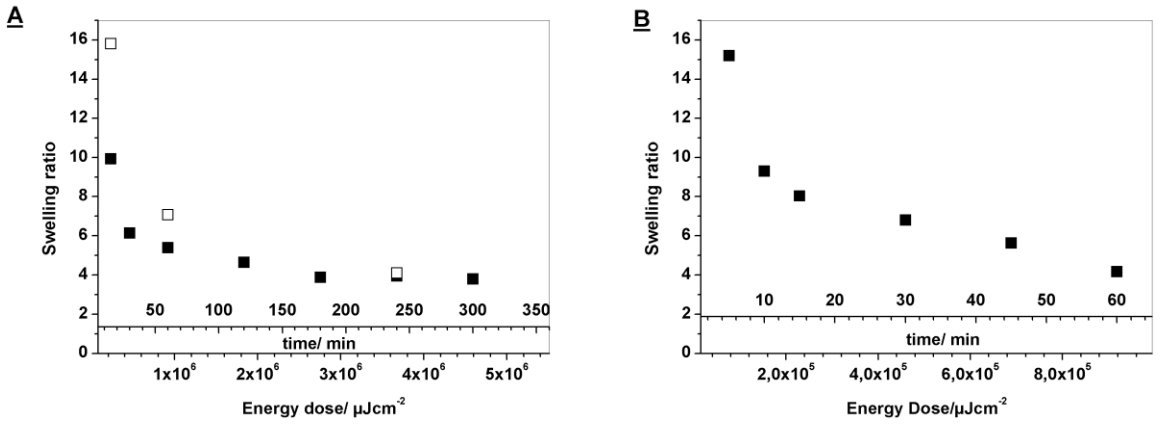

Figure 6.1: Initial swelling ratios (filled squares) and swelling ratios after the first swelling-drying cycle (open squares) of the photo-crosslinked *pNIPAAm* terpolymer (A) on *BPSH* modified gold substrates ($d_{dry} \approx 1.3\ \mu m$) and (B) on *PS* ($d_{dry} \approx 350\ nm$) swollen in ethanol at room temperature as a function of the crosslinking energy dose and time (t_{xl}) [1].

When the gel layer was exposed to ethanol for the first time, it still contained some non-crosslinked chains. Therefore, the photo-crosslinked *pNIPAAm* layer (t_{xl} = 60 *min*) with a dry thickness of 1.7 μm was initially swollen in ethanol five times to reach a stable thickness and to remove the non-crosslinked chains. Between each cycle, the films were dried in vacuum for an hour and the thickness of the dry layer was measured. Due to unbound polymer loss, the dry layer thickness decreased to 1.3 μm after the first swelling-drying cycle and became stable afterwards within ± 0.1 μm deviation. After five swelling-drying cycles, the layer thickness did not change anymore and we assumed the films did not contain any unattached chains any more. The swelling ratio of the gel film increased from initially 5.39 to 7.44 after those swelling-drying cycles. Washing out the free polymer increases the free volume in the gel, which is filled by the swelling solvent in the swollen state and results in thinner gels after swelling-drying cycles. This particularly led to a more heterogeneous structure and a reduction in wave guiding capacity in films with low crosslinking density, as discussed above. For the detailed study of the swelling behaviour and the transition temperature in water-ethanol mixtures with varying composition, *pNIPAAm* gel layers with a crosslinking time of 60 *min* were used throughout the work reported here.

6.2.2. Refractive Index Gradients in Water and Ethanol

The refractive index profiles calculated by *rWKB* from the *SPR/OWS* measurements of photo-crosslinked *pNIPAAm* terpolymer layers swollen in water and in ethanol at room temperature are presented in Figure 6.2. The refractive index continually decreased with increasing distance from the substrate/hydrogel interface toward the interface of the hydrogel with the water or ethanol phase. The corresponding swelling ratios showed a higher solvent content and a stronger swelling in ethanol (Swelling Ratio *SR* 7.44) than in water (*SR* 5.44). The observed difference in these swelling ratios could be predicted by comparing the Hildebrand solubility [15,36] parameters (δ) of *pNIPAAm* (δ_{gel} = 11.5 $(cal/cm^3)^{1/2}$), ethanol (δ_{EtOH} = 12.7 $(cal/cm^3)^{1/2}$) and water (δ_{water} = 23.4 $(cal/cm^3)^{1/2}$) [16,37]. A stronger swelling of the *pNIPAAm* gel layers in ethanol would be suggested by the similarity of the Hildebrand solubility of ethanol to that of *pNIPAAm*.

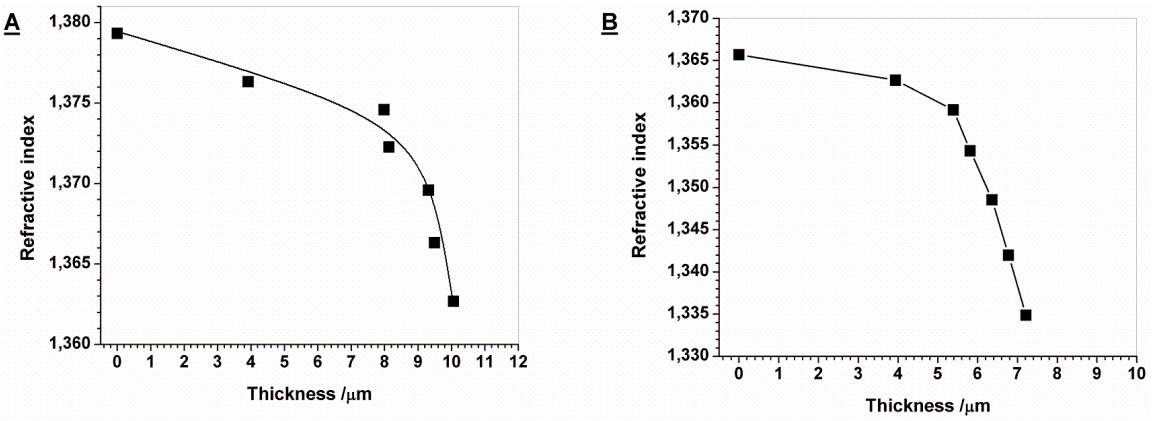

Figure 6.2: Refractive index profiles of photo-crosslinked *pNIPAAm* terpolymer layers (t_{xl} = 60 min) at room temperature (A) in ethanol and (B) in water, as calculated by the reversed *WKB* approximation [1].

6.2.3 Transition Temperatures

Probably the most important parameter describing the response behaviour of thermo-sensitive gel films is given by the transition temperature, at which the gel switches between a swollen and a collapsed state. For this purpose, the temperature-dependent swelling behaviour of the photo-crosslinked *pNIPAAm* terpolymer layers was measured in ethanol, water, and in water-ethanol mixtures. In Figure 6.3A, the angles of incidence of the TM_1 mode are plotted as a function of temperature instead of the layer thickness or refractive index to avoid the use of the box model. The solid lines represent sigmoidal Boltzmann fits using equation 6.1, which was adapted from the literature [17,20] but replacing the refractive index values by the TM_1 coupling angles. A_1 is the asymptotic value of the coupling angle of the TM_1 waveguide modes at low temperatures, A_2 is the corresponding one at high temperature, and T_c is the inflection of the curve, which is taken as the transition temperature (T_c).

$$y = A_2 + \frac{A_1 - A_2}{1 + \exp\left(\frac{T - T_c}{\Delta T_c}\right)} \qquad (6.1)$$

The gel layer in ethanol hardly showed any temperature dependent behaviour - no volume collapse was observed. However, a slight decrease in the angle of incidence and refractive index was observed as the temperature increased. In contrast, in pure water the transition temperature for the volume collapse (T_c) of the terpolymer layer was 32.8 °*C*. A drastic change in the

transition temperature was observed by adding small amounts of ethanol, e.g. the T_c dropped to 29.7 °*C* in a water-ethanol (v/v) mixture containing only 0.25 % ethanol. This result clearly indicates a strong cononsolvency behaviour of the water-ethanol mixture for the responsive *pNIPAAm* layers.

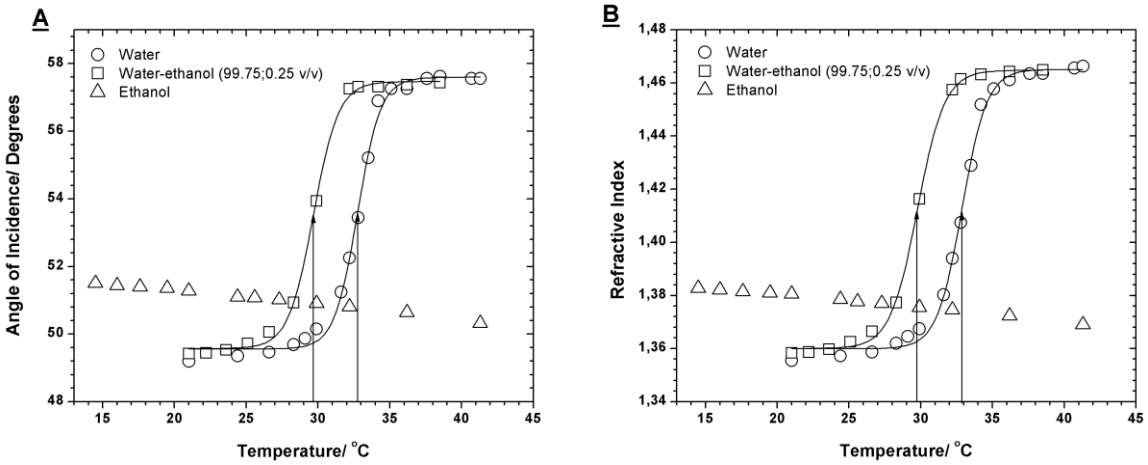

Figure 6.3: (A) Coupling angles of the TM_1 waveguide modes from the *OWS* measurements and (B) refractive indices (box model simulation) of the crosslinked *pNIPAAm* gels (t_{xl} = 60 *min*) plotted as a function of temperature in ethanol (triangles), in water (circles) and in water-ethanol (99.75:0.25 v/v) mixture (squares). The sigmoidal Boltzmann fits of the measured data are displayed as solid lines [1].

In Figure 6.3B, the refractive indices of the gel layer are plotted as a function of temperature. The average refractive indices are obtained by analyzing the *SPR/OWS* data with the box model. As for the TM_1 angles above, the sigmoidal Boltzmann fits (solid lines) of equation 6.1 were obtained with A_1 as the asymptotic refractive index at low temperatures and A_2 the one for high temperatures. The inflection point of the curve indicates the transition temperature T_c. Since the temperature dependence of these box model refractive indices is the same as the temperature dependence of the TM_1 mode (Figure 6.3A), the box model can be used as an approximation for the description of the gel transition.

6.2.4. Cononsolvency in Gel Layers

Although ethanol and water are both solvents for the *pNIPAAm* terpolymer at room temperature, the transition temperature of the gels decreased rapidly upon an increase in ethanol volume fraction, as displayed in Figure 6.4. As discussed for Figure 6.3, the T_c obtained from the

box model refractive index was nearly the same to the T_c obtained from the angle of incidence of the TM_1 mode. Higher volume fractions of ethanol (30 %, 40 %, 50 %, 60 %) were also tested but no transition temperatures could be recorded as the layers were already in a collapsed state even at the lowest possible temperature (10 $°C$) that could be tested by the *SPR* setup. In the current *SPR* configuration it is technically impossible to run *SPR* scans at temperatures below 10 ^oC due to condensation of water on the prism. At 70 % ethanol volume fraction, a reentrant transition temperature was observed for the gel layers (40.2 ^oC from the TM_1 mode angle, and 40.6 ^oC from the box model refractive index). For ethanol volume fractions above 70 % no transition temperatures could be recorded, as it may exceed the boiling point of the mixture. At these high ethanol concentrations the layers were always in the swollen state. As mentioned before, induced phase separation by the addition of a good organic solvent to the aqueous solution of *pNIPAAm* has been termed as cononsolvency. Such cononsolvency behaviour was explained by the combination of three binary interaction parameters (χ) based on Flory-Huggins solution theory calculations [4] and also by the formation of stoichiometric "complexes" between the different solvent molecules [3]. The driving force for cononsolvency is discussed as the preference of water to complex with the organic solvent rather than to interact with *pNIPAAm*. This is indicated by the negative value of the binary interaction parameter (χ) between the organic solvents and water in a *pNIPAAm* solution [4] which promotes more polymer-polymer contacts and triggers the collapse of the polymer. As the ratio of the organic solvent in the mixture further increases, *pNIPAAm* chains become soluble again in the excess of the organic solvent molecules in the solvent mixture. In our system the following three relevant kinds of intermolecular interactions existed, the interactions (1) between water and *pNIPAAm*, (2) between ethanol and *pNIPAAm* and (3) between ethanol and water besides the three trivial symmetric interactions water-water, ethanol-ethanol and *pNIPAAm-pNIPAAm*. Our results at lower ethanol volume fractions indicated that water/ethanol dominated the other two interactions, promoting more polymer-polymer segment contacts and hence resulting in a decrease of T_c with the collapse of the polymer layer. As the ethanol volume fraction increased in our system, the interactions between the *pNIPAAm* and ethanol dominated and the *pNIPAAm* chains became soluble in the excess ethanol, leading to an increased in T_c.

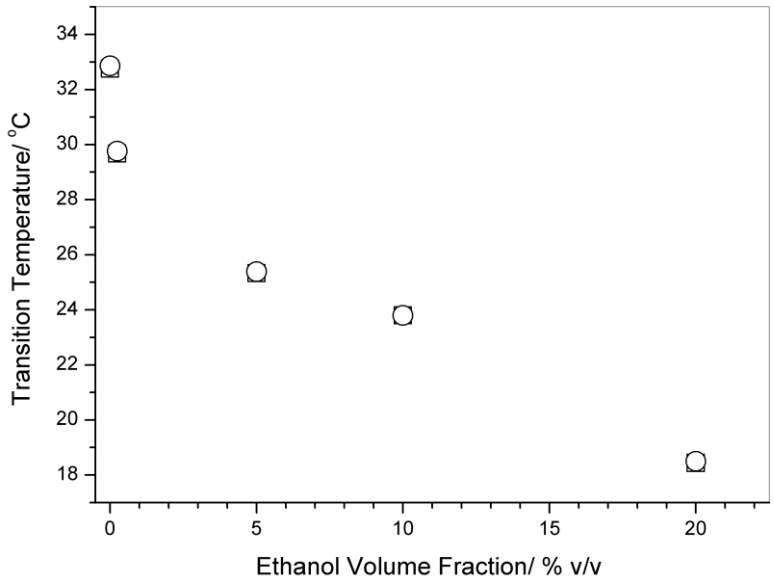

Figure 6.4: Transition temperatures of photo-crosslinked *pNIPAAm* gels as a function of the ethanol volume fraction. The transition temperature is defined as the inflection point of the sigmoidal Boltzmann fits based on either the TM_1 coupling angle (squares) or the average refractive indices calculated from the *SPR/OWS* data with the box model (circles) [1].

6.3. Conclusions

From the *SPR/OWS* results it could be concluded that *pNIPAAm* layers immobilized on gold substrates in mixed solvents behaved similar to the *pNIPAAm* solutions reported in the literature [4,18,24,38] . First they showed a decrease in T_c by the addition of a good organic solvent to the aqueous solution of *pNIPAAm* (up to 20 % ethanol) and at higher fractions of good organic solvent (70 % ethanol) the T_c increased and possibly exceeded the boiling point of the mixture. In our measurements, the $T_c s$ seemed to be below 10 ^oC for ethanol volume fractions between 30 – 60 %, as is observed for *pNIPAAm* solutions in mixed solvents in the literature [3, 4,18,23,24,28]. Thus, a controlled addition of ethanol as cononsolvent could be used to trigger the volume transition of the gel at a desired temperature.

Furthermore, the obtained results were particularly important when considering *pNIPAAm* as responsive matrix material in sensor applications. Cononsolvency presents an interesting tool for deliberately inducing the collapse of the sensor gel matrix after analyte binding by a change of solvent composition. Thus, the bound analyte would be locally concentrated at the sensor interface before a signal read-out. The study of cononsolvency also provided valuable

information on potential composition effects in analyte solutions, which have to be taken into account in designing a reliable sensor and accurately interpret a sensor response.

6.4. Experimental Section

Materials: Methacrylic acid (*MAA*, 99 %) was purchased from Sigma-Aldrich and distilled prior to use. *N*-Isopropylacrylamide (*NIPAAm*, 99 %, Acros) was recrystallized from a mixture of toluene/hexane (1/4) and 2,2'-Azobis-(isobutyronitrile) (*AIBN*, 98 %, Acros) was recrystallized from methanol. Dioxane was distilled over calcium hydride and dried over a molecular sieve (0.4 *nm*). Thioacetic acid (*AcSH*, 98 %, Acros) and ethanol (*HPLC* grade, > 99 %, Sigma Aldrich) were used as received. Water was purified using a Millipore water system that involves reverse osmosis, ion exchange, and filtration steps to achieve a resistivity of 18.2 $M\Omega\,cm$. Water purified by this method is referred to as Milli-Q water.

4-Methacryloyloxybenzophenone (*MABP*) [13] and 4-allyloxybenzophenone [19], propyl 3-(4-benzoylphenoxy) thioacetate (*BPSAc*) [11] were synthesized according to the literature. The *pNIPAAm* terpolymers, having 94 eq of *NIPAAm*, 5 eq of *MAA* and 1 eq of *MABP* (*pNIPAAm-1*) and having 88 of *NIPAAm*, 10 eq of *MAA* and 2 eq of *MABP* (*pNIPAAm-2*), were synthesized by free radical polymerization according to the literature [11]. (Scheme 1)

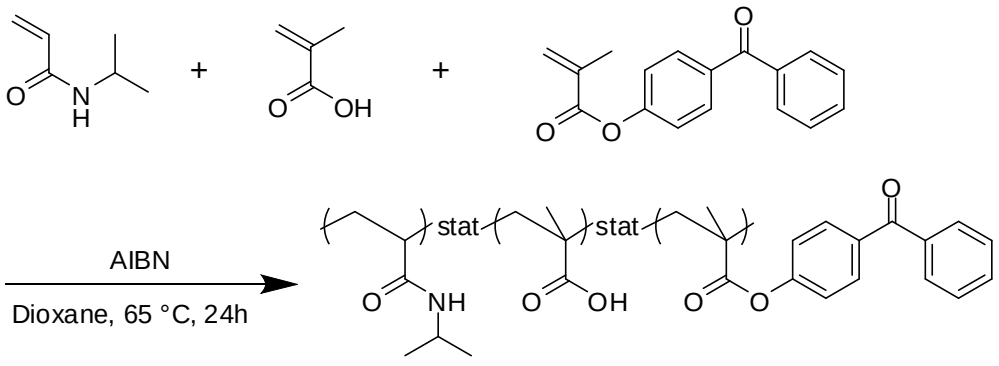

Scheme 6.1: Synthesis of the statistical *pNIPAAm* terpolymer [1].

The average molecular weight (M_w = 266 $kgmol^{-1}$) and the molecular weight distributions (polydispersity index M_w/M_n = 3.52) of polymers were determined by gel permeation chromatography at 60 °*C* in *DMF*, polystyrene (*PS*) served as internal standard.

Synthesis of 3-(4-Benzoylphenoxy)propanethiol (*BPSH*) (Scheme 2): For this synthesis, the synthetic scheme of Bilokin et al. was adapted and modified [20]. A solution of *KOH* (0.547 *g*, 9.75 *mmol*) in methanol (7.5 *ml*) was cooled to 0 °*C* and purged with argon for 15 *min. BPSAc* (2.45 *g*, 7.79 *mmol*) was added to this solution and stirred for 18 *h* at room temperature. The reaction mixture was quenched with H_2O and 25 *ml* ethyl acetate was then added to the media. The aqueous phase was extracted with ethyl acetate (3 x 25 *ml*) and the combined organic extracts were washed with 50 *ml* H_2O and dried over Na_2SO_4. The solvent was removed in vacuum. A 2:1 mixture of thiol (*BPSH*) and disulfide (*BPDs*) was obtained and used as such for the adsorption to gold substrates. The yield was 94 %.

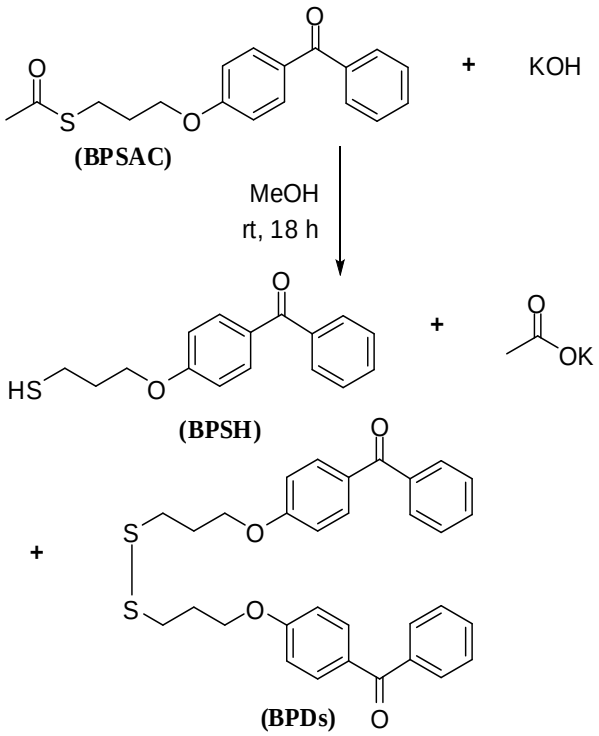

Scheme 6.2: Synthesis of 3-(4-benzoylphenoxy)propanethiol (*BPSH*) [1].

Sample Preparation for *SPR* Measurements: *LaSFN9* glass slides (Hellma Optik GmBH, Jena) were coated with chromium (2 *nm*) and gold (50 *nm*) by thermal evaporation in an Edwards auto 306 evaporator. Samples were prepared by two methods, which are schematically shown in Scheme 3. In the first method, the gold substrates were immersed in a solution of *BPSH* (5 *mM*) in ethanol at room temperature for 24 *h* and then rinsed with ethanol and dried with nitrogen. Both thiols and disulfides form monolayers on a gold surface with a comparable stability. Thus, it was not necessary to remove the 30 % disulfide content in the *BPSH* solution prior to monolayer formation. Thin *pNIPAAm* films were prepared by spin-coating (5000 *rpm*, 60 *s*) from a 10 % w/v *pNIPAAm* ethanol solution onto the *BPSH* modified substrates (Scheme 3A). The samples were then dried at 50 °*C* in vacuum oven for 12 *h*. The thickness of the dry films was approximately 1- 1.8 μm as calculated from *SPR/OWS* measurements. The polymer was both crosslinked and attached to the *BPSH* modified substrate via *UV* irradiation at λ = 365 *nm* with an optical power of 1.74 $W\,cm^{-2}$ (Stratalinker 2400, Stratagene). The crosslinking density was varied by changing the crosslinking time from 15 *min* to 300 *min* respectively.

In the second method, a thin polystyrene (*PS*) layer (50 *nm*) on the gold substrates was prepared by spin-coating (1000 *rpm*, 60 *s*) from a 0.8 % w/v polystyrene-toluene solution. The samples were then dried at 50 °C in a vacuum oven for 12 *h*. The thin *pNIPAAm* layer (50 *nm*) was prepared by spin-coating (4000 *rpm*, 60 *s*) from a 0.5 % w/v *pNIPAAm* ethanol solution onto the PS film. The samples were then dried at 50 °*C* in a vacuum oven for 12 *h*. The *pNIPAAm* layer was crosslinked and attached to the *PS* surface by *UV* irradiation at λ = 365 *nm* for 10 *min*. The thin *pNIPAAm* layers (300 *nm*) on these substrates were prepared by spin-coating (4000 *rpm*, 60 *s*) from a 4 % w/v *pNIPAAm* ethanol solution onto the *PS* film (Scheme 3B). The samples were again dried at 50 °*C* in a vacuum oven for 12 *h*. The *pNIPAAm* layer was both crosslinked and attached to the *pNIPAAm* layer via *UV* irradiation at λ = 365 *nm*. The crosslinking density was varied by changing the crosslinking time from 5 *min* to 60 *min*, respectively. In the second method, the thicknesses of the polymer layers in the dry state were measured by a profilometer. Unless otherwise indicated, all *pNIPAAm* films were prepared by the first method.

Surface Plasmon Resonance (*SPR*) Experiments: *SPR* measurements were carried out in Kretschmann configuration with a customized setup described in chapter 3.1. The multilayer system in this paper consists of *LaSFN9* glass, chromium (d_{cr} , ε_{cr}), gold (d_{Au}, ε_{Au}), adhesion promoter (*AP*) (d_{AP}, ε_{AP}) or PS (d_{PS}, ε_{PS}), gel (d_{gel} , ε_{gel}) and solvent (water (ε_{H2O} = 1.77) or ethanol

(ε_{EtOH} = 1.85) or water-ethanol ($\varepsilon_{H2O\text{-}EtOH}$ = 1.77-1.85 composition-dependent)) where ε ($\varepsilon = \varepsilon` + i\,\varepsilon``$) and d are the dielectric constant and the thickness of the layers respectively. The substrate parameters (d_{cr}, ε_{cr}, d_{Au}, and ε_{Au}) were determined by a reference scan before the deposition of adhesion promoter or before the spin-coating of *PS*. After the deposition of the adhesion promoter or spin-coating of *PS*, another $I(\theta)$ scan was performed to determine either d_{AP} and ε_{AP} or d_{PS} and ε_{PS}, assuming that the other values (d_{cr} , ε_{cr}, d_{Au}, and ε_{Au}) were fixed. The third $I(\theta)$ scan was performed in air after the spin-coating and crosslinking of the gel layer to determine d_{gel} and ε_{gel} in the dry state. The common analysis method of the *SPR/OWS* data of thin organic layers from reflection scans assumes an average refractive index for the entire layer (referred here to as "box model"). The box model is accurate for homogeneous layers. Application of the reversed Wentzel-Kramers-Brillouin (*rWKB*) approximation to the optical data was used to characterize the refractive index gradient perpendicular to the swollen gel film in detail. The refractive index and thickness of the gel layers changed simultaneously during swelling and collapse. In order to determine thickness and refractive index independently by *SPR/OWS*, at least two optical modes were needed. Since waveguide modes cannot be guided within layers less than 500 *nm*, thicknesses in the range of 1-1.8 μm were chosen for most of the measurements in this study. When the hydrogel layer was swollen in ethanol, it was difficult to observe the waveguide modes especially for the crosslinking time less than 60 *min*.

SPR/OWS studies on both swelling and temperature-dependent behaviour of thin *pNIPAAm* gel layers were performed by placing the sample in a flow cell that was connected to a peristaltic pump and mounted on a hot stage. The stage was heated resistively and cooled with a water mantle surrounding the stage to adjust the temperature based on thermo couple Pt100 technology. Firstly, the $I(\theta)$ angle scan measurement of the gel in the dry state was carried out, and then the flow cell was filled with ethanol. The gel was left to swell for 30 *min* at 20 °*C* before another $I(\theta)$ angle scan was performed. This drying-swelling step was repeated 5 times before temperature dependent studies in mixtures of ethanol-water with different mixing ratios were undertaken. Through these drying-swelling cycles, the non-crosslinked polymer was dissolved and a stable thickness was achieved. Between each cycle, the samples were dried at 50 °*C* in a vacuum oven for one hour. For the temperature dependent studies, the temperature was increased in steps of 2 to 10 °*C*. After each temperature increase, the gel was left to swell for 10 *min* in order to reach thermal equilibrium.

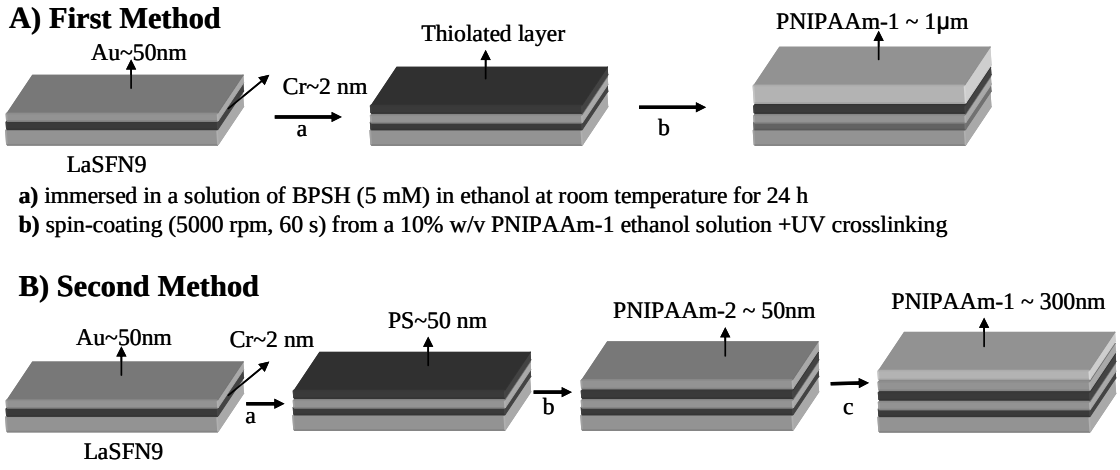

Scheme 6.3: Schematic representation of sample preparation for *SPR* measurements [1].

References

[1] Anac, I., Aulasevich, A., Junk, M. J. N., Jakubowicz, P., Roskamp, R. F., Menges, B., Jonas, U., Knoll, W., *Macromolecular Chemistry and Physics*, **2010**, 211 (9), 1018-1025

[2] Hirotsu, S., *J. Chem. Phys.* **1988**, *88*, 427.

[3] Zhang, G., Wu, C., *J. Am. Chem. Soc.* **2001**, *123*, 1376.

[4] Schild, H. G. , Muthukumar, M., Tirrell, D. A., *Macromolecules* **1991**, *24*, 948.

[5] Crowther, H. M., Vincent, B., *Colloid. Polym. Sci.* **1998**, *276*, 46.

[6] Tao, C. T., Young, T. H., *Polymer* **2005**, *46*, 10077.

[7] Moerkerke, R., Koningsveld, R., Nies, E., Berghmans, H., Dusek, K., Solc, K., "Phase Transitions in Swollen Networks: Swelling in a Single Solvent and in Solvent Mixtures", in *Chemical and Physical Networks, Formation and Control of Properties*, John Wiley & Sons, 1998, p. 463.

[8] Zhu, P. W., Napper, D. H., *J. Colloid Interface Sci.* **1996**, *177*, 343.

[9] Knoll, W., *Annu. Rev. Phys. Chem.* **1998**, *49*, 569.

[10] Prucker, O., Christian, S., Bock, H., Ruhe, J., Frank, C.W., Knoll, W., *Macromol. Chem. Physic.* **1998**, *199*, 1435.

[11] Beines, P. W. , Klosterkamp, I., Menges, B., Jonas, U., Knoll, W., *Langmuir* **2007**, *23*, 2231.

[12] Kuckling, D., Harmon, M. E., Frank, C. W., *Macromolecules* **2002**, *35*, 6377.

[13] Toomey, R., Freidank, D., Ruhe, J., *Macromolecules* **2004**, *37*, 882.

[14] Gianneli, M., Beines, P. W., Roskamp, R. F., Koynov, K., Fytas, G., Knoll, W. , *J. Phys. Chem. C* **2007**, *111*, 13205.

[15] Fried, J. R., "*Polymer Science and Technology"*, Prentice Hall, New Jersey, 2003.

[16] Yagi, Y., Inomata, H., Saito, S., *Macromolecules* **1992**, *25*, 2997.

[17] Harmon, M. E., Kuckling, D., Frank, C. W., *Macromolecules* **2003**, *36*, 162.

[18] Winnik, F. M., *Macromolecules* **1990**, *23*, 233.

[19] Prucker, O., Naumann, C. A., Ruhe, J., Knoll, W., Frank, C. W., *J. Am. Chem. Soc.* **1999**, *121*, 8766.

[20] Bilokin, Y. V., Melman, A., Niddam, V., Benhamu, B., Bachi, M. D, *Tetrahedron* **2000**, *56*, 3425.

7 Effect of Film Thickness

In this chapter temperature responsive *pNIPAAm* with dry film thickness < 100 *nm* were investigated to their volume transition temperature (T_C) and their volume degree of swelling (V_q). This project was done in cooperation with Christoph Hoffmann who performed the measurements and Catrin Corten who provided the materials.

7.1 Introduction

Thin functional hydrogel films < 100 *nm* are used as a hydrophilic "cushion" between the artificial membrane and the solid substrate [1,2]. The properties of thin hydrogel films differ from the bulk behaviour, e.g. the transition temperature and the refractive index of photo-cross-linked poly(N-isopropylacrylamide) (*pNIPPAm*) film in the collapsed state depend on the film thickness [3,4]. The volume-phase transition temperature and swelling ratio of the films fell into two overlapping regimes separated by at least one critical thickness. In the thick-film regime, greater than 100-760 *nm*, depending on the cross-linking density, comonomer concentration, and reference state, the films exhibited two transition temperatures. This can be explained by the stress imposed on the hydrogel as it swells perpendicular to the substrate. In the thin-film regime, less than 270 – 440 *nm*, depending on cross-linking density, the presence of a fixed substrate also limited the collapse of the gel at temperatures above the volume-phase transition temperature [4,5]. This critical film thickness was studied with *SPR/OWS* and analysis is limited by the penetration depth of surface plasmon resonance (~ 200 *nm*) and minimum film thickness to excite waveguide modes (~λ/2) in the hydrogel film. *SPR/OWS* cannot be used for films thinner than 100 *nm* [7]. With a grating coupler based waveguide sensor in Waveguide Mode Spectroscopy configuration (*WaMS*, see Chapter 3.2) it is possible to study hydrogel films with dry thickness < 100 *nm*. Therefore, very thin planar waveguides of high refractive index with TE_0 and TM_0 modes are used. By preparing a thin hydrogel film on the surface of the waveguide the refractive index of the surrounding medium changes in the penetration depth of the evanescent field of the waveguide modes. In this chapter temperature responsive *pNIPAAm* with dry thickness less than 100 *nm* were investigated to their phase transition temperature T_C and their volume degree of swelling V_q. Changes in the phase transition temperature and the volume degree of swelling were

observed by changing the amount of photo-cross-linking unit N,N-dimethylacrylamide (*DMIAAm*).

7.2 Results and Discussion

7.2.1 Influence of Layer Thickness to Swelling Ratio and Transition Temperature T_c.

The influence of hydrogel film thickness to the swelling behaviour and phase transition temperature of photo-cross-linked temperature responsive *pNIPAAm* was investigated by *WaMS*. The refractive index and film thickness were measured simultaneously using two waveguide modes. The refractive index and film thickness can be used to calculate the swelling ratio and polymer volume fraction of the hydrogel layers. These parameters can be compared to the change in the degree of swelling eq. 2.51 [7].

In Fig. 7.1 the typical sigmoid behaviour of phase transition process is detected as observed in thicker layers. Obviously the *WaMS* configuration allows studying very thin hydrogel films very accurately. Subsequently, in the temperature-dependent measurements, the refractive index and layer thickness were carried out from the received effective refractive index n_{eff} for both polarizations by using dispersion relations (see chapter 2). The suspected trend is reinforced by the volume transition temperature. The transition temperature T_c increased for thinner film.

Moreover it shows clearly that the thin layers are no longer able to collapse completely, leading to relatively flat swelling curves. The results already known in the literature [3,6] can be confirmed. However, it can clearly be seen that the 20 *nm* layer shows a lower volume swelling. Besides the water content in the collapsed state is greater than the 30 *nm* thick film. The substrate also prevents the full diffusion in and out of the gel. Therefore, thin layers have a slightly higher refractive index and a slightly higher critical temperature. However, by decreasing the film thickness *Tc* shifted toward higher temperatures, which is attributed to the confinement effect to the substrate. This effect also caused a highly anisotropic gel swelling. Lateral swelling amounted to only a few percent of the swelling perpendicular to the surface [3]. Thin layer are dominated by interactions with the substrate.

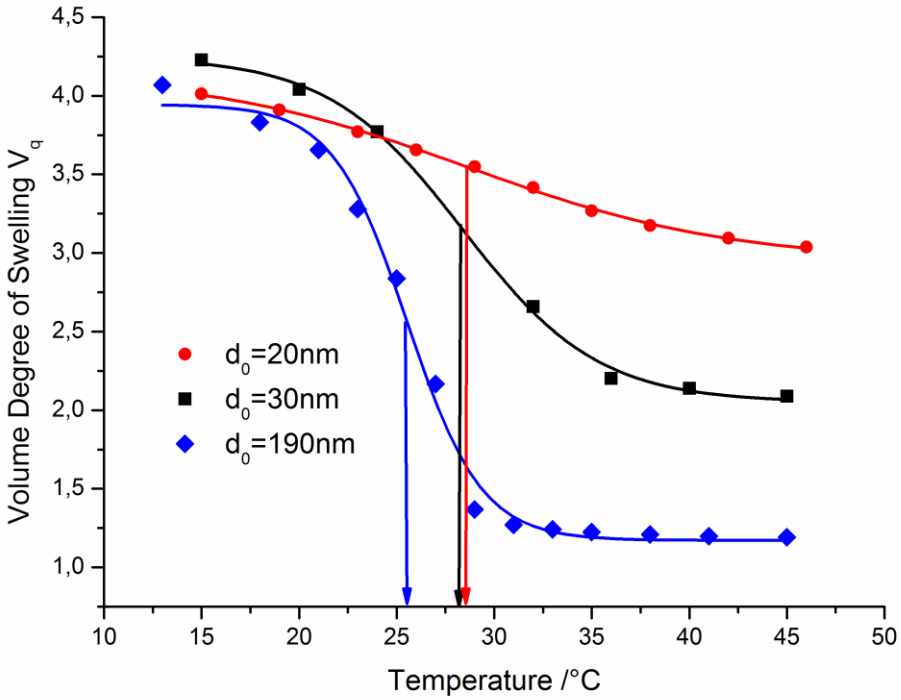

Figure 7.1: Volume degree of swelling and transition temperature for different dry film thicknesses of *pNIPAAm-co DMAAm5* (5%).

7.2.2 Influence of Cross-linking Density

WaMS was used to study the influence of cross-linking density to the swelling behaviour and phase transition temperature of photo-cross-linked temperature responsive *pNIPAAm* thin layers (30 *nm*). The refractive index and thickness were measured simultaneously using two waveguide modes. The volume degree of swelling was observed as a function of the temperature. In Fig. 7.2 the volume degree of swelling is shown for different contents of N,N-dimethylacrylamide *DMIAAM* as the photo-cross-linkable component. Clearly the influence of the photo-cross linking on the transition temperature is detected. The transition temperature decreases with increased photo-cross-linking content, as the *DMIAAm* chromophores make the network more hydrophobic in good agreement with thicker film (> 500 *nm*) [7]. However, the absolute transition temperature is slightly higher for thin films because of confinement effects to the substrate see section 7.2.1. The volume degree of swelling is affected by photo-cross-linking as well.

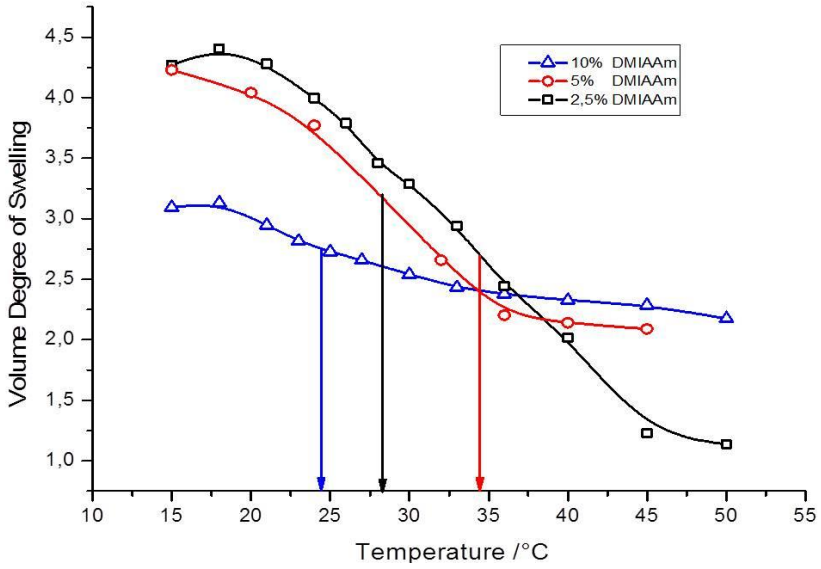

Figure 7.2: Volume degree of swelling calculated from *WaMS* measurements on hydrogel films with dry thickness of 30 *nm*. The swelling ratio changes as a function of the temperature for *pNIPAAm* hydrogel layers with different degrees of cross-linking.

Anisotropic Swelling behaviour

By using a multimode waveguide with two *TE* und two *TM* polarized waveguide modes it was possible to measure *d*, *n*, or the degree of volume swelling separately for both polarizations.

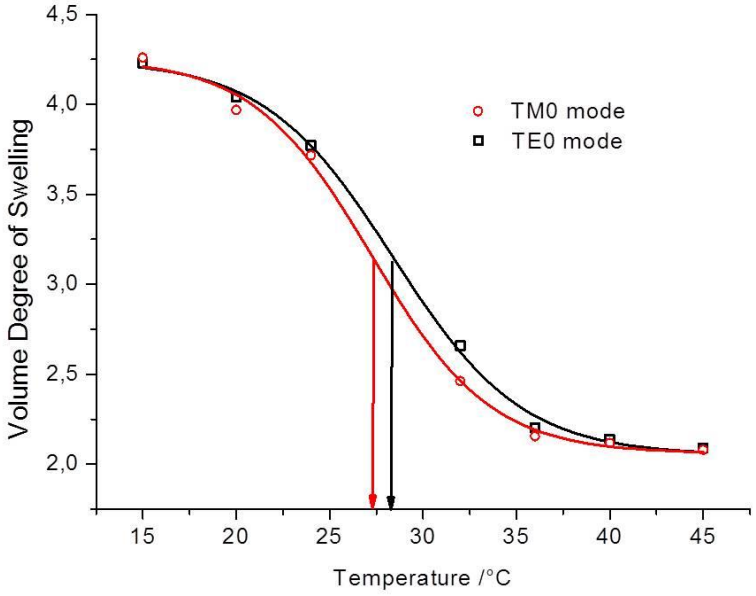

Figure 7.3: Anisotropic measurement of volume transition of *pNIPAAm* film

In Fig.7.3 the volume degree of swelling is shown for different polarizations of light. The different behaviour of the *TE* and *TM* polarization in terms of the transition temperature is clear. This behaviour indicates an inhomogeneous collapse or sources of the layer. In the fully swollen and collapsed state, however, the layer shows a homogeneous behaviour.

7.3 Conclusions

In this chapter temperature responsive poly(*NIPAAm*) with dry thickness less than 100 *nm* were investigated to their volume transition temperature (T_C) and their volume degree of swelling (*Vq*). Changes in the phase transition temperature and the volume degree of swelling were observed by changing the amount of N,N-dimethylacrylamide (*DMIAAm)* (photo-cross-linking unit). The volume transition temperature (T_C) is increasing with decreasing content of *DMIAAm*. For thinner layers the phase transition temperatures T_C increased. The thin layers cannot fully collapse anymore because of confinement effects to the substrate.

7.4 Experimental Part

Materials

N-Isopropylacrylamide (*NIPAAm*; Aldrich) was purified by recrystallization from hexane and dried in vacuum and N,N-dimethylacrylamide [9]. (*DMAAm*; Aldrich) was prepared according to the literature [8].

Synthesis of the polymer

Synthesis of the Copolymer. The *pNIPAAm* copolymers were obtained by free radical polymerization of *NIPAAm*, *DMAAm*, and *DMIAAm*, initiated with *AIBN* in dioxane. The total monomer concentration was 0.55 *mol/l*, and the reaction was carried out at 70 *°C* under nitrogen for 7 *h.* The polymer was precipitated in diethyl ether and purified by reprecipitation from *THF* into diethyl ether (1/3) [3].

Sample preparation

The glass substrate was cleaned with ethanol (96%) and dried with nitrogen. On the *SPR/OWS* substrate a thin chrome (~2 *nm*) and gold layer (~50 *mn*) was coated with a high vacuum evaporation system (Edwards, model car 306) at a pressure < $5x10^{-6}$*mbar*.

Before the hydrogel layer is spincoated, it is necessary to prepare an adhesion promoter on the tantalpentoxide Ta_2O_5- waveguide sensor. In Fig. 7.4 the adhesion promoter is shown.

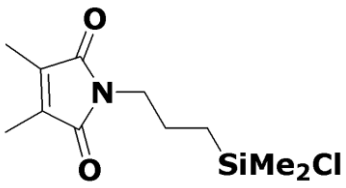

Fig. 7.4: Adhesion promoter for oxide surfaces [9].

Oxide surfaces first must be activated. Therefore, Ta_2O_5- waveguides are exposed to a plasma treatment (plasma cleaner, Technics plasma GmbH, 200-G; 0.1 *mbar* O_2; 0. 9 *mbar* Ar; 300 *W*) for five minutes. Then they are immediately treated with a solution of a bonding agent in Bicyclohexyl for 24 *h* with a 0.1 *vol* %. The oxide surfaces are rinsed with ethanol and dried with an argon flow. The respective adhesion promoter is shown in Figure 7.4.

The hydrogel films were prepared by spin-coating (Headway Research Inc.) on Ta_2O_5 waveguide sensors. Resulting thickness depends on various parameters, such as weight concentration of the polymer, used solvents, the rotation speed and time. According to the spin-coating to dry process the samples for 20 minutes at room temperature in the vacuum to remove remaining solvent residues. Both crosslinking and surface attachment were carried out in a single process step by irradiating the sample with *UV* light (λ = 365 *nm*) for 30 min (Stratalinker 2400, Stratagene).

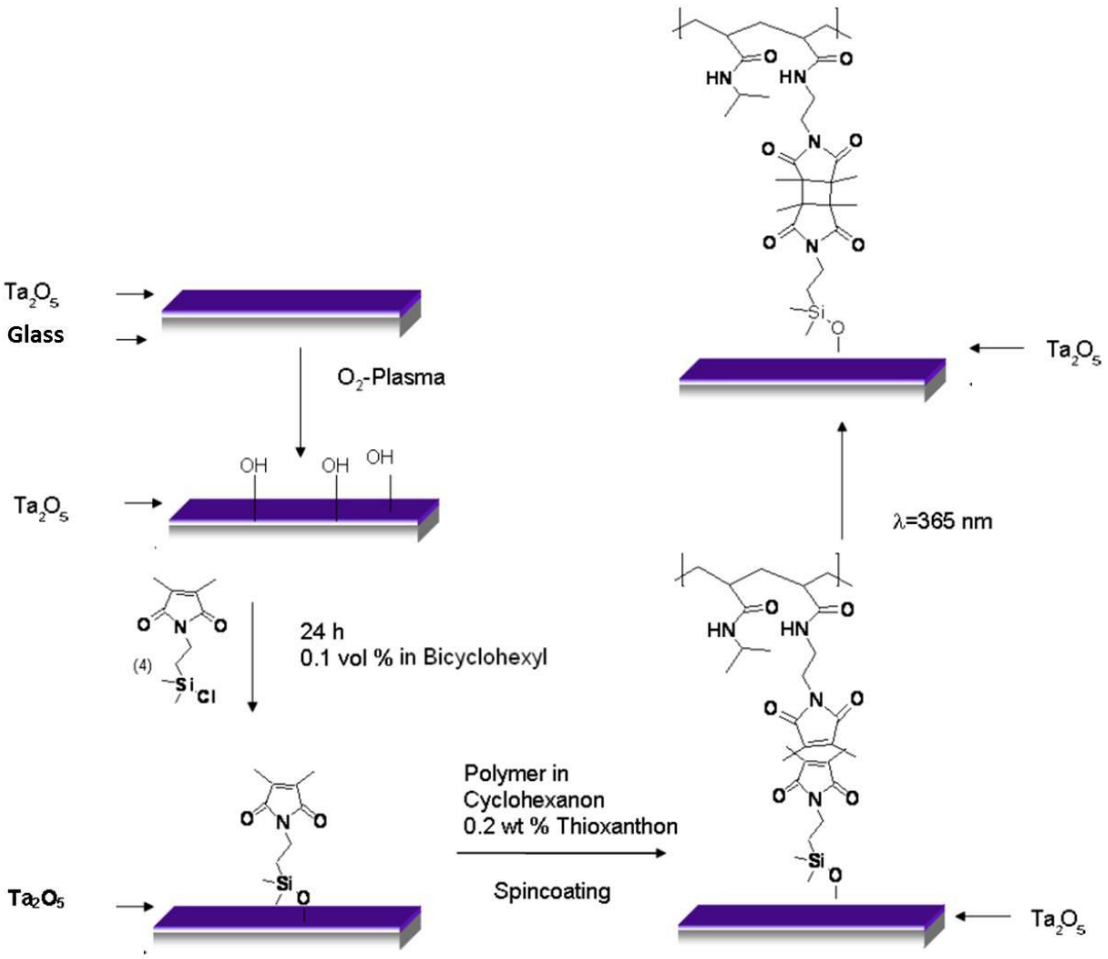

Figure 7.5: Scheme of preparation [9].

Waveguide mode spectroscopy (*WaMS*) experiments

WaMS measurements were carried out in grating coupler configuration with a customized setup described in chapter 3.2.

.

References

[1] Kibrom, A., Roskamp, R.F., Jonas, U., Menges, B., Knoll, W., Naumann, R. L.C., *Soft Matter*, 2011, 7, 1, 237-246.

[2] Smith, H.L., Jablin, M.S., Vidyasagar, A., Saiz, J., Watkins, E., Toomey, R., Hurd, A.J., and Majewski, J., Physical Review Letters, 2009, 102(22), 228102-1-4.

[3] Kuckling, D., Harmon, M.E. and Frank, C.W., *Macromolecules*, **2002**, 35, (16), 6377-6383.

[4] Harmon, M.E., Kuckling, D. and Frank, C.W., *Macromolecules*, **2003**, 162-172.

[5] Harmon, M.E., Kuckling, D., Pareek, P., and Frank, C.W., *Langmuir*, **2003**, 9, 10947-19956.

[6] Harmon, M.E., Jakob, T.A.M., Knoll, W. and Frank, C.W., *Macromolecules*, **2002**, 35, 5999-6004.

[7] Harmon, M.E., Kuckling, D., and Frank, C.W., *Langmuir*, **2003**, 19, 10660-10665.

[8] Ling, L., Habicher, W. D., Kuckling, D., Adler, H.J., *Design Monom. Polym.*, **1999**, 4, 351-358.

[9] Corten Catrin, Diss. 2008, TU Dresden, Synthese und Charakterisierung dünner Hydrogelschichten mit modulierbaren Eigenschaften.

8 Protein-Functionalized Hydrogel Films

In this chapter the optical waveguide modes spectroscopy (*OWS*) is implemented for a time-resolved quantitative studies of protein-functionalized hydrogel films. This project was carried out in cooperation with Alena Aulasevich who performed the measurements, Robert Roskamp who provided the hydrogel, Jakub Dostalek, Ulrich Jonas and Wolfgang Knoll and has already been published [1].

8.1 Introduction

Hydrogel materials can be modified with protein biomolecules in order to provide specific functionality such as controlled drug release [2], defined interactions with cells [3], or capture of target analyte molecules [4,5]. For the observation of thin hydrogel films, various optical methods have been used, which include surface plasmon resonance (*SPR*) and optical waveguide mode spectroscopy (*OWS*) [6,7], applied for the study of structural and swelling characteristics, fluorescence correlation spectroscopy (*FCS*) and dynamic light scattering (*DLS*), for the investigation of their dynamics [8,9]. In this chapter the implementation of *OWS* for quantitative time-resolved characterization of mass changes and the swelling behaviour of protein-functionalized N-isopropylacrylamide (*NIPAAm*)-based hydrogel films is reported. This thermal responsive gel can be used for the design of advanced biosensor binding matrices. For instance, the hydrogel film can be swollen in an aqueous sample (e.g. blood) in order to capture a target analyte from the sample by a ligand immobilized at the hydrogel polymer backbone. Upon externally triggered gel collapse (e.g. by a temperature increase [6]), excess liquid and unbound species would be expelled from the hydrogel matrix while the specifically bound analyte would be concentrated at to the polymer matrix at the sensor surface and thus allow for its effective detection. Immunoglobulin G (*IgG*) molecules were in situ covalently coupled into the *NIPAAm*-based gel by using a novel charge-attraction scheme based on a tetrafluorophenol sulfonate active ester. Compared to other methods [4,10], this approach provided stable covalent coupling of *IgG* molecules without exposing the protein to harsh conditions. The anti-fouling properties of the functionalized hydrogel network were investigated and its potential to serve as a binding matrix

was demonstrated in an experiment in which the kinetics of the affinity binding of neutravidin (*NA*) molecules to the immobilized biotinylated *IgG* was monitored.

8.2 Results and Discussion

8.2.1 Swelling of the Gel

Firstly, the hydrogel film was swollen in an acetate buffer *ACT* for 45 *min* after which a stable optical response was observed. By fitting the measured angular reflectivity spectrum (*I*) presented in Figure 8.1(A), the thickness and the refractive index of the hydrogel film were found to be d_h = 2.5 μm and n_h = 1.3467, respectively. These parameters corresponded to the surface mass density of the hydrogel film of $\Gamma = 171\ ng/mm^2$. The stability of the swollen gel was tested by incubation in *ACT* buffer for several hours and a subsequent flow of *ACT* and *PBS* buffers with a *pH* of 4 and 7.4. No significant changes in its optical properties were observed.

8.2.2 Modification with IgG

The carboxylic groups in the swollen gel were activated by 90 *min* incubation in a solution with sodium para-tetrafluorophenol sulfonate (*TFPS*) and 1-Ethyl-3-(3-dimethylaminopropyl) carbodiimide (*EDC*) dissolved in water at a concentration of 21 and 75 *mg/ml*, respectively. Afterwards, the surface was rinsed with *ACT* buffer for 3 *min* and the solution with *IgGb* (concentration of 100 *mg/ml*) was pumped through the cell for 75 *min*. The *IgG-b* molecules were dissolved in *ACT* buffer at *pH* 4, which was below their isoelectric point (*Ip* ≈ 5.5). Therefore, the positive charge of these molecules allowed for their Coulomb attraction into the hydrogel network that exhibited a net negative excess charge as a result of the sulfonic moieties and the chosen *pH*. After the uptake of *IgG-b* molecules and their reaction with the activated carboxylic groups, the gel was rinsed with the *ACT* buffer for 10 *min*, incubated in ethanolamine for 10 *min* in order to block the unreacted active ester sites and washed with *ACT* buffer for 15 *min*. As seen in Figure 10.1(a), the binding of *IgG-b* into the gel was manifested as a shift of the resonant dips associated with the excitation of TM_1 and TM_2 modes. The fitting of

spectrum II, measured after the uptake of *IgG-b* molecules, revealed that the loading of the gel with *IgG-b* induced a decrease in its thickness to $d_h = 1.94\ \mu m$ and an increase in its surface mass density to $\Gamma = 407\ ng/mm^2$. The thickness decrease was probably a result of the screening of the negatively charged gel moieties by the positively charged *IgG-b* and the 2.4 fold increase in the surface mass density was caused by the uptake of *IgG-b* molecules. After the incubation in ethanolamine, the resonances shifted to lower angles as the loosely bound *IgG-b* molecules were rinsed out of the gel (see spectrum III). This led to a decrease in the gel surface mass density to 190 ng/mm^2 and an increase of the thickness to $d_h = 3.2\ \mu m$. The thickness increase can be attributed to electrostatic repulsion within the gel between bound *IgG-b* molecules that are positively charged at *pH* 4 (note that the negatively charged carboxylic groups without *IgG* substituents were converted into neutral hydroxyl groups through their reaction with *EDC-TFPS* and ethanolamine). The surface mass density of the covalently immobilized *IgG-b* molecules of $\Delta\Gamma = 19\ ng/mm^2$ was determined as the difference between the surface mass density Γ before the hydrogel activation and after the incubation in ethanolamine. The changes in the swelling and the surface mass density of the hydrogel are summarized in Table 8.2. The thickness and mass density of the hydrogel and immobilized *IgG-b* was determined for a set of three identical samples as $d_h = 2.32 \pm 0.28\ \mu m$, $\Gamma = 168 \pm 11\ ng/mm^2$, and $\Delta\Gamma = 31 \pm 10\ ng/mm^2$, respectively (± denotes the standard deviation). After modifying the hydrogel with *IgG-b* antibodies, the hydrogel was swollen in *PBS* at *pH* 7.4. As spectrum IV in Figure 8.1b shows, after the swelling in *PBS* the refractive index increased to $n_h = 1.35$ and the thickness decreased to $d_h = 2.38\ \mu m$, which can be attributed to reduced repulsion force within the hydrogel because of a higher ionic strength of *PBS*.

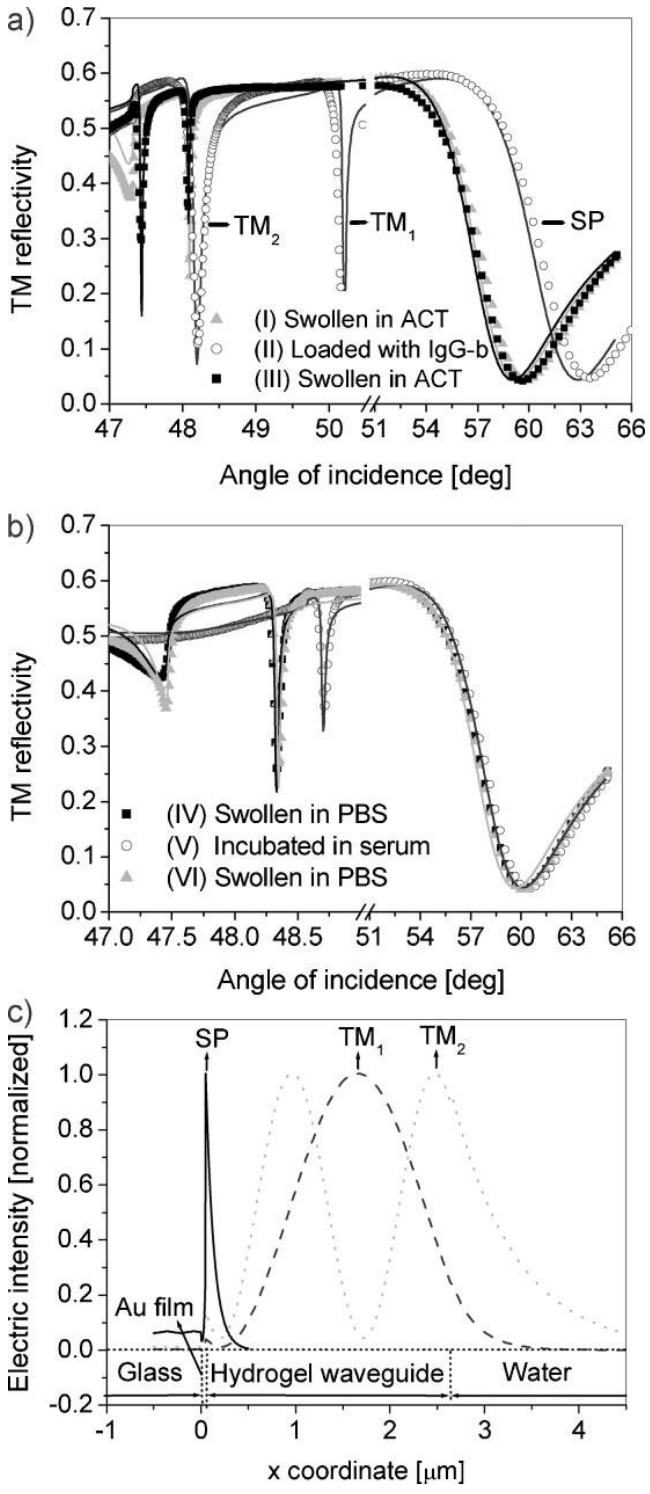

Figure 8.1: a) Reflectivity spectra measured for the hydrogel film swollen in *ACT* buffer (squares), loaded with *IgG* molecules (circles) and after the incubation in ethanolamine (triangles). b) Reflectivity spectra for the gel swollen in *PBS* (squares), upon the incubation on blood plasma (circles) and after the washout with *PBS* (triangles). Corresponding fits are shown as lines. c) Simulations of the profile of the optical light intensity (layer parameters stated in Table 8.1) [1].

8.2.3 Anti-Fouling Properties

The non-specific sorption of blood plasma to the *IgG* modified *NIPAAm*-based film was investigated. Blood plasma (100 %) was circulated through the flow-cell for 40 *min* followed by rinsing with *PBS* buffer for 130 min. Fitting of the reflectivity spectrum (V) measured upon the incubation in plasma showed an increase in the gel refractive index to n_h = 1.3535, which indicated that plasma had diffused inside the hydrogel, see Figure 8.1(b). After the rinsing step, the surface mass density of nonspecifically bound plasma compounds was determined to be $\Delta\Gamma$ = 5 ng/mm^2 as the difference in the surface mass density before the injection of plasma (spectrum IV) and after the rinsing (spectrum VI).

Table 8.1: Optical parameters of the layer structure used for the excitation of hydrogel waveguide modes [1].

Material	Refractive index *n*, thickness *d*	
Glass substrate	n_p=1.845	
Chromium layer	n =3.14 -3.32,	d=2 nm
Gold layer	n_m=0.34 -3.5i,	d_m=45 nm
Linker layer	n =1.5,	d=1.37 nm
Hydrogel	n_h=1.3467,	d_h=2.50 μm
Liquid buffer	n_b=1.3330	

8.2.4 Affinity Binding

The functionalized hydrogel can be used as a matrix for affinity binding studies. Figure 8.2(a) shows the time evolution of the angular position of the TM_1 resonant dip upon the binding of *NA* to the hydrogel film with immobilized biotinylated *IgG-b* molecules. Firstly, *PBS* was flowed across the gel for 5 *min* in order to establish a stable baseline. Afterwards, a solution with *NA* dissolved in *PBS* at a concentration of 100 *mg/ml* was flowed for 50 *min*, followed by rinsing with *PBS*. As seen in Figure 8.2(a), the binding of *NA* into the gel network with biotin moieties was observed as a gradual increase of the coupling angle, which reached its saturation after approximately 40 *min*. In the control experiment, we observed no binding of *NA* in the gel that

was modified by *IgG* molecules without biotin tags. Diffusion characteristics and association and dissociation binding constants of the reaction can be determined by fitting the measured kinetics with an appropriate model [12]. The fitted *NA* association rate (~10^3 M^{-1} s^{-1}) was two orders of magnitude lower than that for the interaction between (strept) avidin derivatives and biotin (~10^5 M^{-1} s^{-1} [13]), which indicated that the binding in the hydrogel was strongly diffusion controlled. The analysis of angular spectra (VI–VII) in Figure 3(B) revealed an increase in the surface mass density as a result of the capture of *NA* to biotin moieties of 16 *ng/mm*^{2} (the mass density of immobilized *IgG-b* was *11 ng/mm*^{2}). Assuming the molecular weight of *IgG* (M_W = 150 *kDa*) is 2.5-fold higher than that of *NA* (M_W = 60 *kDa*), the average number of *NA* molecules captured by an *IgG-b* molecule was determined. This ratio was measured in triplicate as 4.6 ± 1.1 (standard deviation), which was within the expected range (3–6 biotin tags were anchored to an individual *IgG* molecule) and indicated that the coupling of *IgG-b* molecules to flexible polymer chains in a swollen hydrogel network allowed for efficient binding of the affinity partner molecules.

Table 8.2: Characteristics of the hydrogel film upon its modification with protein molecules [1].

Hydrogel	n_b	d_h	n_h	Γ
		µm		*ng mm*$^{-2}$
(I) Swollen in ACT	1.3330	2.50	1.3467	171
(II) Loaded with IgG-b	1.3330	1.94	1.3757	407
(III) After passivation	1.3330	3.20	1.3449	190
(IV) Swollen in PBS	1.3347	2.38	1.3500	182
(V) Incubated in plasma	1.3480	2.20	1.3535	–
(VI) Swollen in PBS	1.3347	2.44	1.3500	187
(VII) After NA binding	1.3347	2.53	1.3507	203

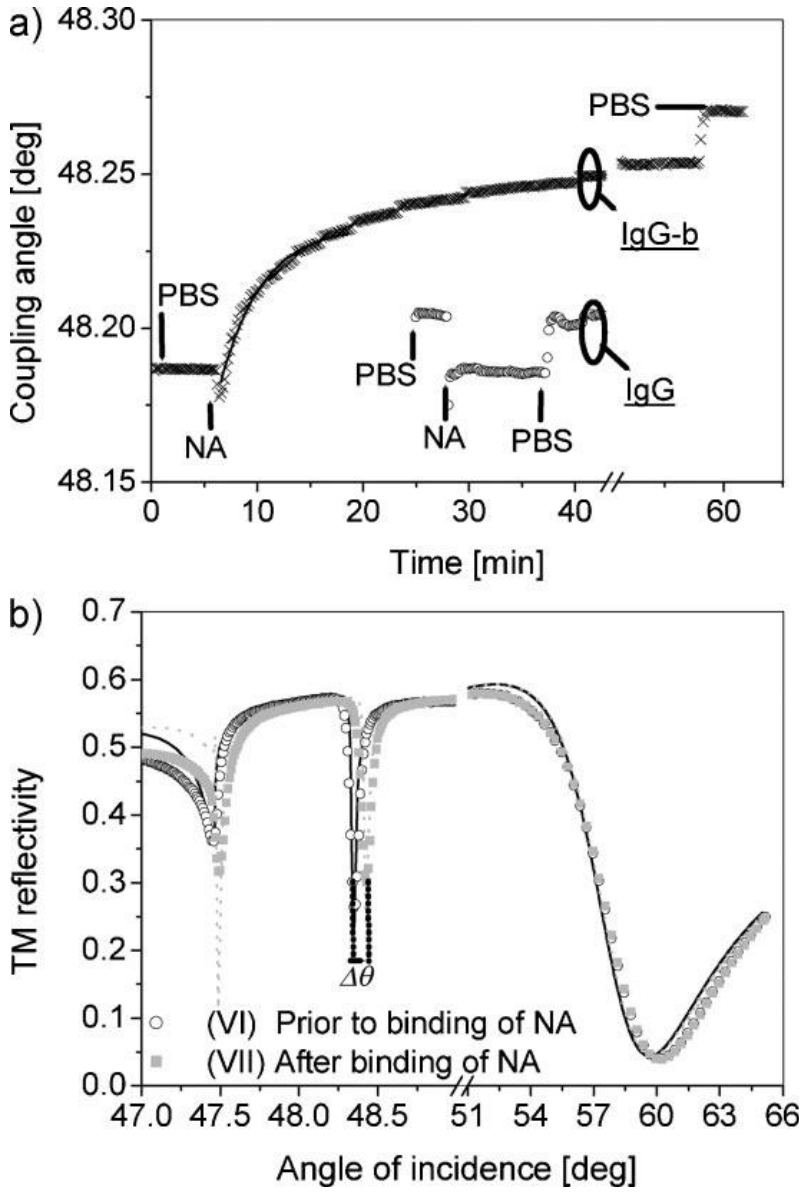

Figure 8.2: a) Time evolution of the TM_1 coupling angle showing the binding of *NA* to a gel modified with *IgG-b* and *IgG*. b) Measured reflectivity spectra before (circles) and after (squares) the affinity binding of *NA* with corresponding fits (lines) [1].

8.3 Conclusions

Optical waveguide modes spectroscopy (*OWS*) was implemented for the time-resolved quantitative studies of protein-functionalized hydrogel films. This technique allowed the observation of changes in mass distribution in a gel film through the simultaneous measurement

of its thickness and refractive index. *OWS* was applied for the investigation of the coupling of protein molecules to a *NIPAAm*-based hydrogel film, which was achieved by using a novel charge-attraction scheme that exploited tetrafluorophenol-sulfonate active ester chemistry. The hydrogel can be used as a binding matrix into which protein molecules can diffuse and affinity bind to the immobilized catcher molecules. In addition, the investigation of the non-specific binding of blood plasma to the gel film revealed its good anti-fouling properties, which makes it, for instance, a good candidate for future applications in affinity biosensors.

8.4 Experimental Part

Chemicals

Sodium acetate, acetic acid and ethanolamine hydrochloride were purchased from Aldrich (USA). 1-Ethyl-3-(3-dimethylaminopropyl) carbodiimide (*EDC*) was bought from Pierce (USA). Biotin-labeled immunoglobulin antibody (*IgG-b*) was obtained from Acros (Germany). Immunoglobulin antibody without biotin labels (*IgG*) was ordered from Biodesign (USA). Neutravidin (*NA*) and newborn calf serum were purchased from Invitrogen GmbH (Germany). Phosphate buffered saline (*PBS*, 10^{-2} *M* phosphate, 137 x10^{-3} *M NaCl*, 2.7x10^{-3} *M KCl* with 0.005% surfactant P-20), *pH* 7.4, was obtained from CalBiochem (USA) and 10^{-2} *M* acetate buffer (ACT), *pH* 4, was prepared in house. Ethanolamine was dissolved in water at 1 *M* concentration with the *pH* of the solution being adjusted to 8.5 with sodium hydroxide. Sodium para-tetrafluorophenol sulfonate (*TFPS*) was synthesized as described in the literature [11].

Preparation and Modification of Hydrogel Films

The synthesis of the *NIPAAm*-based hydrogel composed of the terpolymer with N-isopropylacrylamide, methacrylic acid, and 4-methacryloyl benzophenone was performed as described elsewhere [6]. A thin hydrogel film was deposited on a gold surface modified by a benzophenone-terminated thiol layer by spincoating from ethanol solution (4 wt.-% of the polymer) and dried overnight in vacuum at 50 °*C*. The polymer chains were crosslinked and anchored to the gold surface through benzophenone units by *UV* irradiation ($\lambda = 365$ *nm*,

irradiation energy density of 2 $J\ cm^{-2}$). The thickness of the dry crosslinked polymer layer was 300 *nm* measured with a surface profiler.

Data Evaluation

The measured angular reflectivity spectra were fitted by using a transfer matrix-based model in order to determine the optical properties. Furthermore, we assumed the dependence of the refractive index *n(x)* on the distance from the gold sensor surface as:

$$n(x) = n_b + (n_h - n_b)H(d_h - x) \tag{10.1}$$

where x is the axis perpendicular to the sensor surface (x = 0 is located at the interface between the gold and hydrogel) and H is the Heaviside step function. The parameters of the layer structure used for the excitation of two waveguide modes in the hydrogel (noted as TM_1 and TM_2) and surface plasmon resonance *SPR* are stated in Table 8.1 and the profile of their electric light intensity field is shown in Figure 8.1(c). By fitting the angular positions of TM_1 and TM_2 resonances measured with the accuracy of 10 *mdeg*, the thickness and the refractive index of the hydrogel film was determined with the error of $\delta d_h \approx 20\ nm$ and $\delta n_h = 10^{-4}$, respectively. In a further analysis we assumed that the refractive index changes with the concentration of proteins and the *NIPAAm* polymer as $\delta n_h/\delta c = 0.2\ \mu l\ mg^{-1}$. The surface mass density Γ of the hydrogel film including immobilized protein was calculated as:

$$\Gamma = (n_h - n_b)d_h \frac{\partial c}{\partial n_h} \tag{10.2}$$

References

[1] Aulasevich, A; Roskamp, R.F.; Jonas, U.; Loppinet, B.; Fytas, G. and Knoll, W., Macromolecular Rapid Communications 2009, 30(9), 872-877.

[2] McGonigle, J. S.; Tae, G.; Stayton, P. S.; Hoffman, A. S.; Scatena, M., J. Biomater. Sci., Polym. Ed. 2008, 19, 1021.

[3] Rowley, J. A.; Madlambayan, G.; Mooney, D. J., Biomaterials 1999, 20, 45.

[4] Miyata, T.; Asami, N.; Uragami, T., Nature 1999, 399, 766.

[5] Knoll, W.; Kasry, A.; Yu, F.; Wang, Y.; Brunsen, A.; Dostalek, J., J. Nonlinear Optic. Phys. Mater. 2008, 17, 121.

[6] Beines, P. W.; Klosterkamp, I.; Menges, B.; Jonas, U. and Knoll, W., Langmuir 2007, 23, 2231.

[7] Dostalek, J.; Roskamp, R. F. and Knoll, W., Sens. Actuators B 2008, in press (doi 10.1016/j.snb.2008.07.002).

[8] Gianneli, M.; Beines, P. W.; Roskamp, R. F.; Koynov, K.; Fytas, G. and Knoll, W., J. Phys. Chem. C 2007, 111, 13205.

[9] Gianneli, M.; Roskamp, R. F.; Jonas, U.; Loppinet, B.; Fytas, G. and Knoll, W., Soft Matter 2008, 4, 1443.

[10] Derwinska, K.; Gheber, L. A.; Sauer, U.; Schorn, L. and Preininger, C., Langmuir 2007, 23, 10551.

[11] Gee, K. R.; Archer, E. A.; Kang, H. C., Tetrahedron Lett. 1999, 40,1471.

[12] Edwards, D. A.; Goldstein, B.; Cohen, D. S., J. Math. Biol. 1999, 39,533.

[13] Qureshi, M. H.; Yeung, J. C.; Wu, S. C.; Wong, S. L., J. Biol. Chem. 2001, 276, 46422.

9 Hydrogel-Supported Lipid Bilayer Membranes

The investigation of hydrogel supported protein-tethered bilayer lipid membranes (*ptBLM*) as a new approach toward polymer-supported lipid membranes was a cooperation with Asmorom Kibrom who performed the measurements, Robert F. Roskamp who provided the hydrogel, Ulrich Jonas, Wolfgang Knoll and Renate L. C. Naumann. More details can be found in the published paper [1]. The following chapter is focused on the optical anisotropic characterization of membrane formation process based on an *SPR/OWS* technique.

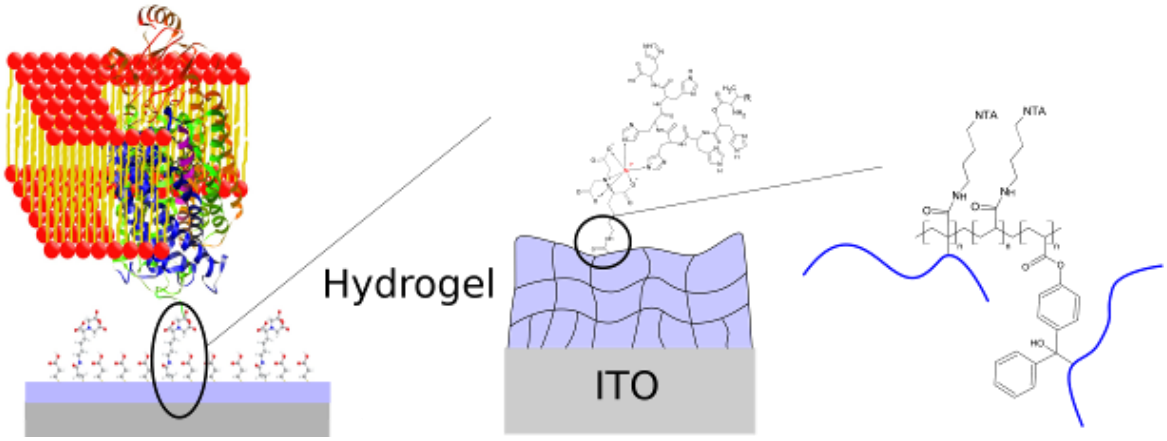

Fig. 9.1: Schematics of the protein-supported bilayer lipid membrane (*ptBLM*) bound to the top layer of a hydrogel. [1].

9.1 Introduction

The lipid bilayer membrane of living cells plays a prominent role in many biologically relevant processes. Examples are signal transduction, transport of ions and molecules, biosynthesis, cell adhesion and recognition. Consequently, there is a great interest in model systems that would allow for a systematic study of such processes, preferably on a planar substrate. The idea of using macromolecules as a “cushion” to mimic the cytosol/cytoskeleton of the cell to create a hydrophilic space between the lipid membrane and a solid support was first introduced by Ringsdorf and Sackmann [2,3]. Since then polymer-supported lipid membranes have been widely used, as documented in several major review articles [3,4]. Physical properties of the fluid lipid bilayer were investigated as well as processes taking place on the surface of the

membrane. However, a new approach in this direction is the use of a polymer layer as a substrate for the so-called protein-supported bilayer lipid membrane (*ptBLM*), previously developed on the basis of short linker molecules [5,6]. This approach employs the protein immobilized on the substrate as a scaffold for the membrane reconstituted around the protein (Fig.9.1). Consequently, this methodology begins with immobilizing the protein specifically onto the top layer of the polymer. This can be achieved by using a hydrogel as the polymer layer with mesh sizes smaller than the size of the protein. The hydrogel is provided with a binding motif such as a nitrilo-triacetic acid (*NTA*) functionality chelated with Ni^{+} ions designed to bind the protein via the his-tag technology [6,7]. Since the protein is too big to penetrate the gel, it stays on the surface. If a lipid bilayer is then assembled around the protein, the formation of an electrically isolating protein-lipid layer could be expected. Electron and ion transport processes through the cytochrome c oxidase (*CcO*) have been observed in previous studies [8,9,12]. In the present study a hydrogel consisting of poly(*N*-(2-hydroxyethyl)acrylamide-co-5-acrylamido-1-carboxypentyl-iminodi-acetate-co-4-benzoylphenyl methacrylate) (P(HEAAm-co-NTAAAm-co-MABP)) was prepared by polymer analogous reactions that offer an *NTA* moiety to bind the *CcO* (Fig. 9.1). Optically transparent indium-tin oxide (*ITO*) layers were used as conducting substrates, different from previous studies using metal films [10,13]. The advantage of *ITO* is that it allows the application of a number of optical surface-analytical techniques such as surface plasmon resonance and optical waveguide spectroscopy (*SPR/OWS*) and fluorescence techniques not applicable on metal films.

9.2 Results and Discussion

Hydrogel-Supported *ptBLMs* on *ITO* layer

The *ITO* surface was coated with a layer of the copolymer as described in the experimental part. The hydrogel was obtained as a highly crosslinked layer from *P(PFPA-co-MABP)* in three reaction steps as depicted in Fig.9.5. The precursor copolymer *P(PFPA-co-MABP)* was prepared by free radical polymerization from 98 mol% *PFPA* and 2 mol% *MABP*, for details see the experimental part. In the first step this precursor copolymer was spin-coated on a benzoylphenyl (*BP*)-silane functionalized *ITO* surface and *UV*-crosslinked. The thickness of the dry copolymer layer was 60 *nm* measured by atomic force microscopy

AFM and ellipsometry. Thereby, the surface of the *ITO* layer was flattened and a chemically durable surface was obtained with high density of the hydrophobic pentafluorophenol active ester. These functional groups exhibited a high reactivity towards amines and prevent the swelling by water during the coupling of amino-*NTA* in aqueous media in the second step. This resulted in an *NTA*-functionalization predominantly at the polymer-water interface. The subsequent reaction with ethanolamine transformed the hydrophobic copolymer into the hydrophilic hydrogel. Such a coating complied with the criteria mentioned in the introduction, namely providing a stable, smooth, hydrophilic and reactive surface. Stability and surface roughness were determined by molecular weight of the polymer and the extent of crosslinking (e. g. the amount of crosslinker groups and the crosslinking irradiation dose). The employed copolymer was optimized resulting in a durable coating of low roughness. *AFM* measurements showed the spikes of the *ITO* layer to be completely covered by the polymer layer. The coating had a low mean roughness (*rms* = 0.4 *nm*) and a peak-to-valley height of 4 *nm*, a highly important prerequisite for the assembly of a dense lipid membrane.

Oriented Immobilization of the CcO and Reconstitution into a ptBLM Investigated by SPR/OWS

Electrochemical impedance spectroscopy (*EIS*) is not designed to follow the binding of the *CcO* to the *NTA* functionalized polymer layer. The formation of the lipid bilayer can be deduced from these measurements but only indirectly. More information could be expected from *SPR/OWS* measurements, which were performed on a thick (680 *nm*) *ITO* layer as the waveguide sensor. Binding as well as lipid reconstitution could be clearly seen as a shift of the TM_3 (*p*-polarized) and the TE_2 mode (*s*-polarized) in the angle spectra in Fig.9.2. The effective refractive indices n_{eff} of the propagating TM_3 and TE_2 (Table 3) are calculated from the angle spectra using eq 2.39.

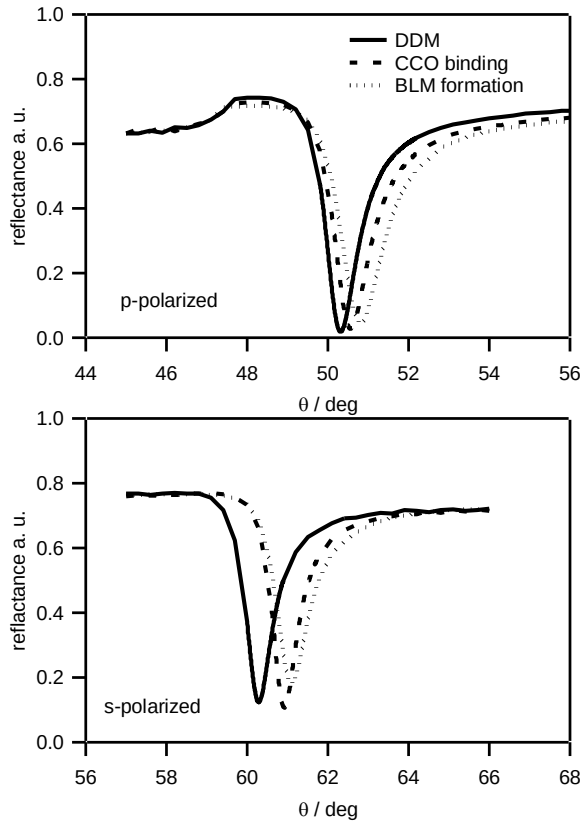

Figure 9.2: *SPR/OWS* angle spectra of (A) *p*-polarized and (B) *s*-polarized light (λ = 632.8 *nm*) of (solid line*)* Ni^{2+}*-NTA* modified *P(HEAAm-co-NTAAAm-co-MABP)* on *ITO* before and (dashed line) after binding of *CcO*; (dotted line) after in situ dialysis to form the lipid bilayer around the protein [1].

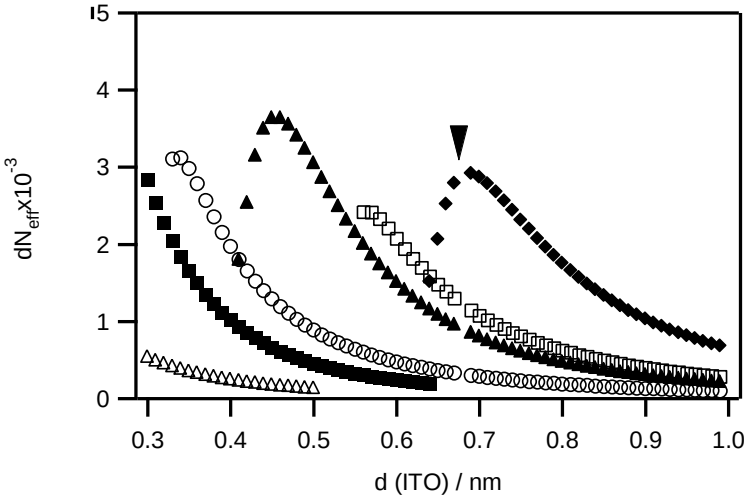

Figure 9.3: Simulated shifts of the effective refractive δn_{eff} caused by an isotropic adlayer (*n* = 1.47, d = 11 *nm*) calculated for *TE* and *TM* modes as a function of the thickness of the *ITO* layer (*n* = 1.9065): (■)TM_1 (▲)TM_2 (♦)TM_3, (Δ)TE_0 (○)TE_1 (□)TE_2. The arrow indicates the thickness of the *ITO* layer used in this study [1].

Changes of Δn_{eff} from one layer to the next yielded information about the anisotropy of the polymer layers. From the angle scans it was already obvious that the two modes shifted differently for each layer formation. In order to obtain more quantitative information - Δn_{eff} values of the two modes were simulated for an isotropic case as a function of the thickness of the *ITO* layer. The thickness of the *ITO* gel support was set to 60 *nm* (see experimental). From this so-called sensitivity curve (Fig. 9.3) the expected absolute shift Δn_{eff} of both modes, TM_3 and TE_2 at a particular thickness d of the *ITO* layer, can be derived. In the experiments performed (d_{ITO} = 680 *nm*) the two modes should shift at a ratio TM_3:TE_2 of 2.4:1 provided the layers are isotropic.

Table 9.1: The change of the effective refractive index n_{eff} of the TE_2 and TM_3 modes after each preparation step calculated using eq. 2.39 [1].

	Δn_{eff} TM_3	Δn_{eff} TE_2
Ni^{2+}-NTA modified P(HEAm-co-TAAm-co-MABP)	0	0
… after CcO adsorption	2.971×10^{-3}	6.432×10^{-3}
… after in-situ dialysis for formation of the BLM	5.875×10^{-3}	8.243×10^{-3}

The actual Δn_{eff} values derived from the n_{eff} in Table 9.1 showed different behaviours. Fig. 9.3 presents actual and simulated Δn_{eff} data of the protein and the protein/lipid layer. In both cases the two modes, TE_2 and TM_3, shifted at a ratio different from the theoretical one. The TE_2 mode shifted even stronger than the TM_3 mode in contrast to what was expected from the simulation data. This result could only be explained by refractive index anisotropy of both the *CcO* and the lipid/*CcO* layer. With the dipole moment directed along the *x*-axis of the *CcO*, a shift of the *TE* mode indicated the *CcO* molecules being arranged more parallel to the surface rather than perpendicular. They seemed to rearrange into a more upright position as deduced from the difference between *TE* and *TM* modes decreasing after insertion of the lipids as required for a well-ordered planar lipid bilayer [18].

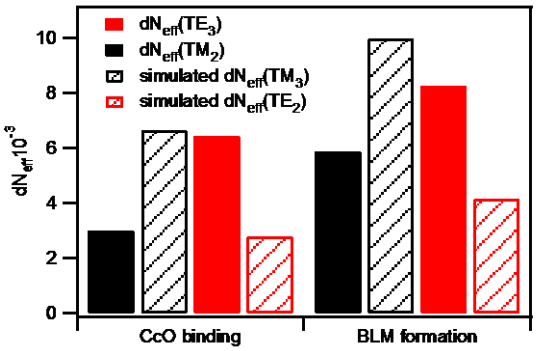

Figure 9.4: Change of the effective refractive index, δn_{eff} for the *TM* and *TE* optical waveguide modes after each preparation step of the *ptBLM* on *P(HEAAm-co-NTAAAm-co-MABP).* The δn_{eff} values were derived from the n_{eff} in Table 9.1. Results from simulations using an isotropic adlayer and the software described in experimental part are also presented [1].

9.3 Conclusions

The concept of the *ptBLM* proved to be useful in the context of polymer-supported planar lipid bilayers. In particular, hydrogel-supported *ptBLMs* based on a polymer with mesh sizes smaller than the size of the protein were shown to result in very robust polymer-supported planar lipid bilayers, exhibiting good electrical insulation properties [1]. Cytochrome c oxidase could easily be incorporated in a functionally active form. Furthermore, the use of *ITO* as a conducting and waveguiding substrate allowed addressing the question of anisotropy effects in the layer system. A well-ordered lipid bilayer should exhibit different optical properties in different directions. The same argument holds to a lesser extent for an ordered and oriented protein monolayer. The experimental proof of this anisotropy is hard to achieve and hence information about the proper arrangement of a protein/lipid layer is scarce. Due to their multi-mode approach, waveguide measurements have the potential to access these properties. The advantage of an *ITO* layers is that they can be used as a waveguide as well as a substrate for electrochemical measurements. However, preparation conditions need to be optimized carefully. The thickness needs to be compromised vs. stability and surface roughness of the *ITO*. Surface roughness that was deteriorated by spike structures could successfully be overcome by coverage with the hydrogel. The polymer layer in turn had to be kept at a thickness of around 60 *nm* in order to ensure a smooth surface for the protein/lipid layer. Layer thickness of about 60 *nm* is sufficient to mimic the submembrane space. Small

molecules such as *cyt c* penetrate easily.

The gel-supported *ptBLM* with mesh sizes below the size of the protein proved to be a good approach towards polymer-supported *BLMs*. This ensures that the protein preferentially binds to the top layer so that a lipid layer forms exclusively at the interphase between polymer and water.

9.4 Experimental Part

4-(3-triethoxysilyl)propyloxybenzophenone [14] (*BP*-silane), pentafluorophenyl acrylate [15] (*PFPA*) and 4-benzoylphenyl methacrylate [16] (*MABP*) were prepared according to the literature. Azodiisobutyronitrile (*AIBN*) (Sigma Aldrich, Germany) was recrystallized from methanol. Dioxane (Sigma Aldrich, Germany) was distilled over calcium hydride.

Polymerization of PFPA-co-MABP

The reactive copolymer poly(pentafluorophenol acrylate-co-4-benzoylphenyl methacrylate) *(P(PFPA-co-MABP))* was polymerized from 98 mol % *PFPA* and 2 mol % *MABP* by free radical polymerization with 0.2 *mo*l % *AIBN* in dioxane at 60 °*C* for 48 *h*. It was precipitated in methanol and dried in high vacuum.

The reactive copolymer was obtained with a yield of 78 % after precipitating it three times from benzene in methanol. The molecular weight M_w was determined by *GPC* (tetrahydrofurane as solvent and poly(methylmethacrylate) as standard) to be ~14.000 g/mol and the molecular weight distribution was ~2.1. The ^{1}*H-NMR* shows the peaks of the *PFPA* and the *MABP* with a ratio of 98:2 as intended by the monomer mixture. ^{1}*H-NMR* (700 *MHz*, CD_2Cl_2): δ [*ppm*] = 7.45 (9 *H, br m*, benzophenone), 3.11 (1 *H, br s, CH*, backbone), 2.15 (2 *H, br s, CH_2*, backbone), 1.48 (3 *H, br m, CH_3*, backbone).

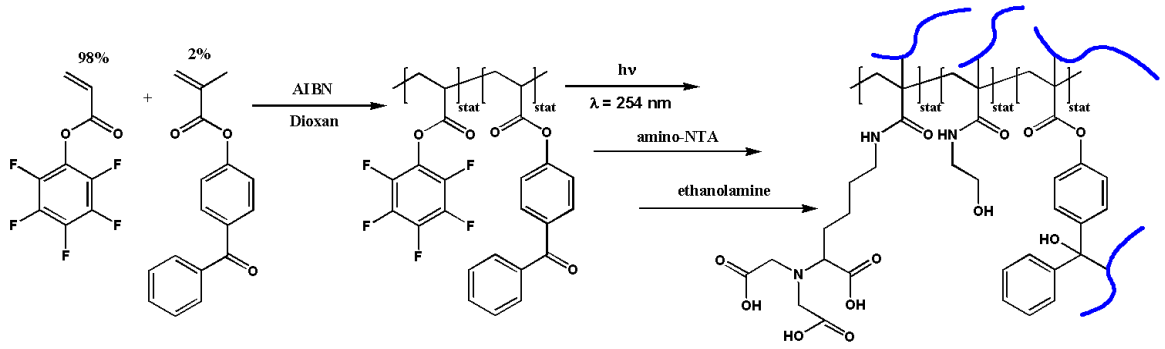

Figure 9.5: Scheme of synthesis of the precursor polymer *P(PFPA-co-MABP)* and its conversion into the *PHEAAm*-hydrogel with attached *NTA* groups *(P(HEAAm-co-NTAAAm-co-MABP))* [1].

Preparation of *ITO* Layers on Glass Slides

The *ITO* layer was deposited on float glass (Menzel, Braunschweig, Germany). Glass slides were cleaned in piranha solution ($H_2O:H_2SO_4:H_2O_2$; *5:1:1 v/v*) and rinsed using *DI* water. *ITO* was deposited by *DC* magnetron sputtering using a Balzers sputtering system (Oerlikon Balzers Lichtenstein). The target used was a 3 inch $In_2O_3:SnO_2$ (90:10) (MaTeck, Jülich, Germany). Series of slides were always prepared on the same day. After deposition under each parameter set, the sheet resistance R_s was measured by a four-point probe method according to Van-der-Paw [17]. The process pressure was P_b = 5.5 10^{-6} *mbar*. The *ITO* target was pre-treated without the samples under following conditions: 15 *min* sputtering time using an argon/oxygen mix (10 % *vol* O_2) at a gas pressure P_b of 1.1 *Pa* and a *DC* power of 100 *W*. Afterwards 100 *nm ITO* was sputtered on top of the glass slides using a pure *Ar* atmosphere without any oxygen at 0.27 Pa and 100 *W*. The deposition time was usually 10 – 15 *m*in and the layer thickness, measured by step-profiler and ellipsometry was 80 - 120 *nm*. The morphology of the *ITO* surface was analyzed by *AFM*.

Preparation of the Gel Layer

The *ITO* coated glass slides were functionalized with the BP-silane as described earlier [14]. On top of the silane layer the reactive copolymer *P(PFPA-co-MAPB)* was spin-coated from chloroform (1 w%), dried over night at 50 °*C* in a vacuum oven and crosslinked by photo-polymerization with at wavelength λ = 254 *nm* and a total energy of 60 *J* cm^{-2}.

Functionalization with NTA

The polymer-coated *ITO* samples were incubated for 2 *h* in an aqueous 0.15 *M* nitrilo-triacetic acid (amino-*NTA*) solution (pH 9.8, 0.5 *M* K_2CO_3 buffer) and after 2 *h* ethanolamine (80 *mM*) was added to the same solution. The samples were left in the solution for another 30 *min* and subsequently rinsed using Milli-Q water.

Binding of CcO and Reconstitution of a Lipid Bilayer Membrane

CcO from *P. denitrificans* with ahis-tag at the C-terminus of subunit *I* was prepared according to [17].

The *ITO* slides were immersed for 30 *min* in 40 *mM NiSO4* in acetate buffer (50 *mM*, *pH* 5.5). The excess nickel was removed by brief rinsing using the same acetate buffer without nickel. Then the *CcO* dissolved in dodecyl β-D-maltoside (*DDM*)-phosphate-buffer (K_2HPO_4 0.1 *M*, *KCl* 0.05 *M, pH*=8, 0.1%*DDM*) was adsorbed to the *NTA*-functionalized surface at a final concentration of 100 *nM*. Bio-Beads were added to the lipid detergent containing phosphate buffer (K_2HPO_4 0.1 *M*, *KCl* 0.05 *M*, *pH* 8, diphytanoylphosphatidylcholine (*DiPhyPC*) 0.05 *mg/ml*, 0.1% *DDM*) to remove the detergent and to form a lipid bilayer using an amplitude of 10 *mV*. Resulting cyclic voltammetry spectra were analyzed by Zview (Version 2.6, Scribner Associates, Southern Pines, NC) by complex nonlinear fitting of the data to a model circuit.

Surface Plasmon Resonance /Optical Waveguide Spectroscopy (*SPR/OWS*)

SPR/OWS was performed in a custom made setup described previously in chapter 3.1. The glass slide (*LaSFN9* glass from Hellma Optic, Jena, refractive index n = 1.8385 at λ = 632.8 *nm*) was optically matched to the base of a 45° glass prism (*LaSFN9*). Monochromatic light from a He/Ne Laser, (Uniphase, San Jose, CA) at λ = 632.8 *nm* was directed through the prism and collected by a custom made photodiode detector. The glass slide was provided with a multilayer system starting with a 41 *nm* thick gold layer electro-thermally evaporated on top of 2 *nm* thick Cr adhesion layer. A 680 *nm* thick *ITO* layer was then sputtered onto the gold layer under the conditions described above and the surface was spin-coated with *P(HEAAm-co-NTAAAm-co-MABP)*. *ITO* served as the guiding media as well as the working electrode. The n_{eff} values of the

gel-supported *tBLM* were calculated and collected in Table 3. Change of n_{eff} (Δn_{eff}) for varying *ITO* thickness was simulated using an isotropic refractive index of n = 1.9065 for the *ITO* taken from ellipsometry measurements.

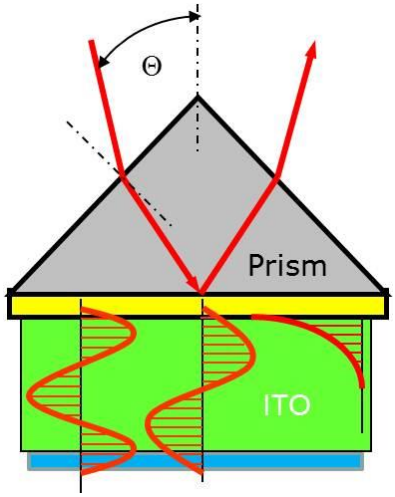

Figure 9.6: SPR/OWS in Kretschman configuration with *ITO* layer and hydrogel film on top.

Reference

[1] Kibrom, A., Roskamp, R.F., Jonas, U., Menges, B., Knoll, W., Naumann, R. L.C. , *Soft Matter*, 2011, 7, 1, 237-246

[2] Kuhner, M., Tampe, R. and Sackmann, E., *Biophysical Journal*, 1994, **67**, 217-226

[3] Simon, J., Kuhner, M., Ringsdorf, H. and Sackmann, E., *Chemistry and Physics of Lipids*, 1995, **76**, 241-258

[4] C. A. Naumann, O. Prucker, T. Lehmann, J. Ruhe, W. Knoll and C. W. Frank, 2002, *Biomacromolecules*, **3**, 27-35

[5] O. Purrucker, A. Fortig, R. Jordan and M. Tanaka, 2004, *Chemphyschem*, **5**, 327-335

[6] R. L. C. Naumann, M. G. Friedrich, V. Kirste and W. Knoll, *Biophys. J.* , 2007, , 4A

[7] J. Arnau, C. Lauritzen, G. E. Petersen and J. Pedersen, 2006, *Protein Expression and Purif.*, **48**, 1-13

[8] E. Hochuli, H. Dobeli, and A. Schacher, 1987, *J. Chromatogr.*, **411**, 177–184

[9] Belevich, M. I. Verkhovsky and M. Wikström, 2006, *Nature*, **440**, 829-832

[10] H. Michel, 1998, *Proc. Natl. Acad. Sci. U. S. A.*, **95**, 12819-12824

[11] K. Ataka, F. Giess, W. Knoll, R. Naumann, S. Haber-Pohlmeier, B. Richter and J. Heberle, *J. Am. Chem. Soc.* , 2004, **126**, 16199-16206

[12] M. G. Friedrich, M. A. Plum, M. G. Santonicola, V. U. Kirste, W. Knoll, B. Ludwig and R. L. C. Naumann, 2008, *Biophys. J.*, **95**, 1500-1510

[13] M. G. Friedrich, F. Giess, R. Naumann, W. Knoll, K. Ataka, J. Heberle, J. Hrabakova, D. H. Murgida and P. Hildebrandt, 2004, *Chemical Communications*, 2376-2377

[14] M. Gianneli, R. F. Roskamp, U. Jonas, B. Loppinet, G. Fytas and W. Knoll, *SoftMatter*, 2008, **4**., 1443-1447

[15] M. Eberhardt, R. Mruk, R. Zentel and P. Théato, *Europ. Poly. J.*, 2005, **41**., 1569-1575

[16] R. Toomey, D. Freidank and J. Rühe, *Macromolecules*, 2004, **37**, 882-887

[17] S. Lucioli, K. Hoffmeier, R. Carrozzo, A. Tessa, B. Ludwig and F. M. Santorelli, *Neurogenetics*, 2006, **7**, 51-57

[18] Z. Salamon, G. Tollin, *Biophysical Journal*, 2001, **86**, 2508-2516

10 Conclusions

The novel combination of Surface Plasmon Resonance and Optical Waveguide Spectroscopy (*SPR/OWS*) with the reversed Wentzel-Kramers-Brillouin (*rWKB*) approximation is a powerful technique to gain detailed information about refractive index profiles, gradients and inhomogeneities in thin surface-attached thermo-responsive hydrogel films. By *SPR/OWS* spectroscopy the reflectivity minima of waveguide modes and surface plasmon resonance are measured in angular reflectivity scans. From the angular position of these minima the refractive index profile perpendicular to the film surface is calculated by the reversed *WKB* approximation. Such a refractive index profile forms the basis of a multilayer model, in which for each individual slab perpendicular to the multilayer surface the local refractive index n and the corresponding imaginary part κ is calculated. This imaginary part κ is a measure for optical losses, which are interpreted in our system as hydrogel inhomogeneities. Through this treatment we could identify different levels of inhomogeneities for the individual layer slabs that vary characteristically with temperature and salt concentration. In particular the inhomogeneities in the layer centre increased significantly for temperatures and salt concentrations around the layer transition from the swollen to the collapsed state.

Composite hydrogels consisting of Poly(N-Isopropylacrylamid) (*pNIPAAm*) reinforced with nanoparticles (*NP*) allowed us to create surface-attached thin films with good optical quality that show very homogeneous swelling when 20–50%-wt *NPs* are present. Furthermore, the swelling ratio can be controlled by the relative amount of particles. Remarkably the volume transition temperature (T_c) of the composite is still fully determined by the polymer matrix and not by the nanoparticles as is shown by the fact that the T_c is not significantly affected by the *NP* content of the samples. These *NPs* form an ideal scaffold to introduce functional groups that are well embedded into a *pNIPAAm* matrix, without changing T_c. This concept is highly useful for sensor applications.

Controlled addition of ethanol as cononsolvent can be used to trigger the volume transition of the gel at a desired temperature. Films of *pNIPAAm* immobilized on gold substrates in mixed solvents behave similar to the *pNIPAAm* solutions reported in the literature. First they show a decrease in T_c by the addition of a good organic solvent to the aqueous solution of

pNIPAAm (here up to 20% ethanol). At higher fractions of good organic solvent (here 70% ethanol) the T_c increases and possibly exceeds the boiling point of the mixture. Furthermore, the obtained results are particularly important when considering *pNIPAAm* as responsive matrix material in sensor applications. Cononsolvency presents an interesting tool there for deliberately inducing the collapse of the sensor gel matrix after analyte binding by a change of solvent composition. Thus the bound analyte would be locally concentrated at the sensor interface before signal read-out. The study of cononsolvency also provides information on potential composition effects in analyte solutions, which have to be taken into account to design a reliable sensor and accurately interpret the sensor response.

For ultra-thin *pNIPAAm* films, less than 100 *nm* thickness changes in the phase transition temperature and the volume degree of swelling were observed. The ultra-thin film was not able to swell or collapse completely anymore because of confinement effects to the substrate. Moreover the substrate prevents the complete diffusion of the solvent. This can be detected by the higher refractive index and the slightly higher transition temperature T_c.

We implemented the Optical Waveguide Spectroscopy (*OWS*) for the time-resolved quantitative studies of protein-functionalized hydrogel films. We showed that this method allowed the observation of changes in mass distribution in a gel film through the simultaneous measurement of its thickness and refractive index. *OWS* was applied for the investigation of the coupling of protein molecules to a *pNIPAAm*-based hydrogel film, which was achieved by using a novel charge-attraction scheme that exploited tetrafluorophenol-sulfonate active ester chemistry. The hydrogel can be used as a binding matrix into which protein molecules can diffuse and bind to the immobilized catcher molecules. In addition, the investigation of the non-specific binding of blood plasma to the gel film revealed its good anti-fouling properties, which makes it, for instance, a good candidate for future applications in affinity biosensors.

The concept of Poly(N-Isopropylacrylamid) (*pNIPAAm*) supported protein-tethered bilayer lipid membranes (*ptBLM*) was proved to be useful in the context of polymer-supported planar lipid bilayers. In particular, hydrogel-supported *ptBLMs* based on a polymer with mesh sizes smaller than the size of the protein were shown to result in very robust polymer-supported planar lipid bilayers. Cytochrome c oxidase (*CcO*) could easily be incorporated in a functionally active form. Furthermore, the use of indium-tin oxide (*ITO*) as a conducting and waveguiding substrate allowed addressing the question of anisotropy effects

in the layer system. Due to their multi-mode approach, waveguide measurements have the potential to access these properties. The advantage of an *ITO* layer is their use as a waveguide as well as a substrate for electrochemical measurements. However, preparation conditions need to be optimized carefully. The thickness needs to be compromised vs. stability and surface roughness of the *ITO*. Surface roughness that was deteriorated by spike structures could successfully be overcome by coverage with the hydrogel. The polymer layer in turn had to be kept at a thickness of around 60 *nm* in order to ensure a smooth surface for the protein/lipid layer. Layer thickness of about 60 *nm* is sufficient to mimic the submembrane space.